

World Journal of *Radiology*

World J Radiol 2010 November 28; 2(11): 417-454





Editorial Board

2009-2013

The *World Journal of Radiology* Editorial Board consists of 319 members, representing a team of worldwide experts in radiology. They are from 40 countries, including Australia (3), Austria (4), Belgium (5), Brazil (3), Canada (9), Chile (1), China (25), Czech (1), Denmark (1), Egypt (4), Estonia (1), Finland (1), France (6), Germany (17), Greece (8), Hungary (1), India (9), Iran (5), Ireland (1), Israel (4), Italy (28), Japan (14), Lebanon (1), Libya (1), Malaysia (2), Mexico (1), Netherlands (4), New Zealand (1), Norway (1), Saudi Arabia (3), Serbia (1), Singapore (2), Slovakia (1), South Korea (16), Spain (8), Switzerland (5), Thailand (1), Turkey (20), United Kingdom (16), and United States (82).

PRESIDENT AND EDITOR-IN-CHIEF

Lian-Sheng Ma, Beijing

STRATEGY ASSOCIATE EDITORS-IN-CHIEF

Ritesh Agarwal, Chandigarh
Kenneth Coenegrachts, Bruges
Mannudeep K Kalra, Boston
Meng Law, Los Angeles
Ewald Moser, Vienna
Aytekin Oto, Chicago
AAK Abdel Razek, Mansoura
Àlex Rovira, Barcelona
Yi-Xiang Wang, Hong Kong
Hui-Xiong Xu, Guangzhou

GUEST EDITORIAL BOARD MEMBERS

Wing P Chan, Taipei
Wen-Chen Huang, Taipei
Shi-Long Lian, Kaohsiung
Chao-Bao Luo, Taipei
Shu-Hang Ng, Taoyuan
Pao-Sheng Yen, Haulien

MEMBERS OF THE EDITORIAL BOARD



Australia

Karol Miller, Perth
Tomas Kron, Melbourne
Zhonghua Sun, Perth



Austria

Herwig R Cerwenka, Graz

Daniela Prayer, Vienna
Siegfried Trattning, Vienna



Belgium

Piet R Dirix, Leuven
Yicheng Ni, Leuven
Piet Vanhoenacker, Aalst
Jean-Louis Vincent, Brussels



Brazil

Emerson L Gasparetto, Rio de Janeiro
Edson Marchiori, Petrópolis
Wellington P Martins, São Paulo



Canada

Sriharsha Athreya, Hamilton
Mark Otto Baerlocher, Toronto
Martin Charron, Toronto
James Chow, Toronto
John Martin Kirby, Hamilton
Piyush Kumar, Edmonton
Catherine Limperopoulos, Quebec
Ernest K Osei, Kitchener
Weiguang Yao, Sudbury



Chile

Masami Yamamoto, Santiago



China

Feng Chen, Nanjing
Ying-Sheng Cheng, Shanghai
Woei-Chyn Chu, Taipei

Guo-Guang Fan, Shenyang
Shen Fu, Shanghai
Gang Jin, Beijing
Tak Yeung Leung, Hong Kong
Wen-Bin Li, Shanghai
Rico Liu, Hong Kong
Yi-Yao Liu, Chengdu
Wei Lu, Guangdong
Fu-Hua Peng, Guangzhou
Li-Jun Wu, Hefei
Zhi-Gang Yang, Chengdu
Xiao-Ming Zhang, Nanchong
Chun-Jiu Zhong, Shanghai



Czech

Vlastimil Válek, Brno



Denmark

Poul Erik Andersen, Odense



Egypt

Mohamed Abou El-Ghar, Mansoura
Mohamed Ragab Nouh, Alexandria
Ahmed A Shokeir, Mansoura



Estonia

Tiina Talvik, Tartu



Finland

Tove J Grönroos, Turku

**France**

Alain Chapel, *Fontenay-Aux-Roses*
 Nathalie Lassau, *Villejuif*
 Youlia M Kirova, *Paris*
 Géraldine Le Duc, *Grenoble Cedex*
 Laurent Pierot, *Reims*
 Frank Pilleul, *Lyon*
 Pascal Pommier, *Lyon*

**Germany**

Ambros J Beer, *München*
 Thomas Deserno, *Aachen*
 Frederik L Giesel, *Heidelberg*
 Ulf Jensen, *Kiel*
 Markus Sebastian Juchems, *Ulm*
 Kai U Juergens, *Bremen*
 Melanie Kettering, *Jena*
 Jennifer Linn, *Munich*
 Christian Lohrmann, *Freiburg*
 David Maintz, *Münster*
 Henrik J Michaely, *Mannheim*
 Oliver Micke, *Bielefeld*
 Thoralf Niendorf, *Berlin-Buch*
 Silvia Obenauer, *Duesseldorf*
 Steffen Rickes, *Halberstadt*
 Lars V Baron von Engelhardt, *Bochum*
 Goetz H Welsch, *Erlangen*

**Greece**

Panagiotis Antoniou, *Alexandroupolis*
 George C Kagadis, *Rion*
 Dimitris Karacostas, *Thessaloniki*
 George Panayiotakis, *Patras*
 Alexander D Rapidis, *Athens*
 C Triantopoulou, *Athens*
 Ioannis Tsalafoutas, *Athens*
 Virginia Tsapaki, *Anixi*
 Ioannis Valais, *Athens*

**Hungary**

Peter Laszlo Lakatos, *Budapest*

**India**

Anil Kumar Anand, *New Delhi*
 Surendra Babu, *Tamilnadu*
 Sandip Basu, *Bombay*
 Kundan Singh Chufal, *New Delhi*
 Shivanand Gamanagatti, *New Delhi*
 Vimoj J Nair, *Haryana*
 R Prabhakar, *New Delhi*
 Sanjeeb Kumar Sahoo, *Orissa*

**Iran**

Vahid Reza Dabbagh Kakhki, *Mashhad*
 Mehran Karimi, *Shiraz*
 Farideh Nejat, *Tehran*
 Alireza Shirazi, *Tehran*
 Hadi Rokni Yazdi, *Tehran*

**Ireland**

Joseph Simon Butler, *Dublin*

**Israel**

Amit Gefen, *Tel Aviv*
 Eyal Sheiner, *Be'er-Sheva*
 Jacob Sosna, *Jerusalem*
 Simcha Yagel, *Jerusalem*

**Italy**

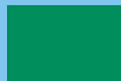
Mohssen Ansarin, *Milan*
 Stefano Arcangeli, *Rome*
 Tommaso Bartalena, *Imola*
 Filippo Cademartiri, *Parma*
 Sergio Casciaro, *Lecce*
 Laura Crocetti, *Pisa*
 Alberto Cuocolo, *Napoli*
 Mirko D'Onofrio, *Verona*
 Massimo Filippi, *Milan*
 Claudio Fiorino, *Milano*
 Alessandro Franchello, *Turin*
 Roberto Grassi, *Naples*
 Stefano Guerriero, *Cagliari*
 Francesco Lassandro, *Napoli*
 Nicola Limbucci, *L'Aquila*
 Raffaele Lodi, *Bologna*
 Francesca Maccioni, *Rome*
 Laura Martincich, *Candiolo*
 Mario Mascalchi, *Florence*
 Roberto Miraglia, *Palermo*
 Eugenio Picano, *Pisa*
 Antonio Pinto, *Naples*
 Stefania Romano, *Naples*
 Luca Saba, *Cagliari*
 Sergio Sartori, *Ferrara*
 Mariano Scaglione, *Castel Volturno*
 Lidia Strigari, *Rome*
 Vincenzo Valentini, *Rome*

**Japan**

Shigeru Ehara, *Morioka*
 Nobuyuki Hamada, *Chiba*
 Takao Hiraki, *Okayama*
 Akio Hiwatashi, *Fukuoka*
 Masahiro Jinzaki, *Tokyo*
 Hiroshi Matsuda, *Saitama*
 Yasunori Minami, *Osaka*
 Jun-Ichi Nishizawa, *Tokyo*
 Tetsu Niwa, *Yokohama*
 Kazushi Numata, *Kanagawa*
 Kazuhiko Ogawa, *Okinawa*
 Hitoshi Shibuya, *Tokyo*
 Akira Uchino, *Saitama*
 Haiquan Yang, *Kanagawa*

**Lebanon**

Aghiad Al-Kutoubi, *Beirut*

**Libya**

Anuj Mishra, *Tripoli*

**Malaysia**

R Logeswaran, *Cyberjaya*
 Kwan-Hoong Ng, *Kuala Lumpur*

**Mexico**

Heriberto Medina-Franco, *Mexico City*

**Netherlands**

Jurgen J Fütterer, *Nijmegen*
 Raffaella Rossin, *Eindhoven*
 Paul E Sijens, *Groningen*
 Willem Jan van Rooij, *Tilburg*

**New Zealand**

W Howell Round, *Hamilton*

**Norway**

Arne Sigmund Borthne, *Lørenskog*

**Saudi Arabia**

Mohammed Al-Omran, *Riyadh*
 Ragab Hani Donkol, *Abha*
 Volker Rudat, *Al Khobar*

**Serbia**

Djordjije Saranovic, *Belgrade*

**Singapore**

Uei Pua, *Singapore*
 Lim CC Tchoyoson, *Singapore*

**Slovakia**

František Dubecký, *Bratislava*

**South Korea**

Bo-Young Choe, *Seoul*
 Joon Koo Han, *Seoul*
 Seung Jae Huh, *Seoul*
 Chan Kyo Kim, *Seoul*
 Myeong-Jin Kim, *Seoul*
 Seung Hyup Kim, *Seoul*
 Kyoung Ho Lee, *Gyeonggi-do*
 Won-Jin Moon, *Seoul*
 Wazir Muhammad, *Daegu*
 Jai Soung Park, *Bucheon*
 Noh Hyuck Park, *Kyunggi*
 Sang-Hyun Park, *Daejeon*
 Joon Beom Seo, *Seoul*
 Ji-Hoon Shin, *Seoul*
 Jin-Suck Suh, *Seoul*
 Hong-Gyun Wu, *Seoul*



Spain

Eduardo J Aguilar, *Valencia*
 Miguel Alcaraz, *Murcia*
 Juan Luis Alcaraz, *Pamplona*
 Gorka Bastarrika, *Pamplona*
 Rafael Martínez-Monge, *Pamplona*
 Alberto Muñoz, *Madrid*
 Joan C Vilanova, *Girona*



Switzerland

Nicolau Beckmann, *Basel*
 Silke Grabherr, *Lausanne*
 Karl-Olof Löfblad, *Geneva*
 Tilo Niemann, *Basel*
 Martin A Walter, *Basel*



Thailand

Sudsriluk Sampatchalit, *Bangkok*



Turkey

Olus Api, *Istanbul*
 Kubilay Aydin, *Istanbul*
 Işıl Bilgen, *Izmir*
 Zulkif Bozgeyik, *Elazig*
 Barbaros E Çil, *Ankara*
 Gulgun Engin, *Istanbul*
 M Fatih Evcimik, *Malatya*
 Ahmet Kaan Gündüz, *Ankara*
 Tayfun Hakan, *Istanbul*
 Adnan Kabaalioglu, *Antalya*
 Fehmi Kaçmaz, *Ankara*
 Musturay Karcaaltincaba, *Ankara*
 Osman Kizilkilic, *Istanbul*
 Zafer Koc, *Adana*
 Cem Onal, *Adana*
 Yahya Paksoy, *Konya*
 Bunyamin Sahin, *Samsun*
 Ercument Unlu, *Edirne*
 Ahmet Tuncay Turgut, *Ankara*
 Ender Uysal, *Istanbul*



United Kingdom

K Faulkner, *Wallsend*
 Peter Gaines, *Sheffield*
 Balaji Ganeshan, *Brighton*
 Nagy Habib, *London*
 Alan Jackson, *Manchester*
 Pradesh Kumar, *Portsmouth*
 Tarik F Massoud, *Cambridge*
 Igor Meglinski, *Bedfordshire*
 Robert Morgan, *London*
 Ian Negus, *Bristol*
 Georgios A Plataniotis, *Aberdeen*
 N J Raine-Fenning, *Nottingham*
 Manuchehr Soleimani, *Bath*
 MY Tseng, *Nottingham*
 Edwin JR van Beek, *Edinburgh*
 Feng Wu, *Oxford*



United States

Athanasios Argiris, *Pittsburgh*
 Stephen R Baker, *Newark*
 Lia Bartella, *New York*
 Charles Bellows, *New Orleans*
 Walter L Biff, *Denver*
 Homer S Black, *Houston*
 Wessam Bou-Assaly, *Ann Arbor*
 Owen Carmichael, *Davis*
 Shelton D Caruthers, *St Louis*
 Yuhchay Chen, *Rochester*
 Melvin E Clouse, *Boston*
 Ezra Eddy Wyssam Cohen, *Chicago*
 Aaron Cohen-Gadol, *Indianapolis*
 Patrick M Colletti, *Los Angeles*
 Kassa Darge, *Philadelphia*
 Abhijit P Datir, *Miami*
 Delia C DeBuc, *Miami*
 Russell L Deter, *Houston*
 Adam P Dicker, *Phil*
 Khaled M Elsayes, *Ann Arbor*
 Steven Feigenberg, *Baltimore*
 Christopher G Filippi, *Burlington*
 Victor Frenkel, *Bethesda*
 Thomas J George Jr, *Gainesville*
 Patrick K Ha, *Baltimore*
 Robert I Haddad, *Boston*
 Walter A Hall, *Syracuse*
 Mary S Hammes, *Chicago*
 John Hart Jr, *Dallas*
 Randall T Higashida, *San Francisco*
 Juebin Huang, *Jackson*
 Andrei Iagaru, *Stanford*
 Craig Johnson, *Milwaukee*
 Ella F Jones, *San Francisco*
 Csaba Juhasz, *Detroit*
 Riyadh Karmy-Jones, *Vancouver*
 Daniel J Kelley, *Madison*
 Amir Khan, *Longview*
 Euishin Edmund Kim, *Houston*
 Vikas Kundra, *Houston*
 Kenneth F Layton, *Dallas*
 Rui Liao, *Princeton*
 CM Charlie Ma, *Philadelphia*
 Nina A Mayr, *Columbus*
 Thomas J Meade, *Evanston*
 Steven R Messé, *Philadelphia*
 Nathan Olivier Mewton, *Baltimore*
 Feroze B Mohamed, *Philadelphia*
 Koenraad J Morteale, *Boston*
 Mohan Natarajan, *San Antonio*
 John L Nosher, *New Brunswick*
 Chong-Xian Pan, *Sacramento*
 Dipanjan Pan, *St Louis*
 Martin R Prince, *New York*
 Reza Rahbar, *Boston*
 Carlos S Restrepo, *San Antonio*
 Veronica Rooks, *Honolulu*
 Maythem Saeed, *San Francisco*
 Edgar A Samaniego, *Palo Alto*
 Kohkan Shamsi, *Doylestown*
 Jason P Sheehan, *Charlottesville*
 William P Sheehan, *Willmar*
 Charles Jeffrey Smith, *Columbia*
 Monvadi B Srichai-Parsia, *New York*
 Dan Stoianovici, *Baltimore*
 Janio Szklaruk, *Houston*
 Dian Wang, *Milwaukee*
 Jian Z Wang, *Columbus*
 Liang Wang, *New York*
 Shougang Wang, *Santa Clara*
 Wenbao Wang, *New York*
 Aaron H Wolfson, *Miami*
 Gayle E Woloschak, *Chicago*
 Ying Xiao, *Philadelphia*
 Juan Xu, *Pittsburgh*
 Benjamin M Yeh, *San Francisco*
 Terry T Yoshizumi, *Durham*
 Jinxing Yu, *Richmond*
 Jianhui Zhong, *Rochester*



Contents

Monthly Volume 2 Number 11 November 28, 2010

- | | | |
|-------------------------|-----|---|
| EDITORIAL | 417 | Radiofrequency ablation of hepatocellular carcinoma: Current status
<i>Minami Y, Kudo M</i> |
| OBSERVATION | 425 | Technological innovations in digital data management and changing roles of imaging specialists in Japan
<i>Ehara S</i> |
| REVIEW | 427 | Pathophysiology of nephrogenic systemic fibrosis: A review of experimental data
<i>Morcos SK, Haylor J</i> |
| ORIGINAL ARTICLE | 434 | Peripheral dose measurement in high-energy photon radiotherapy with the implementation of MOSFET
<i>Vlachopoulou V, Malatara G, Delis H, Theodorou K, Kardamakis D, Panayiotakis G</i> |
| | 440 | Multislice CT virtual intravascular endoscopy of aortic dissection: A pictorial essay
<i>Sun Z, Cao Y</i> |
| BRIEF ARTICLE | 449 | Perfusion characterization of liver metastases from endocrine tumors: Computed tomography perfusion
<i>Guyennon A, Mihaila M, Palma J, Lombard-Bohas C, Chayvialle JA, Pilleul F</i> |

Contents

World Journal of Radiology
Volume 2 Number 11 November 28, 2010

ACKNOWLEDGMENTS I Acknowledgments to reviewers of *World Journal of Radiology*

APPENDIX I Meetings
I-V Instructions to authors

ABOUT COVER Sun Z, Cao Y. Multislice CT virtual intravascular endoscopy of aortic dissection: A pictorial essay.
World J Radiol 2010; 2(11): 440-448
<http://www.wjgnet.com/1949-8470/full/v2/i11/440.htm>

AIM AND SCOPE *World Journal of Radiology* (*World J Radiol*, *WJR*, online ISSN 1949-8470, DOI: 10.4329) is a monthly peer-reviewed, online, open-access, journal supported by an editorial board consisting of 319 experts in radiology from 40 countries.
The major task of *WJR* is to rapidly report the most recent improvement in the research of medical imaging and radiation therapy by the radiologists. *WJR* accepts papers on the following aspects related to radiology: Abdominal radiology, women health radiology, cardiovascular radiology, chest radiology, genitourinary radiology, neuroradiology, head and neck radiology, interventional radiology, musculoskeletal radiology, molecular imaging, pediatric radiology, experimental radiology, radiological technology, nuclear medicine, PACS and radiology informatics, and ultrasound. We also encourage papers that cover all other areas of radiology as well as basic research.

FLYLEAF I-III Editorial Board

EDITORS FOR THIS ISSUE

Responsible Assistant Editor: Na Liu
Responsible Electronic Editor: Xiao-Mei Zheng
Proofing Editor-in-Chief: Lian-Sheng Ma

Responsible Science Editor: Jian-Xia Cheng

NAME OF JOURNAL

World Journal of Radiology

LAUNCH DATE
December 31, 2009

SPONSOR
Beijing Baishideng BioMed Scientific Co., Ltd.,
Room 903, Building D, Ocean International Center,
No. 62 Dongsihuan Zhonglu, Chaoyang District,
Beijing 100025, China
Telephone: 0086-10-8538-1892
Fax: 0086-10-8538-1893
E-mail: baishideng@wjgnet.com
<http://www.wjgnet.com>

EDITING
Editorial Board of *World Journal of Radiology*,
Room 903, Building D, Ocean International Center,
No. 62 Dongsihuan Zhonglu, Chaoyang District,
Beijing 100025, China
Telephone: 0086-10-8538-1892
Fax: 0086-10-8538-1893
E-mail: wjr@wjgnet.com
<http://www.wjgnet.com>

PUBLISHING
Baishideng Publishing Group Co., Limited,
Room 1701, 17/F, Henan Building,
No.90 Jaffe Road, Wanchai, Hong Kong, China
Fax: 00852-3115-8812
Telephone: 00852-5804-2046
E-mail: baishideng@wjgnet.com
<http://www.wjgnet.com>

SUBSCRIPTION

Beijing Baishideng BioMed Scientific Co., Ltd.,
Room 903, Building D, Ocean International Center,
No. 62 Dongsihuan Zhonglu, Chaoyang District,
Beijing 100025, China
Telephone: 0086-10-8538-1892
Fax: 0086-10-8538-1893
E-mail: baishideng@wjgnet.com
<http://www.wjgnet.com>

ONLINE SUBSCRIPTION
One-Year Price 216.00 USD

PUBLICATION DATE
November 28, 2010

CSSN
ISSN 1949-8470 (online)

PRESIDENT AND EDITOR-IN-CHIEF
Lian-Sheng Ma, *Beijing*

STRATEGY ASSOCIATE EDITORS-IN-CHIEF
Ritesh Agarwal, *Chandigarh*
Kenneth Coenegrachts, *Bruges*
Adnan Kabaalioglu, *Antalya*
Meng Law, *Los Angeles*
Ewald Moser, *Vienna*
Aytekin Oto, *Chicago*
AAK Abdel Razek, *Mansoura*
Àlex Rovira, *Barcelona*
Yi-Xiang Wang, *Hong Kong*
Hui-Xiong Xu, *Guangzhou*

EDITORIAL OFFICE

Na Ma, Director
World Journal of Radiology
Room 903, Building D, Ocean International Center,
No. 62 Dongsihuan Zhonglu, Chaoyang District,
Beijing 100025, China
Telephone: 0086-10-8538-1892
Fax: 0086-10-8538-1893
E-mail: wjr@wjgnet.com
<http://www.wjgnet.com>

COPYRIGHT

© 2010 Baishideng. All rights reserved; no part of this publication may be reproduced, stored in a retrieval system, or transmitted in any form or by any means, electronic, mechanical, photocopying, recording, or otherwise without the prior permission of Baishideng. Authors are required to grant *World Journal of Radiology* an exclusive license to publish.

SPECIAL STATEMENT

All articles published in this journal represent the viewpoints of the authors except where indicated otherwise.

INSTRUCTIONS TO AUTHORS

Full instructions are available online at http://www.wjgnet.com/1949-8470/g_info_20100316162358.htm. If you do not have web access please contact the editorial office.

ONLINE SUBMISSION
<http://www.wjgnet.com/1949-8470office>

Radiofrequency ablation of hepatocellular carcinoma: Current status

Yasunori Minami, Masatoshi Kudo

Yasunori Minami, Masatoshi Kudo, Division of Gastroenterology and Hepatology, Department of Internal Medicine, Kinki University School of Medicine, 377-2 Ohno-Higashi Osaka-Sayama, 589-8511, Japan

Author contributions: Minami Y drafted the manuscript and wrote the final version of the manuscript; Kudo M reviewed and approved the last version of the manuscript.

Correspondence to: Masatoshi Kudo, MD, PhD, Division of Gastroenterology and Hepatology, Department of Internal Medicine, Kinki University School of Medicine, 377-2 Ohno-Higashi Osaka-Sayama, 589-8511, Japan. m-kudo@med.kindai.ac.jp

Telephone: +81-72-3660221 Fax: +81-72-3672880

Received: September 13, 2010 Revised: October 14, 2010

Accepted: October 21, 2010

Published online: November 28, 2010

© 2010 Baishideng. All rights reserved.

Key words: Hepatocellular carcinoma; Radiofrequency ablation; Transcatheter arterial chemoembolization

Peer reviewers: Yicheng Ni, MD, PhD, Professor, Biomedical Imaging, Interventional Therapy and Contrast Media Research, Department of Radiology, University Hospitals, K.U. Leuven, Herestraat 49, B-3000, Leuven, Belgium; Sergio Sartori, MD, Department of Internal Medicine, Section of Interventional Ultrasound, St. Anna Hospital, I-44100 Ferrara, Italy

Minami Y, Kudo M. Radiofrequency ablation of hepatocellular carcinoma: Current status. *World J Radiol* 2010; 2(11): 417-424
Available from: URL: <http://www.wjgnet.com/1949-8470/full/v2/i11/417.htm> DOI: <http://dx.doi.org/10.4329/wjr.v2.i11.417>

Abstract

Ablation therapy is one of the best curative treatment options for malignant liver tumors, and can be an alternative to resection. Radiofrequency ablation (RFA) of primary and secondary liver cancers can be performed safely using percutaneous, laparoscopic, or open surgical techniques, and RFA has markedly changed the treatment strategy for small hepatocellular carcinoma (HCC). Percutaneous RFA can achieve the same overall and disease-free survival as surgical resection for patients with small HCC. The use of a laparoscopic or open approach allows repeated placements of RFA electrodes at multiple sites to ablate larger tumors. RFA combined with transcatheter arterial chemoembolization will make the treatment of larger tumors a clinically viable treatment alternative. However, an accurate evaluation of treatment response is very important to secure successful RFA therapy. Since a sufficient safety margin (at least 0.5 cm) can prevent local tumor recurrences, an accurate evaluation of treatment response is very important to secure successful RFA therapy. To minimize complications of RFA, clinicians should be familiar with the imaging features of each type of complication. Appropriate management of complications is essential for successful RFA treatment.

INTRODUCTION

Hepatocellular carcinoma (HCC) is one of the most common solid cancers worldwide, with an estimated annual incidence of at least one million new patients^[1-4]. Furthermore, the liver is second only to lymph nodes as a common site of metastasis from other solid cancers^[5-8]. Surgery is the only curative option for HCC; however, the majority of primary liver cancers are not suitable for curative resection at the time of diagnosis. Difficulties in surgical resection may be related to size, site, and number of tumors, vascular and extrahepatic involvement as well as the general condition and liver function of the patient^[9-12]. There is, therefore, a need to develop a simple and effective technique for the treatment of unresectable tumors within the liver. In recent years, local ablative techniques [percutaneous ethanol injection (PEI), microwave coagulation therapy (MCT) and radiofrequency ablation (RFA)] have emerged in clinical practice to expand the pool of patients considered for liver-directed therapies^[13-16].

Localized application of thermal energy induces tumor cell destruction. When tumor cells are heated above

45–50°C, intracellular proteins are denatured and cell membranes are destroyed through the dissolution and melting of lipid bilayers^[17]. RFA is a localized thermal treatment technique designed to produce tumor destruction by heating tumor tissue to temperatures that exceed 60°C^[17]. The alternating current of radiofrequency waves passing down from an uninsulated electrode tip into the surrounding tissues generates changes in the direction of ions and creates ionic agitation and frictional heating. This tissue heating then drives extracellular and intracellular water out of the tissue, resulting in tissue destruction by coagulative necrosis^[18,19]. Currently, RFA has gained popularity based on the ease of use, safety, reasonable cost and applicability to minimally invasive techniques. This paper reviews the current status of RFA for HCC.

EQUIPMENT

RFA electrodes and generators

Three types of RF electrodes are currently available commercially: two brands of retractable needle electrodes (model 70 and model 90 Starburst XL needles, RITA Medical Systems, Mountain View, CA, USA; LeVein needle electrode, Boston Scientific, Boston, MA, USA) and an internally cooled electrode (Cool-Tip RF electrode; Radionics, Burlington, MA, USA)^[15].

The needle electrodes of RITA consist of a 14-gauge insulated outer needle that houses nine retractable curved electrodes of various lengths. When the electrodes are extended, the device assumes the approximate configuration of a Christmas tree. Nine of the electrodes are hollow and contain thermocouples in their tips in order to measure the temperature of adjacent tissue. The alternating electric current generator comes in a 250-W model at 460 kHz (Model 1500X RF Generator, RITA Medical Systems). The ablation algorithm is based on temperature at the tips of the electrodes. After the ablation cycle is completed, a temperature reading from the extended electrodes in excess of 50°C at 1 min is considered to indicate satisfactory ablation.

Another RFA device (LeVein Needle Electrode; Radiotherapeutics) has retractable curved electrodes and an insulated 17-gauge outer needle that houses 10 solid retractable curved electrodes that, when deployed, assume the configuration of an umbrella. The electrodes are manufactured in different lengths (2- to 4.0-cm umbrella diameter). The alternating electric current generator is 200 W operated at 480 kHz (RF 3000; Boston Scientific). The ablation algorithm is based on tissue impedance, and ablation is considered successful if the device impedes out.

The third RFA device (Cool-Tip radiofrequency electrode; Radionics) has an insulated hollow 17-gauge needle with an exposed needle tip of variable length (2- or 3-cm). The tip of the needle contains a thermocouple to record the temperature of adjacent tissue. The shaft of the needle has two internal channels to allow the needle to be perfused with chilled water. In an attempt to further increase the size of the ablation area, the manufacturer

placed three of the cooled needles in a parallel triangular cluster with a common hub. The generator has a peak power output of 200 W and is operated at 480 kHz (CC-1; Radionics). The ablation algorithm is based on tissue impedance, and ablation is considered successful if the device impedes out. As a result, successful ablations usually increase the temperature of the ablated tissue to above 60°C.

Selection criteria of patients with HCC

In patients with HCC, exclusion criteria should include evidence of extrahepatic metastases and/or lobar and local portal venous thrombosis or uncontrolled liver disease decompensation, patients with clotting impairment, renal failure, or Child-Pugh class C cirrhosis. In the EASL Consensus Conference criteria^[20], all patients that had tumor nodules with a maximum diameter of 3 cm and not more than three in number with contraindications for surgery are included.

Assessment of technical effectiveness

The technical effectiveness of ablation is commonly assessed by findings on contrast-enhanced computed tomography (CT) or magnetic resonance imaging. A tumor was considered to have been successfully ablated when there were no longer any enhanced regions within the entire tumor during the arterial phase and at least a 0.5 cm margin of apparently normal hepatic tissue surrounding the tumor during the portal phase (Figure 1)^[21–23]. This safety margin for RFA therapy is necessary from the perspective of partial volume effect. Failure to establish a sufficient ablative safety margin was shown to be an independently significant risk factor for local tumor progression on multivariate analysis^[24]. Part of the tumor was diagnosed as remaining viable when images of the ablated area showed nodular peripheral enhancement^[25].

CLINICAL OUTCOMES

Percutaneous approach

A randomized control trial (RCT) has shown that RFA achieved survival rates similar to those achieved following resection^[26] (Table 1). Chen *et al.*^[26] conducted a RCT on 180 patients with a solitary HCC ≤ 5 cm indicated to receive either percutaneous RFA or surgical resection. This study showed percutaneous RFA achieved the same overall and disease-free survival rates as surgical resection for patients with small solitary HCC. The 1- and 4-year overall survival rates after percutaneous RFA and surgery were 95.8%, 67.9% and 93.3%, 64.0%, respectively. The corresponding disease-free survival rates were 85.9%, 46.4% and 86.6%, 51.6%, respectively. However, in cases of primary liver cancer in which local curative therapy was achieved by securing a safety margin, the 4-year survival rate was relatively high, at 66%–82% (results in Japan)^[27,28]. Percutaneous RFA has an advantage over liver resection in providing a better short-term postoperative result because local ablative therapy is a less invasive procedure. Although

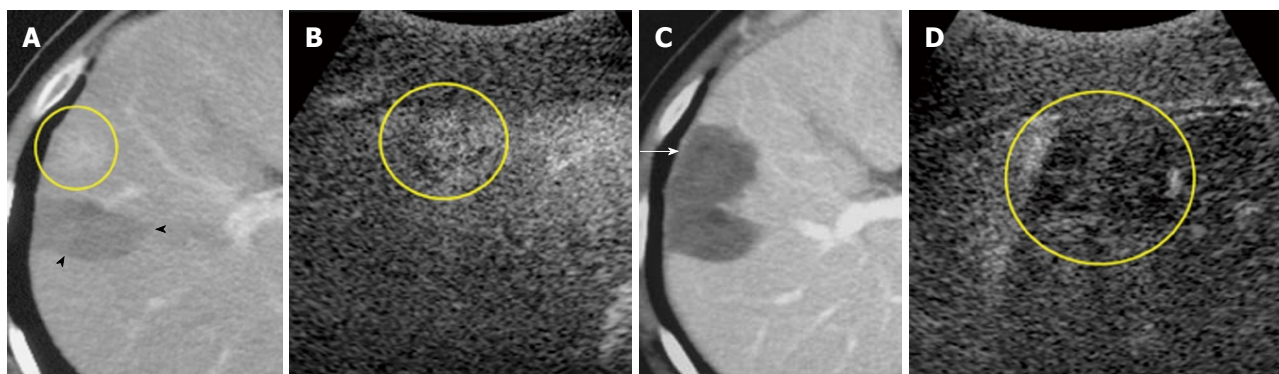


Figure 1 A 61-year-old man with 1.5-cm recurrent hepatocellular carcinoma after ablation therapy in segment 5 of the liver. A: Early-phase dynamic computed tomography (CT) scan shows recurrent tumor (circle). Non-enhanced area (arrowheads) was previously treated by radiofrequency ablation (RFA); B: Contrast harmonic ultrasound (US) using Levovist shows enhancement of viable focus of a hepatocellular carcinoma (HCC) nodule (circle); C: Portal-phase dynamic CT scan, which was obtained 3 d after RFA shows that the tumor was not enhanced, indicating complete necrosis of the lesion (arrow); D: Contrast harmonic US, which was obtained 3 d after ablation shows non-enhanced area (circle).

Table 1 Studies comparing radiofrequency ablation *vs* hepatic resection for hepatocellular carcinoma

Author, yr	Study type	RFA/resection	RFA/resection (mean tumor size, cm)	RFA <i>vs</i> resection (%) (overall survival)	P
Chen, 2006	RCT	90/90	-/-	65.9 <i>vs</i> 64.0 (4-yr)	NS
Takayama, 2009	Retrospective	1315/1235	1.6/1.8	95 <i>vs</i> 94 (2-yr)	0.28
Ueno, 2009	Retrospective	123/110	2.0/2.7	63 <i>vs</i> 80 (5-yr)	0.06
Hiraoka, 2008	Retrospective	105/59	-/-	59.3 <i>vs</i> 59.4 (5-yr)	NS
Abu-Hilal, 2008	Retrospective	34/34	3.0/3.8	57 <i>vs</i> 56 (5-yr)	0.3
Gnglielmi, 2008	Retrospective	23/33	-/-	45 <i>vs</i> 55 (5-yr)	0.7
Wakai, 2006	Retrospective	64/85	-/-	30 <i>vs</i> 53 (10-yr)	0.012
Ogihara, 2005	Retrospective	40/47	4.6/7.4	39 <i>vs</i> 31 (5-yr)	0.79
Montorsi, 2005	Prospective	58/40	-/-	30 <i>vs</i> 53 (4-yr)	0.018
Vivarelli, 2004	Retrospective	79/79	-/-	33 <i>vs</i> 65 (3-yr)	0.002

RFA: Radiofrequency ablation; RCT: Randomized control trial; NS: Not significant.

promising, these data need to be confirmed in larger RCTs before local ablative therapy can replace partial hepatectomy in the treatment of good surgical candidates.

RFA has also been investigated for treating patients with large or multifocal tumors. However, the size and number of tumors are important factors determining the local recurrence rate after RFA^[29]. Apart from the larger tumor volume, large liver cancers more frequently have irregular borders and satellite lesions. Therefore, precise tailoring of the size and shape of the thermal lesion is important in RFA for large liver cancers. A number of precisely calculated overlapping coagulation zones are necessary to treat large liver cancers. To increase the size of the coagulation zone in RFA, investigators tried using vascular occlusion during RFA^[30,31]. Temporary interruption of hepatic blood flow using vascular occlusion techniques (e.g. balloon catheter occlusion of the hepatic artery, transcatheter arterial embolization (TAE), or transcatheter arterial chemoembolization (TACE) has been shown to increase the efficacy of interstitial thermotherapy due to a significant increase in lesion volume. Vascular occlusion causes a reduction of heat dispersion, thus increasing the range of therapeutic thermal coagulation. Peng *et al.*^[32] reported a series of 120 patients with HCC, and the 1-, 2-, 3-, and

5-year overall survival rates for the TACE-RFA and RFA groups were 93%, 83%, 75%, 50%, and 89%, 76%, 64%, 42%, respectively ($P = 0.045$).

Ultrasound (US)-guided procedures are necessary but have limited use when the tumor is located under the diaphragm. However, saline solution injection into the pleural cavity can separate the lung and liver on B-mode US, i.e. artificial pleural effusion acts as an acoustic media. There are reports on the feasibility and safety of RFA with artificially induced pleural effusion for HCC located in the right subphrenic region^[33-36]. In a series of 24 patients with HCC located in the hepatic dome, 200-1100 mL of 5% glucose solution was infused intrathoracically to separate the lung and liver, thus, complete tumor necrosis in a single session was achieved in 96.4% of patients^[36].

Multiple RFA sessions for locally progressive HCCs were previously required because it is frequently difficult to distinguish viable tumors from necrotic tissue on B-mode US^[37]. However, contrast-enhanced harmonic US imaging is able to evaluate small hypervascular HCCs even when B-mode US cannot adequately characterize the tumors^[38-43]. In particular, contrast harmonic US has been improved by the development of second-generation contrast agents such as sulfur hexafluoride microbubbles (So-

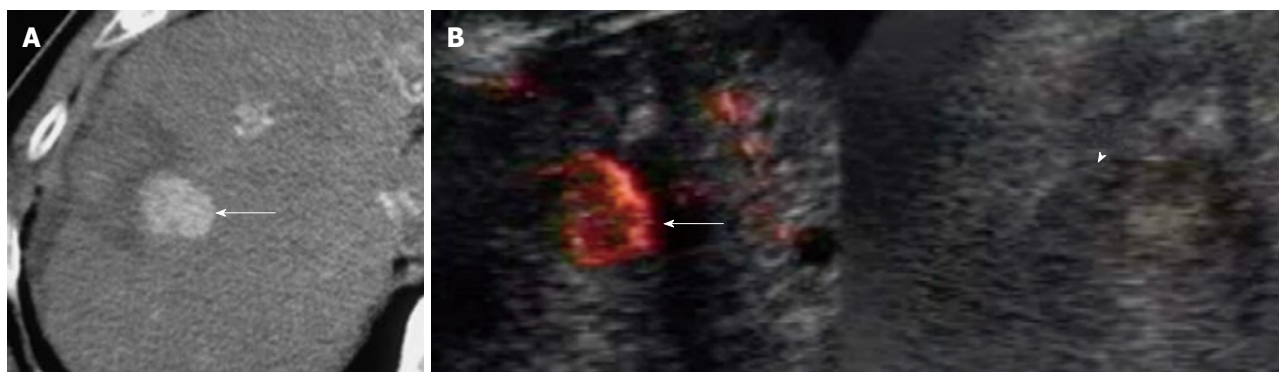


Figure 2 A 71-year-old man with 2.0 cm local tumor progression of hepatocellular carcinoma after radiofrequency ablation therapy in segment 8 of the liver. A: Early-phase dynamic computed tomography (CT) scan shows outgrowth pattern of locally progressive hepatocellular carcinoma (HCC) (arrow). The lesion borders an unenhanced area, which was previously treated; B: Left: Contrast harmonic Doppler ultrasound (US) using Levovist shows enhancement of local tumor progression of HCC (arrow). Therefore, an enhanced lesion can be identified as a target for the insertion of a single RF electrode; Right: B-mode US shows a HCC nodule demonstrated as a low echoic lesion with an unclear border (arrowhead).

noVue; Bracco SpA, Milan, Italy), perflutren lipid microbubbles (Definity; Bristol-Myers Squibb, North Billerica, MA, USA), perflutren protein microbubbles (Optison; GE Healthcare, Buckinghamshire, UK), and perfluorocarbon microbubbles (Sonazoid; Daiichi-Sankyo, Tokyo, Japan). These microbubbles provide stable nonlinear oscillation in a low power acoustic field due to the hard shell of these bubbles, producing great detail in the harmonic signals in real-time^[44-49]. It has been reported that contrast harmonic sonography-guided RFA is an efficient approach for guiding further ablation of hepatic malignancies that are not clearly demarcated by B-mode US (Figure 2)^[50-54].

Laparoscopic/open surgical approach

The use of a laparoscopic or open approach allows repeated placements of RFA electrodes at multiple sites to ablate larger tumors. The laparoscopic approach appears to be the safest and most effective method for small tumors on the liver surface, and offers the advantages of laparoscopic US, which provides better resolution of the number and location of liver tumors^[55,56]. Moreover, a hand-assisted technique can be applied safely and effectively to laparoscopic liver surgery^[57-59]. An intraoperative US probe is inserted into the peritoneal cavity together with the surgeon's hand through a hand-access device. An RF electrode can be subcostally or intercostally advanced into a liver tumor under direct guidance by intraoperative US. Therefore, a hand-assisted laparoscopic US-guided method has advantages for both laparoscopic and open surgical approaches. The postoperative recovery of patients was shorter compared with that after an open surgical approach. Ishiko *et al.*^[57] reported that the surgical procedures consisted of 5 RFA to tumors in the caudate lobe with hand-assisted laparoscopic surgery (HALS), and a postoperative CT scan demonstrated sufficient ablation in all patients and there was no surgical mortality. The HALS approach has several advantages; it facilitates and expedites the procedure, reduces the stress factor on the surgeon, greatly improves exposure, and facilitates immediate and efficient control

of bleeding vessels with the internal hand. The hand-access device, which essentially consists of a cuff with a spiral inflatable valve, enables withdrawal and reinsertion of the hand without loss of pneumoperitoneum during the procedure. However, the local treatment failure rate of the laparoscopic approach was higher in patients with HCC nodules situated deep within the liver and measuring 4 cm or more in diameter^[60]. Great difficulty can be encountered during treatment of lesions located close to the gallbladder or in contact with the diaphragm.

Although more invasive, open RFA can be performed more easily and the puncture course of the RF needle can be more widely selected than that during the laparoscopic approach. It has been reported that patients undergoing radical open RFA demonstrated few ablation site recurrences even though the nodules measured more than 4 cm in diameter and/or there were more than three nodules^[61,62]. Open RFA can be indicated for patients who are considered suitable for open surgery with large, numerous, or deeply located tumors that cannot be accurately accessed by a laparoscopic approach. Furthermore, when patients have synchronous liver metastases, open surgical RFA can be performed in conjunction with resection of the primary cancer.

Local controllability (local tumor progression)

The local recurrence rate after RFA for HCC ranged from 1.7% to 41%^[63-70] (Table 2). As reported by Kudo^[28], in a series of 141 HCC patients who underwent curative RFA therapy, local tumor progression was observed in 9 cases (local tumor progression rate, 6.3%), whereas the cumulative local tumor progression rate, calculated by the Kaplan-Meier method, was 12% at 4 years. The rate may have depended on the size of nodules treated and the skill of the surgeons. There has not been any definitive report of local recurrence of nodules measuring 2-cm or smaller, and we ourselves have not encountered any case showing such recurrence, suggesting that recurrence in such cases is exceptional. The risk of local tumor progression increases with size, but the local tumor progression rate

Table 2 Studies comparing local tumor progression rates of radiofrequency ablation for hepatocellular carcinoma

Author	Yr	n	Tumor size (mean, cm)	Follow-up period (mean, mo)	Local tumor progression rate (%)
Rossi <i>et al</i> ^[63]	1996	41	2.3	22.6	5.0
Buscarini <i>et al</i> ^[64]	2001	60	-	26.8	14
Choi <i>et al</i> ^[65]	2004	53	2.1	23	21
Lu <i>et al</i> ^[66]	2005	87	2.5	12.7	5.8
Shiina <i>et al</i> ^[67]	2005	118	-	34.8	1.7
Solmi <i>et al</i> ^[68]	2006	63	2.8	32.3	41
Hänsler <i>et al</i> ^[69]	2007	21	4.2	-	21
Waki <i>et al</i> ^[70]	2010	88	-	36	4.8

differs markedly depending on whether or not a circumferential 5-mm safety margin is secured. In a meta-analysis of RFA *vs* PEI in HCC, the survival rate showed a significant benefit for RFA over PEI at 1, 2, 3 and 4 years^[71]. The survival advantage increased over time with Relative Risk values of: 1.28 (95% CI: 1.12-1.45) and 1.24 (95% CI: 1.05-1.48) for RFA *vs* PEI at 3- and 4-years, respectively. Likewise, RFA achieved significantly lower rates of local recurrence (RR: 0.37, 95% CI: 0.23-0.59)^[71].

Complications

Complications reported following percutaneous RFA of malignant liver tumors in 2320 patients treated at 41 different hospitals in Italy indicate that the mortality rate was 0.3% with an overall complication rate of 7.1%^[72,73]. The authors described major complications (2.4% incidence) including death, hemorrhage, RFA needle-track seeding, RFA lesion abscess, perforation of gastrointestinal viscus, liver failure, biloma, biliary stricture, portal vein thrombosis, and hemothorax or pneumothorax requiring drainage, and minor complications (4.7% incidence) including pain, fever, and asymptomatic pleural effusion. Another recent review indicated that complication rates for percutaneous, laparoscopic, and open RFA of hepatic tumors in 3670 patients were 7.2%, 9.5%, and 9.9%, respectively^[74]. Complications directly related to the liver included bleeding (1.6%), intrahepatic abscess (1.1%), biliary or hepatic vascular injury (1.7%), and liver failure (0.8%). Complications that arose in less than 1% of hepatic tumor RFA patients included pulmonary problems (pneumothorax, hydrothorax, pleural effusion), grounding pad skin burn, myoglobinemia or myoglobinuria, renal failure, coagulopathy, tumor seeding of the needle track, excessive hormone release from treated neuroendocrine tumors, cardiac problems (myocardial infarction, arrhythmia), and injury to the diaphragm or adjacent viscera. Although Llovet *et al*^[75] reported that dissemination along the puncture route was observed in 12.5% of their patients, only a few such cases have been reported in Japan, and dissemination may not occur at such a high frequency. This complication was almost absent in many reports from Japan^[28]. Overall, the frequency of major complications of percutaneous RFA was 0.6%-8.9%, which was higher than that of PEI, but generally lower than that of MCT^[28].

Some investigators have suggested that tumor location is closely related to the risk of major complications. Central tumors close to the hepatic hilum were reported to be unsuitable for percutaneous RFA because of the risk of injuring adjacent bile ducts^[15]. It was also suggested that RFA for nodules adjacent to large vessels might often result in incomplete necrosis because of a heat sink effect. In addition, peripheral tumors adjacent to extrahepatic organs were also suggested to be unsuitable because of the risk of heat injuries, such as intestinal perforation and pleural effusion^[72,76]. Thus, there may be difficulty with RFA of nodules in such high-risk locations, possibly resulting in complications or preventing adequate treatment. However, Teratani *et al*^[77] reported that there was no difference in early complication rates according to tumor location. The effort to achieve thorough ablation increased the total number of electrode insertions, and this may have led to an increase in complications.

To minimize complications of RFA for malignant liver tumors, knowledge of risk factors and prevention methods is required. In addition, because early and accurate diagnosis is necessary for the proper management of complications, not only radiologists but also hepatologists and surgeons should be familiar with the imaging features of each type of complication. Appropriate management of complications is essential for successful treatment with RFA.

CONCLUSION

RFA can be performed safely using percutaneous, laparoscopic, or open surgical techniques, and has markedly changed the treatment strategy for small HCC. RFA combined with TACE will likely make the treatment of larger tumors a clinically viable treatment alternative. Moreover, an accurate evaluation of treatment response is very important to secure successful RFA therapy. A sufficient safety margin can prevent local tumor recurrences. However, surgery is still the recommended treatment modality for patients with both primary hepatic malignancies. For inoperable lesions, RFA will likely play a significant role with a potential curative intent. Currently, the important clinical issue is that follow-up studies need to be performed for the early detection and treatment of recurrence, either locally or at different sites after RFA.

REFERENCES

- 1 El-Serag HB. Hepatocellular carcinoma: recent trends in the United States. *Gastroenterology* 2004; **127**: S27-S34
- 2 Kiyosawa K, Umemura T, Ichijo T, Matsumoto A, Yoshizawa K, Gad A, Tanaka E. Hepatocellular carcinoma: recent trends in Japan. *Gastroenterology* 2004; **127**: S17-S26
- 3 Di Bisceglie AM. Epidemiology and clinical presentation of hepatocellular carcinoma. *J Vasc Interv Radiol* 2002; **13**: S169-S171
- 4 McCaughan GW, Koorey DJ, Strasser SI. Hepatocellular carcinoma: current approaches to diagnosis and management. *Intern Med J* 2002; **32**: 394-400
- 5 Zavadsky KE, Lee YT. Liver metastases from colorectal carci-

- noma: incidence, resectability, and survival results. *Am Surg* 1994; **60**: 929-933
- 6 **Liu LX**, Zhang WH, Jiang HC. Current treatment for liver metastases from colorectal cancer. *World J Gastroenterol* 2003; **9**: 193-200
 - 7 **Tsim NC**, Frampton AE, Habib NA, Jiao LR. Surgical treatment for liver cancer. *World J Gastroenterol* 2010; **16**: 927-933
 - 8 **Michalski CW**, Erkan M, Hüser N, Müller MW, Hartel M, Friess H, Kleeff J. Resection of primary pancreatic cancer and liver metastasis: a systematic review. *Dig Surg* 2008; **25**: 473-480
 - 9 **Cho YK**, Kim JK, Kim WT, Chung JW. Hepatic resection versus radiofrequency ablation for very early stage hepatocellular carcinoma: a Markov model analysis. *Hepatology* 2010; **51**: 1284-1290
 - 10 **Rust C**, Gores GJ. Locoregional management of hepatocellular carcinoma. Surgical and ablation therapies. *Clin Liver Dis* 2001; **5**: 161-173
 - 11 **Lee WS**, Yun SH, Chun HK, Lee WY, Kim SJ, Choi SH, Heo JS, Joh JW, Choi D, Kim SH, Rhim H, Lim HK. Clinical outcomes of hepatic resection and radiofrequency ablation in patients with solitary colorectal liver metastasis. *J Clin Gastroenterol* 2008; **42**: 945-949
 - 12 **Mulier S**, Ruers T, Jamart J, Michel L, Marchal G, Ni Y. Radiofrequency ablation versus resection for resectable colorectal liver metastases: time for a randomized trial? An update. *Dig Surg* 2008; **25**: 445-460
 - 13 **Bartolozzi C**, Lencioni R. Ethanol injection for the treatment of hepatic tumours. *Eur Radiol* 1996; **6**: 682-696
 - 14 **Okada S**. Local ablation therapy for hepatocellular carcinoma. *Semin Liver Dis* 1999; **19**: 323-328
 - 15 **McGhana JP**, Dodd GD 3rd. Radiofrequency ablation of the liver: current status. *AJR Am J Roentgenol* 2001; **176**: 3-16
 - 16 **Shiina S**, Teratani T, Obi S, Hamamura K, Koike Y, Omata M. Nonsurgical treatment of hepatocellular carcinoma: from percutaneous ethanol injection therapy and percutaneous microwave coagulation therapy to radiofrequency ablation. *Oncology* 2002; **62** Suppl 1: 64-68
 - 17 **McGahan JP**, Brock JM, Tesluk H, Gu WZ, Schneider P, Browning PD. Hepatic ablation with use of radio-frequency electrocautery in the animal model. *J Vasc Interv Radiol* 1992; **3**: 291-297
 - 18 **McGahan JP**, Browning PD, Brock JM, Tesluk H. Hepatic ablation using radiofrequency electrocautery. *Invest Radiol* 1990; **25**: 267-270
 - 19 **Goldberg SN**, Gazelle GS, Halpern EF, Rittman WJ, Mueller PR, Rosenthal DI. Radiofrequency tissue ablation: importance of local temperature along the electrode tip exposure in determining lesion shape and size. *Acad Radiol* 1996; **3**: 212-218
 - 20 **Bruix J**, Sherman M, Llovet JM, Beaugrand M, Lencioni R, Burroughs AK, Christensen E, Pagliaro L, Colombo M, Rodés J. Clinical management of hepatocellular carcinoma. Conclusions of the Barcelona-2000 EASL conference. European Association for the Study of the Liver. *J Hepatol* 2001; **35**: 421-430
 - 21 **Ni Y**, Mulier S, Miao Y, Michel L, Marchal G. A review of the general aspects of radiofrequency ablation. *Abdom Imaging* 2005; **30**: 381-400
 - 22 **Ni Y**, Chen F, Mulier S, Sun X, Yu J, Landuyt W, Marchal G, Verbruggen A. Magnetic resonance imaging after radiofrequency ablation in a rodent model of liver tumor: tissue characterization using a novel necrosis-avid contrast agent. *Eur Radiol* 2006; **16**: 1031-1040
 - 23 **Mori K**, Fukuda K, Asaoka H, Ueda T, Kunitatsu A, Okamoto Y, Nasu K, Fukunaga K, Morishita Y, Minami M. Radiofrequency ablation of the liver: determination of ablative margin at MR imaging with impaired clearance of ferucarbotran—feasibility study. *Radiology* 2009; **251**: 557-565
 - 24 **Kim YS**, Rhim H, Cho OK, Koh BH, Kim Y. Intrahepatic recurrence after percutaneous radiofrequency ablation of hepatocellular carcinoma: analysis of the pattern and risk factors. *Eur J Radiol* 2006; **59**: 432-441
 - 25 **Lim HK**, Choi D, Lee WJ, Kim SH, Lee SJ, Jang HJ, Lee JH, Lim JH, Choo IW. Hepatocellular carcinoma treated with percutaneous radio-frequency ablation: evaluation with follow-up multiphase helical CT. *Radiology* 2001; **221**: 447-454
 - 26 **Chen MS**, Li JQ, Zheng Y, Guo RP, Liang HH, Zhang YQ, Lin XJ, Lau WY. A prospective randomized trial comparing percutaneous local ablative therapy and partial hepatectomy for small hepatocellular carcinoma. *Ann Surg* 2006; **243**: 321-328
 - 27 **Kudo M**. Radiofrequency ablation for hepatocellular carcinoma: updated review in 2010. *Oncology* 2010; **78** Suppl 1: 113-124
 - 28 **Kudo M**. Local ablation therapy for hepatocellular carcinoma: current status and future perspectives. *J Gastroenterol* 2004; **39**: 205-214
 - 29 **Lau WY**, Lai EC. Hepatocellular carcinoma: current management and recent advances. *Hepatobiliary Pancreat Dis Int* 2008; **7**: 237-257
 - 30 **Yamasaki T**, Kurokawa F, Shirahashi H, Kusano N, Hironaka K, Okita K. Percutaneous radiofrequency ablation therapy for patients with hepatocellular carcinoma during occlusion of hepatic blood flow. Comparison with standard percutaneous radiofrequency ablation therapy. *Cancer* 2002; **95**: 2353-2360
 - 31 **Yamakado K**, Nakatsuka A, Akeboshi M, Shiraki K, Nakano T, Takeda K. Combination therapy with radiofrequency ablation and transcatheter chemoembolization for the treatment of hepatocellular carcinoma: Short-term recurrences and survival. *Oncol Rep* 2004; **11**: 105-109
 - 32 **Peng ZW**, Chen MS, Liang HH, Gao HJ, Zhang YJ, Li JQ, Zhang YQ, Lau WY. A case-control study comparing percutaneous radiofrequency ablation alone or combined with transcatheter arterial chemoembolization for hepatocellular carcinoma. *Eur J Surg Oncol* 2010; **36**: 257-263
 - 33 **Uehara T**, Hirooka M, Ishida K, Hiraoka A, Kumagi T, Kikasa Y, Hiasa Y, Onji M. Percutaneous ultrasound-guided radiofrequency ablation of hepatocellular carcinoma with artificially induced pleural effusion and ascites. *J Gastroenterol* 2007; **42**: 306-311
 - 34 **Koda M**, Ueki M, Maeda Y, Mimura K, Okamoto K, Matsunaga Y, Kawakami M, Hoshio K, Murawaki Y. Percutaneous sonographically guided radiofrequency ablation with artificial pleural effusion for hepatocellular carcinoma located under the diaphragm. *AJR Am J Roentgenol* 2004; **183**: 583-588
 - 35 **Minami Y**, Kudo M, Kawasaki T, Chung H, Ogawa C, Shiozaki H. Percutaneous radiofrequency ablation guided by contrast-enhanced harmonic sonography with artificial pleural effusion for hepatocellular carcinoma in the hepatic dome. *AJR Am J Roentgenol* 2004; **182**: 1224-1226
 - 36 **Minami Y**, Kudo M, Kawasaki T, Chung H, Ogawa C, Inoue T, Sakaguchi Y, Sakamoto H, Shiozaki H. Percutaneous ultrasound-guided radiofrequency ablation with artificial pleural effusion for hepatocellular carcinoma in the hepatic dome. *J Gastroenterol* 2003; **38**: 1066-1070
 - 37 **Cioni D**, Lencioni R, Rossi S, Garbagnati F, Donati F, Crocetti L, Bartolozzi C. Radiofrequency thermal ablation of hepatocellular carcinoma: using contrast-enhanced harmonic power doppler sonography to assess treatment outcome. *AJR Am J Roentgenol* 2001; **177**: 783-788
 - 38 **Kudo M**. Imaging diagnosis of hepatocellular carcinoma and premalignant/borderline lesions. *Semin Liver Dis* 1999; **19**: 297-309
 - 39 **Ding H**, Kudo M, Onda H, Suetomi Y, Minami Y, Maekawa K. Hepatocellular carcinoma: depiction of tumor parenchymal flow with intermittent harmonic power Doppler US during the early arterial phase in dual-display mode. *Radiology* 2001; **220**: 349-356
 - 40 **Ding H**, Kudo M, Maekawa K, Suetomi Y, Minami Y, Onda

- H. Detection of tumor parenchymal blood flow in hepatic tumors: value of second harmonic imaging with a galactose-based contrast agent. *Hepatol Res* 2001; **21**: 242-251
- 41 **Kudo M.** Contrast harmonic ultrasound is a breakthrough technology in the diagnosis and treatment of hepatocellular carcinoma. *J Med Ultrasonics* 2001; **28**: 79-81
 - 42 **Ding H,** Kudo M, Onda H, Suetomi Y, Minami Y, Chung H, Kawasaki T, Maekawa K. Evaluation of posttreatment response of hepatocellular carcinoma with contrast-enhanced coded phase-inversion harmonic US: comparison with dynamic CT. *Radiology* 2001; **221**: 721-730
 - 43 **Minami Y,** Kudo M, Kawasaki T, Kitano M, Chung H, Maekawa K, Shiozaki H. Transcatheter arterial chemoembolization of hepatocellular carcinoma: usefulness of coded phase-inversion harmonic sonography. *AJR Am J Roentgenol* 2003; **180**: 703-708
 - 44 **Meloni MF,** Goldberg SN, Livraghi T, Calliada F, Ricci P, Rossi M, Pallavicini D, Campani R. Hepatocellular carcinoma treated with radiofrequency ablation: comparison of pulse inversion contrast-enhanced harmonic sonography, contrast-enhanced power Doppler sonography, and helical CT. *AJR Am J Roentgenol* 2001; **177**: 375-380
 - 45 **Quaia E,** Calliada F, Bertolotto M, Rossi S, Garioni L, Rosa L, Pozzi-Mucelli R. Characterization of focal liver lesions with contrast-specific US modes and a sulfur hexafluoride-filled microbubble contrast agent: diagnostic performance and confidence. *Radiology* 2004; **232**: 420-430
 - 46 **Jang HJ,** Kim TK, Burns PN, Wilson SR. Enhancement patterns of hepatocellular carcinoma at contrast-enhanced US: comparison with histologic differentiation. *Radiology* 2007; **244**: 898-906
 - 47 **Wang Z,** Tang J, An L, Wang W, Luo Y, Li J, Xu J. Contrast-enhanced ultrasonography for assessment of tumor vascularity in hepatocellular carcinoma. *J Ultrasound Med* 2007; **26**: 757-762
 - 48 **Leen E,** Angerson WJ, Yarmenitis S, Bongartz G, Blomley M, Del Maschio A, Summari V, Maresca G, Pezzoli C, Llull JB. Multi-centre clinical study evaluating the efficacy of SonoVue (BR1), a new ultrasound contrast agent in Doppler investigation of focal hepatic lesions. *Eur J Radiol* 2002; **41**: 200-206
 - 49 **Kono Y,** Lucidarme O, Choi SH, Rose SC, Hassanein TI, Alpert E, Mattrey RF. Contrast-enhanced ultrasound as a predictor of treatment efficacy within 2 weeks after transarterial chemoembolization of hepatocellular carcinoma. *J Vasc Interv Radiol* 2007; **18**: 57-65
 - 50 **Kudo M,** Minami Y. Radiofrequency ablation therapy under harmonic imaging guidance for the recurring cancer after local therapy for HCC: a randomized controlled study with RFA under B-mode guidance. *Ultrasound Med Biol* 2003; **29**: S145
 - 51 **Minami Y,** Kudo M, Kawasaki T, Chung H, Ogawa C, Shiozaki H. Treatment of hepatocellular carcinoma with percutaneous radiofrequency ablation: usefulness of contrast harmonic sonography for lesions poorly defined with B-mode sonography. *AJR Am J Roentgenol* 2004; **183**: 153-156
 - 52 **Minami Y,** Kudo M, Chung H, Kawasaki T, Yagyu Y, Shimono T, Shiozaki H. Contrast harmonic sonography-guided radiofrequency ablation therapy versus B-mode sonography in hepatocellular carcinoma: prospective randomized controlled trial. *AJR Am J Roentgenol* 2007; **188**: 489-494
 - 53 **Minami Y,** Kudo M. Contrast-enhanced harmonic ultrasound imaging in ablation therapy for primary hepatocellular carcinoma. *World J Radiol* 2009; **1**: 86-91
 - 54 **Minami Y,** Kudo M, Hatanaka K, Kitai S, Inoue T, Hagiwara S, Chung H, Ueshima K. Radiofrequency ablation guided by contrast harmonic sonography using perfluorocarbon microbubbles (Sonazoid) for hepatic malignancies: an initial experience. *Liver Int* 2010; **30**: 759-764
 - 55 **Santambrogio R,** Podda M, Zuin M, Bertolini E, Bruno S, Cornalba GP, Costa M, Montorsi M. Safety and efficacy of laparoscopic radiofrequency ablation of hepatocellular carcinoma in patients with liver cirrhosis. *Surg Endosc* 2003; **17**: 1826-1832
 - 56 **Okabayashi T,** Kobayashi M, Akimori T, Akisawa N, Iwasaki S, Onishi S, Araki K. Usefulness of laparoscopic radiofrequency ablation of hepatocellular carcinoma. *Surg Technol Int* 2005; **14**: 177-181
 - 57 **Ishiko T,** Beppu T, Sugiyama S, Masuda T, Takahashi M, Komori H, Takamori H, Hirota M, Kanemitsu K, Baba H. Radiofrequency ablation with hand-assisted laparoscopic surgery for the treatment of hepatocellular carcinoma in the caudate lobe. *Surg Laparosc Endosc Percutan Tech* 2008; **18**: 272-276
 - 58 **Schumacher G,** Eisele R, Spinelli A, Schmidt SC, Jacob D, Pratschke J, Neuhaus P. Indications for hand-assisted laparoscopic radiofrequency ablation for liver tumors. *J Laparoendosc Adv Surg Tech A* 2007; **17**: 153-159
 - 59 **Hirooka M,** Kisaka Y, Uehara T, Ishida K, Kumagi T, Watanabe Y, Abe M, Matsuura B, Hiasa Y, Onji M. Efficacy of laparoscopic radiofrequency ablation for hepatocellular carcinoma compared to percutaneous radiofrequency ablation with artificial ascites. *Dig Endosc* 2009; **21**: 82-86
 - 60 **Santambrogio R,** Opocher E, Montorsi M. Laparoscopic radiofrequency ablation of hepatocellular carcinoma: A critical review from the surgeon's perspective. *J Ultrasound* 2008; **11**: 1-7
 - 61 **Minami Y,** Kawasaki T, Kudo M, Haji S, Shiraishi O, Kawabe T, Yasuda C, Nakai T, Takeyama Y, Shiozaki H. Treatment of large and/or multiple hepatic malignancies: open surgical approaches of radiofrequency ablation. *Hepatogastroenterology* 2007; **54**: 2358-2360
 - 62 **Tanaka S,** Shimada M, Shirabe K, Taketomi A, Maehara S, Tsujita E, Ito S, Kitagawa D, Maehara Y. Surgical radiofrequency ablation for treatment of hepatocellular carcinoma: an endoscopic or open approach. *Hepatogastroenterology* 2009; **56**: 1169-1173
 - 63 **Rossi S,** Di Stasi M, Buscarini E, Quaretti P, Garbagnati F, Squassante L, Paties CT, Silverman DE, Buscarini L. Percutaneous RF interstitial thermal ablation in the treatment of hepatic cancer. *AJR Am J Roentgenol* 1996; **167**: 759-768
 - 64 **Buscarini L,** Buscarini E, Di Stasi M, Vallisa D, Quaretti P, Rocca A. Percutaneous radiofrequency ablation of small hepatocellular carcinoma: long-term results. *Eur Radiol* 2001; **11**: 914-921
 - 65 **Choi D,** Lim HK, Kim MJ, Lee SH, Kim SH, Lee WJ, Lim JH, Joh JW, Kim YI. Recurrent hepatocellular carcinoma: percutaneous radiofrequency ablation after hepatectomy. *Radiology* 2004; **230**: 135-141
 - 66 **Lu DS,** Yu NC, Raman SS, Lassman C, Tong MJ, Britten C, Durazo F, Saab S, Han S, Finn R, Hiatt JR, Busuttil RW. Percutaneous radiofrequency ablation of hepatocellular carcinoma as a bridge to liver transplantation. *Hepatology* 2005; **41**: 1130-1137
 - 67 **Shiina S,** Teratani T, Obi S, Sato S, Tateishi R, Fujishima T, Ishikawa T, Koike Y, Yoshida H, Kawabe T, Omata M. A randomized controlled trial of radiofrequency ablation with ethanol injection for small hepatocellular carcinoma. *Gastroenterology* 2005; **129**: 122-130
 - 68 **Solmi L,** Nigro G, Roda E. Therapeutic effectiveness of echo-guided percutaneous radiofrequency ablation therapy with a LeVeen needle electrode in hepatocellular carcinoma. *World J Gastroenterol* 2006; **12**: 1098-1104
 - 69 **Hänsler J,** Frieser M, Tietz V, Uhlke D, Wissniowski T, Bernatik T, Hothorn T, Hahn EG, Strobel D. Percutaneous radiofrequency ablation of liver tumors using multiple saline-perfused electrodes. *J Vasc Interv Radiol* 2007; **18**: 405-410
 - 70 **Waki K,** Aikata H, Katamura Y, Kawaoka T, Takaki S, Hiramatsu A, Takahashi S, Toyota N, Ito K, Chayama K. Percutaneous radiofrequency ablation as first-line treatment for small hepatocellular carcinoma: results and prognostic factors on

- long-term follow up. *J Gastroenterol Hepatol* 2010; **25**: 597-604
- 71 **Bouza C**, López-Cuadrado T, Alcázar R, Saz-Parkinson Z, Amate JM. Meta-analysis of percutaneous radiofrequency ablation versus ethanol injection in hepatocellular carcinoma. *BMC Gastroenterol* 2009; **9**: 31
- 72 **Livraghi T**, Solbiati L, Meloni MF, Gazelle GS, Halpern EF, Goldberg SN. Treatment of focal liver tumors with percutaneous radio-frequency ablation: complications encountered in a multicenter study. *Radiology* 2003; **226**: 441-451
- 73 **Curley SA**, Marra P, Beaty K, Ellis LM, Vauthey JN, Abdalla EK, Scaife C, Raut C, Wolff R, Choi H, Loyer E, Vallone P, Fiore F, Scordino F, De Rosa V, Orlando R, Pignata S, Daniele B, Izzo F. Early and late complications after radiofrequency ablation of malignant liver tumors in 608 patients. *Ann Surg* 2004; **239**: 450-458
- 74 **Mulier S**, Mulier P, Ni Y, Miao Y, Dupas B, Marchal G, De Wever I, Michel L. Complications of radiofrequency coagulation of liver tumours. *Br J Surg* 2002; **89**: 1206-1222
- 75 **Llovet JM**, Vilana R, Brú C, Bianchi L, Salmeron JM, Boix L, Ganaou S, Sala M, Pagès M, Ayuso C, Solé M, Rodés J, Bruix J. Increased risk of tumor seeding after percutaneous radiofrequency ablation for single hepatocellular carcinoma. *Hepatology* 2001; **33**: 1124-1129
- 76 **Meloni MF**, Goldberg SN, Moser V, Piazza G, Livraghi T. Colonic perforation and abscess following radiofrequency ablation treatment of hepatoma. *Eur J Ultrasound* 2002; **15**: 73-76
- 77 **Teratani T**, Yoshida H, Shiina S, Obi S, Sato S, Tateishi R, Mine N, Kondo Y, Kawabe T, Omata M. Radiofrequency ablation for hepatocellular carcinoma in so-called high-risk locations. *Hepatology* 2006; **43**: 1101-1108

S- Editor Cheng JX L- Editor Webster JR E- Editor Zheng XM

Shigeru Ehara, MD, Series Editor

Technological innovations in digital data management and changing roles of imaging specialists in Japan

Shigeru Ehara

Shigeru Ehara, Department of Radiology, Iwate Medical University School of Medicine, Morioka 020-8505, Japan

Author contributions: Ehara S contributed solely to this paper

Correspondence to: Shigeru Ehara, MD, Department of Radiology, Iwate Medical University School of Medicine, Morioka 020-8505, Japan. ehara@iwate-med.ac.jp

Telephone: +81-19-6515111 Fax: +81-19-6517071

Received: July 7, 2010 Revised: October 24, 2010

Accepted: October 31, 2010

Published online: November 28, 2010

Abstract

Technical innovations in digital data management pose a threat to radiologists in that can we remain in the process of clinical decision making or be assigned to a secondary role in future clinical practice. The value added to the imaging studies by diagnostic radiologists, or imaging specialists, has never been questioned more seriously.

© 2010 Baishideng. All rights reserved.

Key words: Radiology practice; Teleradiology

Peer reviewer: Thomas Deserno, PhD, Professor, Department of Medical Informatics, RWTH Aachen University, Pauwelsstr, 30, 52057 Aachen, Germany

Ehara S. Technological innovations in digital data management and changing roles of imaging specialists in Japan. *World J Radiol* 2010; 2(11): 425-426 Available from: URL: <http://www.wjgnet.com/1949-8470/full/v2/i11/425.htm> DOI: <http://dx.doi.org/10.4329/wjr.v2.i11.425>

CHANGING ROLES OF IMAGING SPECIALISTS

Radiologists used to be the first physician to access imag-

ing studies, and were in a position to control imaging studies. "Always be in Gemba (the actual place of patient care)" was the principle that all interns used to be taught during the first year of training. However, technological advances have made it possible for radiologists to work away from the radiology department. Teleradiology has enabled effective sharing of the increased workload on the one hand, but on the other hand, radiologists have started to lose control over the production of imaging data. Instead, referring physicians can more easily assess imaging data through picture archiving and communication systems, and imaging flow has started to bypass radiologists. Radiologists might be losing their role in clinical decision making.

In this context, the value added to the imaging studies by diagnostic radiologists, or imaging specialists, has never been more seriously in question^[1,2]. Radiologists are gatekeepers. By their presence in the process of diagnostic work-up, radiologists can propose the most effective way of diagnostic work-up. Radiologists are also guarantors of the quality of the overall medical care based on accurate imaging interpretation. To do this, radiologists must become more involved in direct patient management.

DECLINE AND FALL OF THE AMERICAN-STYLE RADIOLOGY BUSINESS MODEL

Radiologists in Japan have been struggling to establish the American-style radiology business model, which has been very successful with its efficiency and high rewards. It started in 1962, when the Johnson administration passed the Medicare bill. Since the radiologists' professional fee was included in Medicare part B, radiology practices became financially independent from hospital business. This reminds us of the fact that radiology practice entered into a different stage when Japan's National Health Insurance System introduced a radiologists' professional fee. That provided us with little room for hospital-independent practice.

However, this effective and profitable business model has been challenged by an increased demand for direct patient care and 24 h, 7 d a week coverage. The increased workload and manpower shortages have accelerated outsourcing of radiologist manpower. In addition, due to advanced digital imaging data management, referring physicians can proceed to clinical decision making without a radiologists' interpretation, and radiology reports are more likely to be handled as a commodity. When performing and interpreting imaging studies that occur in separate locations, commoditization of radiology reports has been accelerated. Patient-centered radiology is also a challenge to the traditional radiology business model, and radiologists might have to increase the time to cope with direct patient care, at least to some extent.

HOW WILL RADIOLOGISTS IN JAPAN SURVIVE?

Although academic radiology has relatively few differences in each country, the overall radiology practice is different, and depends on the national policy on healthcare, particularly in the balance of social welfare and healthcare industries for profit.

Japan's traditional socialized medicine has been functioning only in the process of social welfare^[3]. However, to date, there has been a little room for healthcare business for the hospital-based services including radiology, pathology and anesthesiology. A small number of pathologists started an independent anatomical pathology practice in their laboratories outside the hospital more than 10 years ago. Some pathologists might plan a larger business covering wider areas. A few anesthesiologists' groups have become independent from hospital practice, and have started working in the same or different hospitals with greater reward, although these still do not constitute the majority at present.

An increased number of radiologists are now starting office practice, using teleradiology as a tool. Such a trend has also changed our hospital practice. This is not limited to teleradiology, and types of practice can become more divergent or flexible using the current technology. One of the staff radiologists in my department works at home 1 d a week while taking care of her children. Since the worker can be anywhere in the world, such teleradiology business can be potentially border-less, but the problems of medical licensing still exist. The Ministry of Health, Labor and

Welfare of Japan and the Japanese Medical Association are keeping an eye on this issue.

FUTURE

Manpower shortage has always been a serious matter, and it has been accelerated by significantly increased imaging data. Current digital imaging management systems will certainly help us enhance our productivity. In addition, there is another factor that will change our working environment: physician-patient relationships. Traditional medical care is based on the patient and (sole) physician relationship, but this differs from current patient care. Since medical care provided by a team of specialists has now become common medical practice, the basic structure of medical care established by the traditional patient-physician relationship now needs to be redesigned. In this context, the status and the responsibilities of imaging specialists need to be better defined. It will certainly influence the status of radiologists.

Current advances in technology, including mass production of imaging data and digital data management systems, are not necessarily good for radiologists, for the following reasons. First, they are a cause of significant friction between human physiology and technology, although ergonomics research on, for example, visual display terminals might improve our working environment. Second, technological innovations in digital data management are now posing a threat to radiologists, and it is not clear whether we will keep our role in the process of clinical decision making or will be assigned to a secondary role in future clinical practice. However, I am confident that such technology-physiology friction and the workload-workforce imbalance will not persist for a long time. In the meantime, we should maximize our efficiency and maintain a high profile in clinical decision making. "Always be in Gemba" is still effective. The time to decide our future is now.

REFERENCES

- 1 **Patti JA**, Berlin JW, Blumberg AL, Bryan RN, Gaschen F, Izzi BM, Larson PA, Lewin JS, Liebscher LA. ACR white paper: the value added that radiologists provide to the health care enterprise. *J Am Coll Radiol* 2008; **5**: 1041-1053
- 2 **Lexa F**, Berlin JW, Boland GW, Smith GG, Jensen MD, Seidenwurm DJ, Hoppe R, Stroud R Jr. ACR White Paper: Task Force to Evaluate the Value Add Impact on Business Models. *J Am Coll Radiol* 2009; **6**: 681-693
- 3 **Ehara S**, Nakajima Y, Matsui O. Radiology in Japan in 2008. *AJR Am J Roentgenol* 2008; **191**: 328-329

S- Editor Cheng JX L- Editor Kerr C E- Editor Zheng XM

Pathophysiology of nephrogenic systemic fibrosis: A review of experimental data

Sameh K Morcos, John Haylor

Sameh K Morcos, Department of Diagnostic Imaging, Sheffield Teaching Hospitals NHS Foundation Trust, Sheffield S5 7AU, United Kingdom

John Haylor, Academic Department of Nephrology, University of Sheffield, Sheffield S5 7AU, United Kingdom

Author contributions: Morcos SK and Haylor J carried out the literature review and analysis; Morcos SK wrote the first draft; Haylor J provided the amendments and alterations.

Correspondence to: Sameh K Morcos, Professor, Department of Diagnostic Imaging, Sheffield Teaching Hospitals NHS Foundation Trust, Sheffield S5 7AU,

United Kingdom. sameh.morcos@sth.nhs.uk

Telephone: +44-114-2714339 Fax: +44-114-2611791

Received: June 13, 2010 Revised: September 30, 2010

Accepted: October 7, 2010

Published online: November 28, 2010

Morcos SK, Haylor J. Pathophysiology of nephrogenic systemic fibrosis: A review of experimental data. *World J Radiol* 2010; 2(11): 427-433 Available from: URL: <http://www.wjgnet.com/1949-8470/full/v2/i11/427.htm> DOI: <http://dx.doi.org/10.4329/wjr.v2.i11.427>

INTRODUCTION

Extracellular gadolinium contrast agents (Gd-CAs) are chelates containing the gadolinium ion (Gd^{3+}) which has been associated with the development of nephrogenic systemic fibrosis (NSF) in patients with a marked reduction in renal function^[1,2]. The epidemiology of NSF associated with Gd-CAs suggests that the stability of the Gd-chelate is an important factor in the pathogenesis of this condition^[3]. Stability refers to the relative tendency of the Gd^{3+} to remain coordinated (attached) to the chelating ligand. Free Gd^{3+} is highly toxic and can cause splenic degeneration, central lobular necrosis of the liver, enzyme inhibition, calcium channel blockade and a variety of haematological abnormalities^[3]. Therefore, it is crucially important that Gd^{3+} should be strongly attached to a ligand to avoid its toxic effects. The configuration of the Gd-CA molecule is either linear (gadopentetate, gadobenate, gadodiamide, gadoversetamide, gadofosveset and gadoxetate) or cyclic in which the Gd^{3+} ion is "caged" in the pre-organized cavity of the ligand (gadoterate, gadobutrol and gadoteridol), and are available as ionic (where the remaining carboxyl groups are saltified with meglumine or sodium) or non ionic (in which the number of carboxyl groups is reduced to three, neutralizing the three positive charges of the Gd^{3+}) preparations. There are differences in the chemical stability of these agents and, therefore, liability to release free gadolinium ions. The binding to Gd^{3+} is relatively weak in the non ionic linear molecule, whereas the cyclic molecule offers better protection and binding to Gd^{3+} . The physicochemical characteristics of Gd-CA available for clinical use are summarized in Table 1.

Abstract

Since the association between nephrogenic systemic fibrosis (NSF) and gadolinium contrast agents (Gd-CAs) was suggested in 2006, several experimental studies have been published to elucidate the role of these agents in the pathogenesis of NSF. Low stability Gd-CAs have a stimulant effect on human skin and fibroblasts in culture and modulate the production of collagen by these cells. Low stability agents have also induced NSF-like skin changes in a rat model with normal renal function after multiple repeat administrations. The role of the 5/6 subtotal nephrectomy rat model in investigating NSF remains under evaluation.

© 2010 Baishideng. All rights reserved.

Key words: Experimental models; Gadolinium-based contrast agents; Nephrogenic systemic fibrosis; Pathophysiology

Peer reviewers: Ahmed A Shokeir, MD, PhD, FEBU, Professor, Urology Department, Urology and Nephrology Center, Mansoura University, Mansoura 35516, Egypt; Mohamed Abou El-Ghar, MD, Department of Radiology, Urology and Nephrology center-Mansoura University, 72 El-gomhoria st, Mansoura, 35516, Egypt

Molecules of low stability are prone to undergo transmetallation with endogenous ions, leading to the release of free Gd ions (Gd^{3+}) which may deposit in tissues and initiate the process of fibrosis that characterises the condition NSF^[3]. Transmetallation is likely to occur if the elimination of low stability Gd-CAs molecules from the body is delayed. All Gd-CAs are eliminated from the body through the kidneys by glomerular filtration and the excretion half life is prolonged in patients with reduced renal function, enhancing the opportunity for both transmetalation and release of free Gd^{3+} ^[4]. Although the pathogenesis of NSF remains uncertain, data from experimental studies are accumulating to support the hypothesis of a causal relation between low stability Gd-CAs and NSF. In this chapter, experimental studies which have investigated the stability of Gd-CAs and their effects on fibroblasts and skin *in vitro* and *in vivo* will be critically evaluated.

STABILITY OF GD-CAS

Thermodynamic stability

The stability of a metal chelate is described as the equilibrium between the metal (M), its ligand (L) and the complex (ML) of the type: $[M] + [L] \rightleftharpoons [ML]$. The thermodynamic stability of Gd-CA is typically expressed as the thermodynamic stability constant ($\log K_{therm}$) measured at very basic condition (pH 11). The conditional thermodynamic stability constant ($\log K_{cond}$) is more appropriate than $\log K_{therm}$ to describe thermodynamic stability as it is measured at the physiological pH 7.4. As the thermodynamic and conditional stability constants reflect the affinity of gadolinium for its ligand, the higher these stability constants, the more stable the complex and less free Gd^{3+} ions and free ligand are present when sufficient time is allowed to reach thermodynamic equilibrium.

Kinetic stability

Kinetic stability reflects the speed of dissociation of the metal ligand complex and provides insight into the potential of *in vivo* dissociation^[5].

The kinetic stability of Gd-CAs, can be assessed by measuring the dissociation half life ($T_{1/2}$) under very acidic conditions (pH 1)^[5]. However, dissociation half life data of different Gd-CAs has been obtained from different laboratories making direct comparison between these agents rather difficult. A recent study evaluated the dissociation half life ($T_{1/2}$) of Gd-CAs under the same laboratory conditions, confirming the following order for kinetic stability: linear chelates < non-ionic macrocyclic chelates \leq ionic macrocyclic chelates (Table 2)^[6].

Transmetallation in vitro

Transmetallation of Gd-CAs leads to release of free gadolinium through replacement of the Gd^{3+} within the chelate molecule by another cation such as iron, copper, zinc or calcium^[3]. Transmetallation of Gd-CAs would be difficult if the attachment between the Gd ion and the chelate were strong. *In vivo*, zinc might have the potential to displace an amount of Gd^{3+} because its concentration

in the blood is relatively high (55-125 $\mu\text{mol/L}$) whereas, copper is present in low concentration (1-10 $\mu\text{mol/L}$) and calcium ions have low affinity to organic ligands^[3,7]. Iron ions are tightly bound by the storage proteins, ferritin and haemosiderin, and only a small amount is available for transmetallation with Gd^{3+} ^[7].

A validated and reliable *in vitro* relaxometric method has been used to evaluate the release of Gd^{3+} from gadolinium chelates^[8,9] in the presence of Zn^{2+} at pH 7.4. Three classes of Gd-CA were determined using this approach: (1) Macrocyclic chelates were characterized by very high kinetic stability; (2) Ionic linear chelates for which a moderate kinetic stability leads to significant decomplexation in the presence of Zn^{2+} (Gd-DTPA, Gd-EOB-DTPA, Gd-BOPTA); and (3) Non-ionic linear chelates which exhibited poor kinetic stability and the highest extent of decomplexation.

Clinical studies also demonstrated transmetallation between Gd-CAs and endogenous zinc ions. The non-ionic linear chelate, Gd-DTPA-BMA (Omniscan®, GE Healthcare, USA), caused a large increase in zinc excretion that was 3-fold higher than the zincuria induced by the ionic linear molecule, Gd-DTPA (Magnevist®, Bayer Healthcare, Germany), in patients undergoing contrast-enhanced MRI examinations. The presence of free ligand in Omniscan may have also contributed to the observed zincuria. No effect on zinc excretion was observed with the ionic macrocyclic, Gd-CA Gd-DOTA (Dotarem®, Guerbet, France)^[10].

Stability of Gd-CA in human serum

A recent study measured the release of free Gd^{3+} after addition of different Gd-CAs to human serum incubated at 37°C over 15 d. A highly sensitive high pressure liquid chromatography connected to mass spectrometry (HPLC-ICP-MS) method was used to differentiate between dissociated and complex-bound Gd. Early release of Gd was observed with the linear chelates which increased with time^[11]. The release induced by non-ionic linear chelates was 10-fold higher in comparison to ionic chelates. Marked release of Gd^{3+} from gadodiamide and gadoversetamide without excess ligand was observed from day one. The excess ligand in formulated Omniscan® and OptiMark® (Covidien, USA) offered early protection and chelated the released Gd^{3+} in the first 2 d, but by day 3 the level of free Gd^{3+} increased about 5-fold from < 0.5% at day one to almost 2.5%. The amount of Gd released from Omniscan® and OptiMark® at day 15 was almost 20% of the dose added compared with 2% for Magnevist®.

The addition of phosphate to serum markedly increased the release of Gd at day one by a factor of 100 with the non-ionic linear preparations and by a factor of 30 with the ionic linear chelates. At day 15, phosphate increased the amount of released Gd^{3+} from 20% to around 35% of the total dose of Omniscan® and OptiMark®. For Magnevist® the total amount of released Gd^{3+} did not change and remained at 2%, only the speed of the release was increased in day one to 2% and remained at this level up to day 15. No release of Gd^{3+} was observed with the

Table 1 General characteristics of currently marketed gadolinium chelates used for magnetic resonance imaging^[6]

Name	Acronym	Gd-DTPA	Gd-EOB-DTPA	Gd-BOPTA	MS325	Gd-DTPA-BMA	Gd-DTPA-BMEA	Gd-HP-DO3A	Gd-BT-DO3A	Gd-DOTA
	Generic name	Gadopentetate dimeglumine	Gadoxetic acid, disodium salt	Gadobenate dimeglumine	Gadofosveset, trisodium salt	Gadodiamide	Gadoverse-tamide	Gadoteridol	Gadobutrol	Gadoterate meglumine
	Trade name	Magnevistâ	Primovist®	MultiHanceâ	Vasovist®	Omniscanâ	OptiMARKâ	ProHanceâ	Gadovistâ	Dotaremâ
	Company	Bayer-Schering	Bayer-Schering	Bracco	EPIX	GE-Healthcare	Mallinckrodt	Bracco	Bayer-Schering	Guerbet
	Chemical structure	Open-chain	Open-chain	Open-chain	Open-chain	Open-chain	Open-chain	Macrocytic	Macrocytic	Macrocytic
	Charge	Ionic	Ionic	Ionic	Ionic	Nonionic	Nonionic	Nonionic	Nonionic	Ionic
	Concentration (M)	0.5	0.25	0.5	0.25	0.5	0.5	0.5	1	0.5
	Osmolality at 37°C (mOsm/kg H ₂ O)	1960	688	1970	825	789	1110	630	1603	1350
	Viscosity (mPa.s) at 37°C	2.9	1.19	5.3	2.06	1.4	2	1.3	4.96	2
	Formulation	Free DTPA (1 mmol/L)	Ca-EOB-DTPA (trisodium salt) (1.5 mmol/L)	No formulation	Fosveset (0.325 mmol/L)	Ca-DTPA-BMA (caldiamide) (Na ⁺ salt) (25 mmol/L)	Ca-DTPA-BMEA (Na ⁺ salt) (50 mmol/L)	[Ca-HP-DO3A] ₂ (Ca ²⁺ salt) (0.5 mmol/L)	Ca-BT-DO3A (Na ⁺ salt) (1.0 mmol/L)	No formulation
	Hydrophilicity (log P Butanol/water)	-3.16	-2.11	-2.33	-2.11	-2.13	N/A	-1.98	-2	-2.87
	log K _{therm}	22.1	23.5	22.6	22.06	16.9	16.6	23.8	21.8	25.6
	log K _{cond}	17.7	18.7	18.4	18.9	14.9	15	17.1	14.7	19.3
	Kinetic Stability ^a	Low	Medium	Medium	Medium	Low	Low	High	High	High

^aLow: long-time index < 0.3, Medium: Long-time index 0.49 to 0.86; High: Long-time index > 0.95. N/A: Not available.

macrocytic Gd-CAs even after the addition of phosphate to the serum^[11].

These data support the high stability of the macrocytic Gd-CAs and that the non-ionic linear chelates have the lowest stability. The ionic linear chelates have a moderately higher stability in comparison to the non-ionic linear preparations as they released only a small amount of free Gd³⁺ throughout the observation period^[11].

TISSUE RETENTION OF GD-CA

There are several factors *in vivo* such as endogenous ions, enzymes and other biological elements that may work simultaneously to dissociate the Gd-CA with unpredictable effects^[12]. Therefore, it has been suggested that *ex-vivo* data are not reliable to predict the behaviour of Gd-CA *in vivo* as the conditions under which these measurements are obtained are disparate from those found *in vivo*^[12].

Retention of gadolinium in tissues has been used to assess the stability of Gd-CAs *in vivo*. Once Gd³⁺ is dissociated from its ligand, it can deposit in body tissues and may persist for long periods of time. On the other hand, virtually all the injected water soluble undissociated chelate is eliminated from the body after 3 d in the presence of normal renal function. Therefore, most of the gadolinium detected in the body 5 d after administration of a Gd-CA is likely to be released from the chelate^[13]. Thus, the lower the stability of the Gd-CA, the higher the retention of gadolinium in tissues.

Tweedle *et al.*^[13] compared the percent injected doses (%ID)/g-tissue of ¹⁵³Gd-labelled contrast agents in sev-

eral organs in mice and rats, and found that Gd retention in tissues 2 wk after injection was 3 times greater following Omniscan compared to the ionic linear chelate, Magnevist®. Gd retention in tissues was minimal with the macrocytic agents, Dotarem® and ProHance® (Bracco, Italy). The long-term retention of gadolinium in the skin after intravenous administration of commercially available Gd-CAs has also been investigated in the normal rat. The contrast agents were injected daily at the dose of 2.5 mmol/kg bodyweight for 5 consecutive days. Skin biopsies were taken at various time points up to a year after the last injection to measure total gadolinium concentration using Inductively Coupled Plasma Mass Spectrometry (ICP-MS). Retention of gadolinium in the skin was found throughout the observation period which correlated with the Gd-CA stability. The amount of gadolinium retention in the skin followed the order: Omniscan® > OptiMark® > Magnevist®. Only a minimal amount of gadolinium retention was observed with the macrocytic agents^[14].

IN VITRO STUDIES

Edward *et al.*^[15] found that Omniscan® (10–500 µmol/L) stimulated proliferation of normal human skin fibroblasts in culture. However, since no proliferation was seen with Gd chloride, the response to Omniscan® was attributed to the Gd-chelate molecule rather than free Gd³⁺. However, the same group in a recent study demonstrated that Gd chloride can stimulate the proliferation of fibroblasts confirming a role for free Gd³⁺ in this effect^[16]. Serum from NSF patients stimulated the proliferation of normal

Table 2 Dissociation half life ($T_{1/2}$) of gadolinium contrast agent under the same laboratory conditions^[6]

Gd-CA	$T_{1/2}$, pH 1.2	$T_{1/2}$, pH 1	$T_{1/2}$, pH 1	$T_{1/2}$, pH 1 (Temp 250)
Temperature (°C)	370	370	250	
Dotarem [®] (Guerbet, France)	85 h	23 h	338 h	338 h
Gadovist [®] (Bayer Schering Pharma AG, Germany)	18 h	7 h	43 h	43 h
ProHance [®] (Bracco, Italy)	4 h	1.6 h	3.9 h	3.9 h
All linear chelates	ND	ND	< 5 s	< 5 s

Gd-CA: Gadolinium contrast agent.

human skin fibroblasts but had no effect on fibroblasts derived from NSF patients, suggesting that once activated, these fibroblasts can not be activated further^[15].

A subsequent study by Varani *et al*^[17], confirmed the stimulant effect of Omniscan[®] on the proliferation of human fibroblasts over a lower concentration range (0.5–25 $\mu\text{mol/L}$) with no proliferative effect on human keratinocytes. However, a proliferative response to Gd chloride was detected, an effect inhibited in the presence of the free ligand, DTPA. More stable Gd-CAs also induced proliferation but at a higher minimum concentration, 50 $\mu\text{mol/L}$ for Magnevist[®] and Multihance[®] (Bracco, Italy) and 25 mmol/L for the macrocyclic Prohance[®] (Bracco, Italy) a 100 000 higher concentration than Omniscan[®]. These data taken as a whole would support a role for released Gd^{3+} ions rather than the entire Gd chelate molecule in the proliferative effect of Gd-CA. An experiment to establish whether the response to Omniscan[®] can be inhibited in the presence of a large amount of free ligands to chelate released Gd^{3+} ions is warranted.

MATRIX SUBSTANCES

The effect of Gd-CAs on matrix protein synthesis *in vitro* is somewhat controversial, but they appear to modulate the synthesis of the enzymes that control collagen synthesis^[17]. Omniscan[®] has been shown to increase hyaluronan synthesis in cultured normal human dermal fibroblasts together with an enhanced immunostain for α -smooth muscle actin (α -SMA)^[15]. Human skin fibroblasts derived from patients with NSF released higher levels of hyaluronan and the procollagen metabolite, procollagen type-1 C-propeptide (CICP). They also showed positive immunostain for α -SMA. Interestingly, serum from NSF patients stimulated both collagen (up to 3.3-fold) and hyaluronan synthesis (up to 7-fold) in healthy skin fibroblasts compared to serum from either healthy volunteers or dialysis patients. However, NSF serum had little effect on skin fibroblasts derived from NSF patients, suggesting these fibroblasts had already been maximally stimulated. Edward *et al*^[15] concluded that the ability of Omniscan[®] to stimulate fibroblast growth, differentiation and matrix synthesis supported its role in the pathophysiology of NSF.

ANIMAL STUDIES *IN VIVO*

Cytokine production was investigated in the normal rat

injected with 2.5 mmol/kg per day of gadodiamide (Omniscan[®] without excess chelate) for up to 8 d once, three or 8 times. Animals were sacrificed 6 h after the last injection^[18]. Gadodiamide for up to 8 d increased vascular endothelial growth factor (VEGF), osteopontin (OPN) and TIMP-1 in serum collected 6 h after the last dose. VEGF enhances vascular permeability and promotes angiogenesis. OPN regulates macrophage activity in response to calcification, cell-matrix interaction and is a chemoattractant for dendritic cells and t-lymphocytes, while TIMP-1-inhibits extracellular matrix degradation.

Gadolinium was detected in the skin, liver and femur and the detected amount increased with the total injected dose of gadodiamide. Gadolinium deposition in tissues was proposed to initiate a physiological response similar to tissue calcification seen in patients with advanced chronic kidney disease. This includes upregulation of OPN, chemoattractants for macrophages and monocytes, and cytokines that increase the vascular permeability and modulate extra-cellular matrix synthesis^[18]. All animals injected with gadodiamide over 8 d developed macroscopic skin lesions (reddening, ulceration and scab formation). Dermal microscopic changes included cellular infiltration and thickening of the collagen fibres^[18].

MODELS OF NSF

Experimental studies using normal rats and rats with 5/6 subtotal nephrectomy have been carried out to investigate the association between Gd-CAs and NSF. The subtotal nephrectomy model was proposed to reproduce *in vivo* a comparable situation to that of patients with advanced chronic kidney disease.

Rat with normal renal function

Gd-CAs at the dose of 2.5 mmol/kg per day administered intravenously 5 d a week over 4 wk has been proposed to induce skin lesions consistent with human NSF^[19,20]. Skin lesions were observed as early as 8 d after starting non-formulated gadodiamide and 20 d after starting Omniscan[®] (with excess chelate). No skin lesions were observed with either the Omniscan[®] ligand, caldiumide (Ca-DTPA-BMA) or with Magnevist[®]. The incidence of skin lesions (ulceration, fibrosis, CD34+ cell infiltration and increased cellularity) was qualitatively associated with gadolinium concentrations in tissues. The highest Gd concentrations were found in animals that received either gadodiamide or

the less stable Gd-EDTA. These data support the concept that NSF-like skin lesions are associated with gadolinium release from low stability chelates^[19,20].

The induction of skin lesions by low stability Gd-CAs in this model, despite their short half-life (20 min) and rapid elimination, suggests that some dissociation of the Gd-CA and release of free Gd³⁺ may occur even in the presence of normal renal function. Frenzel *et al*^[11] showed that the dissociation of Omniscan® occurs from day one in human serum and the release of free Gd³⁺ increases with time. It is reasonable to conclude from these studies that multiple repeat injections of low stability Gd-CAs in the absence of renal impairment could lead to gradual accumulation of Gd³⁺ in tissues until it reaches a threshold level that triggers the fibrotic process. A previous study in man has shown that Gd³⁺ deposition in bone occurs in patients with normal renal function. In this study, the Gd³⁺ retention in bone with Omniscan® was 2-4 times more than ProHance®, a non-ionic macrocyclic Gd-CA^[21].

Rats with partial nephrectomy

Grant *et al*^[22] investigated the effects of Gd-CAs in partially nephrectomised rats, with a reported serum creatinine level twice that of healthy animals. Rats received a dose of 5 mmol/kg body weight of Omniscan®, Magnevist®, 1 mmol/kg body weight of gadodiamide or Gd chloride or 25 µmol/kg body weight of gadolinium citrate daily except weekends (total of 10 doses). Rats were sacrificed on day 15, 3 d after the last injection. Both gadodiamide (1 mmol/kg per day) and Omniscan® (5 mmol/kg per day) induced macroscopic and histological skin lesions. Skin lesions were greater and developed more rapidly in animals which received gadodiamide in comparison to those which received Omniscan® (gadodiamide + excess ligand) confirming initial beneficial effects of the excess ligand, caldiumide, in the Omniscan® preparation. No macroscopic or histological skin lesions were observed with Magnevist® or with the gadolinium salts, chloride or citrate. Grant *et al*^[22] concluded that the skin lesions detected did not represent NSF, due to absence of fibrosis and CD34 positive cells. The authors indicated that the ulcerative skin lesions were produced secondary to scratching precipitated by an allergic response since there was some elevation of plasma histamine and an increase in dermal mast cells. The possibility that the dermatological changes could be a reaction to Gd deposition in the skin was not considered. Interestingly, itching and macroscopic skin lesions were only observed in animals with a high skin Gd content and no acute inflammatory response was observed when the skin Gd content was low. However, we would agree only with the statement of Grant *et al*^[22] that the model described was not an animal model of NSF since: (1) Ulcerative skin lesions are not a feature of NSF in man and should not be used as the endpoint of detection in an animal model. Their presence may modify or obscure the microscopic and immunohistochemical features of NSF in the skin; (2) The development of NSF in the rat requires time and allowing only 3 d following

cessation of Gd-CA administration is too short for the detection of typical histological changes of NSF; and (3) The only immutable epidemiological feature of human NSF is renal impairment. Marked reduction in GFR was not demonstrated in the study by Grant *et al*^[22].

Grant *et al*^[22] also commented that Gd salts are not suitable for investigating the role of free Gd³⁺ *in vivo*. Free Gd³⁺ ions within the intravascular compartment following intravenous administration of Gd chloride/citrate will form insoluble salts with body anions such as phosphate and hydroxide. These insoluble Gd salts would be attached to plasma proteins forming colloid micro-emboli which in turn will be phagocytosed by the reticuloendothelial system, particularly in the liver and spleen causing toxic effects in these organs. According to Grant *et al*^[22], for Gd³⁺ to be delivered to the skin or other organs it has to be in a soluble form i.e. while it is still in the chelated form. We agree with this suggestion and believe that delay in excretion of the Gd-chelate molecules would allow time for their dissociation in the extravascular extracellular fluid leading to deposition of insoluble gadolinium salts in the skin and other organs. These salts could be phagocytosed by local macrophages precipitating the release of varieties of profibrotic cytokines. Boyd *et al*^[23] employing scanning electron microscopy and energy dispersive x-ray spectroscopy (SEM/EDS) demonstrated gadolinium deposition in association with calcium phosphate in the skin of patients affected with NSF. It is also probable that the released Gd³⁺ may penetrate local fibroblasts causing direct activation of these cells as shown in *in vitro* studies^[16,17]. It is less likely that the entire Gd-CA molecule, which is highly hydrophilic, would enter the cell.

Grant *et al*^[22] did not adequately discuss the importance of the stability of Gd-CA although there are several observations in the study to indicate that released Gd from the low stability Gd-CA, Omniscan®, is likely to be the culprit of the observed skin lesions. The study showed that the excess ligand in Omniscan® provided an initial protective effect which is mainly due to reducing transmetallation with endogenous ions and chelating released free Gd³⁺ ions. In addition, higher retention of gadolinium in the skin was found with gadodiamide and Omniscan® in comparison to the more stable Magnevist®. The authors indicated that analytical technique did not allow them to determine whether the gadolinium detected in tissue is released free Gd³⁺ or the whole Gd-chelate molecule. However, recent work by Abraham *et al*^[24] using SIMS ion microscopy has confirmed that gadolinium detected in skin is insoluble gadolinium precipitated with tissue anions.

CONCLUSION

Since a causal relation between low stability Gd-CAs and NSF was suggested in 2006, several experimental studies to elucidate this possible association have been published. However, there has been no consensus on the requirements of the ideal animal model of NSF. Initial studies by Sieber *et al*^[19,20] indicated that rats with normal

renal function receiving multiple large doses of a Gd-CA could be used as a suitable model for NSF. However, the model lacks an essential clinical feature of NSF which is a marked reduction in renal function. The animal model of a 5/6 subtotal nephrectomy was subsequently proposed to reproduce *in vivo* a comparable situation to that of patients with advanced chronic kidney disease. Reported experience with this model so far has been mixed, some authors concluded that it is not a suitable model of NSF^[22], while others have used the model to investigate long-term retention of Gd in tissues^[25]. In the authors view a good animal model of NSF should possess the following features: (1) Histological changes of the skin similar to those seen in human NSF^[26]: (a) dermal cellularity for monocytes and fibrocytes/fibroblasts; (b) thickness of collagen bundles with decreased interstitial space; and (c) fibroblast/fibrocyte markers including CD34, collagen and α -SMA; (2) Absence of macroscopic skin lesions; (3) Reduction in GFR, equivalent to stage 5 CKD in man; (4) Adequate time allowed after Gd-CA injection and before sacrifice; and (5) Quantitative assessment of skin collagen.

We have considerable experience in the use of rats following 5/6 subtotal nephrectomy and have recently reported a positive correlation between the reduction in renal function, the retention of gadolinium in tissues and histological response of the skin following a single intravenous dose of Omniscan[®]^[27]. More recently, we reported a differential response of Gd retention in tissues and histological changes in the skin between Dotarem and Omniscan in rats with subtotal nephrectomy, with high retention of Gd in the skin associated with increase in cell cellularity and collagen of the dermis following Omniscan. These changes were absent with the highly stable Dotarem^[28]. A recent report by other authors employing the subtotal nephrectomy model, found that the retention of Gd in tissues following Omniscan administration was mainly due to dechelated gadolinium^[29].

Finally, the role of lanthanides in stimulating fibrogenesis was identified more than 20 years ago^[30,31]. Current experimental data support the view that gadolinium released from low stability Gd-CAs is an important factor in promoting fibrosis, the predominant feature of NSF.

REFERENCES

- Grobner T. Gadolinium--a specific trigger for the development of nephrogenic fibrosing dermopathy and nephrogenic systemic fibrosis? *Nephrol Dial Transplant* 2006; **21**: 1104-1108
- Marckmann P, Skov L, Rossen K, Dupont A, Damholt MB, Heaf JG, Thomsen HS. Nephrogenic systemic fibrosis: suspected causative role of gadodiamide used for contrast-enhanced magnetic resonance imaging. *J Am Soc Nephrol* 2006; **17**: 2359-2362
- Morcos SK, Thomsen HS. Nephrogenic systemic fibrosis: more questions and some answers. *Nephron Clin Pract* 2008; **110**: c24-c31; discussion c32
- Morcos SK. Nephrogenic systemic fibrosis following the administration of extracellular gadolinium based contrast agents: is the stability of the contrast agent molecule an important factor in the pathogenesis of this condition? *Br J Radiol* 2007; **80**: 73-76
- Schmitt-Willich H. Stability of linear and macrocyclic gadolinium based contrast agents. *Br J Radiol* 2007; **80**: 581-582; author reply 584-585
- Port M, Idée JM, Medina C, Robic C, Sabatou M, Corot C. Efficiency, thermodynamic and kinetic stability of marketed gadolinium chelates and their possible clinical consequences: a critical review. *Biometals* 2008; **21**: 469-490
- Cacheris WP, Quay SC, Rocklage SM. The relationship between thermodynamics and the toxicity of gadolinium complexes. *Magn Reson Imaging* 1990; **8**: 467-481
- Laurent S, Elst LV, Copoix F, Muller RN. Stability of MRI paramagnetic contrast media: a proton relaxometric protocol for transmetallation assessment. *Invest Radiol* 2001; **36**: 115-122
- Laurent S, Elst LV, Muller RN. Comparative study of the physicochemical properties of six clinical low molecular weight gadolinium contrast agents. *Contrast Media Mol Imaging* 2006; **1**: 128-137
- Kimura J, Ishiguchi T, Matsuda J, Ohno R, Nakamura A, Kamei S, Ohno K, Kawamura T, Murata K. Human comparative study of zinc and copper excretion via urine after administration of magnetic resonance imaging contrast agents. *Radiat Med* 2005; **23**: 322-326
- Frenzel T, Lengsfeld P, Schirmer H, Hütter J, Weinmann HJ. Stability of gadolinium-based magnetic resonance imaging contrast agents in human serum at 37 degrees C. *Invest Radiol* 2008; **43**: 817-828
- Tweedle MF. "Stability" of gadolinium chelates. *Br J Radiol* 2007; **80**: 583-584; author reply 584-585
- Tweedle MF, Wedeking P, Kumar K. Biodistribution of radiolabeled, formulated gadopentetate, gadoteridol, gadoterate, and gadodiamide in mice and rats. *Invest Radiol* 1995; **30**: 372-380
- Pietsch H, Lengsfeld P, Jost G, Frenzel T, Hütter J, Sieber MA. Long-term retention of gadolinium in the skin of rodents following the administration of gadolinium-based contrast agents. *Eur Radiol* 2009; **19**: 1417-1424
- Edward M, Quinn JA, Mukherjee S, Jensen MB, Jardine AG, Mark PB, Burden AD. Gadodiamide contrast agent 'activates' fibroblasts: a possible cause of nephrogenic systemic fibrosis. *J Pathol* 2008; **214**: 584-593
- Edward M, Jardine AG, Burden AD, Newton BB. Assessment of the ability of gadolinium-based contrast agents to stimulate fibroblast proliferation: a possible link to nephrogenic systemic fibrosis. Conference Abstract of ECR, 2009
- Varani J, DaSilva M, Warner RL, Deming MO, Barron AG, Johnson KJ, Swartz RD. Effects of gadolinium-based magnetic resonance imaging contrast agents on human skin in organ culture and human skin fibroblasts. *Invest Radiol* 2009; **44**: 74-81
- Steger-Hartmann T, Raschke M, Riefke B, Pietsch H, Sieber MA, Walter J. The involvement of pro-inflammatory cytokines in nephrogenic systemic fibrosis - a mechanistic hypothesis based on preclinical results from a rat model treated with gadodiamide. *Exp Toxicol Pathol* 2009; **61**: 537-552
- Sieber MA, Pietsch H, Walter J, Haider W, Frenzel T, Weinmann HJ. A preclinical study to investigate the development of nephrogenic systemic fibrosis: a possible role for gadolinium-based contrast media. *Invest Radiol* 2008; **43**: 65-75
- Sieber MA, Lengsfeld P, Walter J, Schirmer H, Frenzel T, Siegmund F, Weinmann HJ, Pietsch H. Gadolinium-based contrast agents and their potential role in the pathogenesis of nephrogenic systemic fibrosis: the role of excess ligand. *J Magn Reson Imaging* 2008; **27**: 955-962
- White GW, Gibby WA, Tweedle MF. Comparison of Gd(DTPA-BMA) (Omniscan) versus Gd(HP-DO3A) (ProHance) relative to gadolinium retention in human bone tissue by inductively coupled plasma mass spectroscopy. *Invest Radiol* 2006; **41**: 272-278

- 22 **Grant D**, Johnsen H, Juelsrud A, Løvhaug D. Effects of gadolinium contrast agents in naïve and nephrectomized rats: relevance to nephrogenic systemic fibrosis. *Acta Radiol* 2009; **50**: 156-169
- 23 **Boyd AS**, Zic JA, Abraham JL. Gadolinium deposition in nephrogenic fibrosing dermopathy. *J Am Acad Dermatol* 2007; **56**: 27-30
- 24 **Abraham JL**, Chandra S, Thakral C, Abraham JM. SIMS imaging of gadolinium isotopes in tissue from Nephrogenic Systemic Fibrosis patients: Release of free Gd from magnetic resonance imaging (MRI) contrast agents. *Appl Surf Sci* 2008; **255**: 1181-1184
- 25 **Pietsch H**, Lengsfeld P, Steger-Hartmann T, Löwe A, Frenzel T, Hütter J, Sieber MA. Impact of renal impairment on long-term retention of gadolinium in the rodent skin following the administration of gadolinium-based contrast agents. *Invest Radiol* 2009; **44**: 226-233
- 26 **Cowper SE**, Rabach M, Girardi M. Clinical and histological findings in nephrogenic systemic fibrosis. *Eur J Radiol* 2008; **66**: 191-199
- 27 **Haylor JL**, Dencausse H, Vickers M, Idee JM, Slater D, Morcos SK. Increased skin cellularity following Omniscan in rats with reduced renal function. Conference Abstract of ECR, 2009
- 28 **Haylor JL**, Nutter F, Jestin G, Decausse A, Idee JM, Slater D, Morcos S. Comparing the effects of the gadolinium based contrast agents (GBCAs), gadoterate and gadodiamide, on tissue gadolinium retention and skin cellularity in rats with marked renal impairment. Conference Abstract of ECR, 2010
- 29 **Idee JM**, Fretellier N, Poveda N, Dencausse A, Jestin G, Wallon C, Hollenbeck C, Raynaud JS, ZCorot C. Comparative stability of nonionic linear and ionic macrocyclic gadolinium chelates in renally-impaired rats. Conference Abstract of ECR, 2010
- 30 **Evans CH**, Drouven BJ. The promotion of collagen polymerization by lanthanide and calcium ions. *Biochem J* 1983; **213**: 751-758
- 31 **Drouven BJ**, Evans CH. Collagen fibrillogenesis in the presence of lanthanides. *J Biol Chem* 1986; **261**: 11792-11797

S- Editor Cheng JX **L- Editor** Webster JR **E- Editor** Zheng XM

Peripheral dose measurement in high-energy photon radiotherapy with the implementation of MOSFET

Vassiliki Vlachopoulou, Georgia Malatara, Harry Delis, Kiki Theodorou, Dimitrios Kardamakis, George Panayiotakis

Vassiliki Vlachopoulou, Georgia Malatara, Harry Delis, George Panayiotakis, Department of Medical Physics, School of Medicine, University of Patras, 265 00 Patras, Greece

Kiki Theodorou, Department of Medical Physics, School of Medicine, University of Thessaly, 411 00 Larissa, Greece

Dimitrios Kardamakis, Department of Radiotherapy, School of Medicine, University of Patras, 265 00 Patras, Greece

Author contributions: Vlachopoulou V, Malatara G, Kardamakis D and Panayiotakis G contributed to the initial study concept and design; Vlachopoulou V, Malatara G, Delis H and Theodorou K performed the data acquisition and analyses; Vlachopoulou V, Delis H and Panayiotakis G drafted and revised the manuscript; all authors approved the final version of the submitted manuscript.

Supported by The Greek Central Council of Health (110K/93)
 Correspondence to: George Panayiotakis, PhD, Professor, Department of Medical Physics, School of Medicine, University of Patras, 265 00 Patras, Greece. panayiot@upatras.gr

Telephone: +30-2610-969131 Fax: +30-2610-996113

Received: March 22, 2010 Revised: July 20, 2010

Accepted: July 27, 2010

Published online: November 28, 2010

Abstract

AIM: To study the peripheral dose (PD) from high-energy photon beams in radiotherapy using the metal oxide semiconductor field effect transistor (MOSFET) dose verification system.

METHODS: The radiation dose absorbed by the MOSFET detector was calculated taking into account the manufacturer's Correction Factor, the Calibration Factor and the threshold voltage shift. PD measurements were carried out for three different field sizes (5 cm × 5 cm, 10 cm × 10 cm and 15 cm × 15 cm) and for various depths with the source to surface distance set at 100 cm. Dose measurements were realized on the central axis and then at distances (1 to 18 cm) parallel to the edge of the field, and were expressed as the percentage PD (% PD) with respect to the maximum dose (d_{max}).

The accuracy of the results was evaluated with respect to a calibrated 0.3 cm³ ionization chamber. The reproducibility was expressed in terms of standard deviation (s) and coefficient of variation.

RESULTS: % PD is higher near the phantom surface and drops to a minimum at the depth of d_{max} , and then tends to become constant with depth. Internal scatter radiation is the predominant source of PD and the depth dependence is determined by the attenuation of the primary photons. Closer to the field edge, where internal scatter from the phantom dominates, the % PD increases with depth because the ratio of the scatter to primary increases with depth. A few centimeters away from the field, where collimator scatter and leakage dominate, the % PD decreases with depth, due to attenuation by the water. The % PD decreases almost exponentially with the increase of distance from the field edge. The decrease of the % PD is more than 60% and can reach up to 90% as the measurement point departs from the edge of the field. For a given distance, the % PD is significantly higher for larger field sizes, due to the increase of the scattering volume. Finally, the measured PD obtained with MOSFET is higher than that obtained with an ionization chamber with percentage differences being from 0.6% to 34.0%. However, when normalized to the central d_{max} this difference is less than 1%. The MOSFET system, in the early stage of its life, has a dose measurement reproducibility of within 1.8%, 2.7%, 8.9% and 13.6% for 22.8, 11.3, 3.5 and 1.3 cGy dose assessments, respectively. In the late stage of MOSFET life the corresponding values change to 1.5%, 4.8%, 11.1% and 29.9% for 21.8, 2.9, 1.6 and 1.0 cGy, respectively.

CONCLUSION: Comparative results acquired with the MOSFET and with an ionization chamber show fair agreement, supporting the suitability of this measurement for clinical *in vivo* dosimetry.

© 2010 Baishideng. All rights reserved.

Key words: Radiotherapy; Peripheral dose; Metal oxide semiconductor field effect transistor; Dosimeter

Peer reviewer: Igor Meglinski, PhD, Head of Bio-Photonics and Bio-Medical Imaging, Cranfield Health, Cranfield University, Cranfield, Bedfordshire, MK43 0AL, United Kingdom

Vlachopoulou V, Malatara G, Delis H, Theodorou K, Kardamakis D, Panayiotakis G. Peripheral dose measurement in high-energy photon radiotherapy with the implementation of MOSFET. *World J Radiol* 2010; 2(11): 434-439 Available from: URL: <http://www.wjgnet.com/1949-8470/full/v2/i11/434.htm> DOI: <http://dx.doi.org/10.4329/wjr.v2.i11.434>

INTRODUCTION

With radiotherapy treatment modalities there is an increase in tumor cure rates, and additionally, there are a significant number of patients who are irradiated for benign diseases^[1]. During radiotherapy treatment with high-energy photon beams, a small fraction of the delivered dose is absorbed a few centimetres away from the irradiated field^[2]. This dose is known as peripheral dose (PD) and, compared to higher doses, the associated cancer risk is likely to be much lower but not insignificant^[3].

The risk for secondary cancer associated with low doses of ionizing radiation, especially appearing in long-term surviving patients, is gaining new interest every day^[4]. Dörr *et al*^[1] showed that the majority of secondary tumors within the margin region of the treatment volume (from 2.5 cm inside to 5 cm outside the margin of the planning target volume) received a dose less than 6 Gy. Brenner *et al*^[5] reported that there is a 40% increase in solid tumors in the lung after radiotherapy of the prostate, where the lung is receiving doses in the range of 0.5-1.0 Gy. Since there is no dose that is regarded as safe, assessment of PDs to radiosensitive tissue/organs, such as the breast, the gonads and the thyroid, is essential to determine the possible risk of late effects, such as secondary cancers that could appear in long-term surviving patients (e.g. pediatric patients)^[6,7]. In general, it is of extreme importance to calculate the PD down to the level of 0.1% of the central axis maximum dose (d_{max})^[8] and its determination has been the subject of extensive investigation^[2,9-20]. Metal oxide semiconductor field effect transistor (MOSFET) is used as a clinical dosimeter for radiotherapy beams, and mobileMOSFET seems to be the appropriate dose verification system^[21-30], since due to its small size it can be positioned very easily on the patient's skin, and can evaluate the delivered dose both at the target and at organs at risk^[21].

This paper aims to assess the PD in high-energy photon beam radiotherapy as a function of the distance from the edge of the field, the depth, the field size and the energy of the photon beam, while the overall accuracy has been investigated by comparing the derived experimental results to corresponding ones obtained with an ionization chamber. Additionally, the paper aims to investigate the reproducibility of the mobileMOSFET dose verification system with respect to the low PDs.

MATERIALS AND METHODS

The present study was carried out in the Radiotherapy Department of the University Hospital of Patras, where the measurements were made with 6 MV and 18 MV X-ray beams of an ELEKTA SLI linear accelerator. Thomson Nielsen's mobileMOSFET Dose Verification System (TN-RD-70-W) with standard sensitivity MOSFET dosimeter (TN-502 RD) were used for the dose measurements.

MobileMOSFET (TN-RD-70-W) is Best Medical Canada Ltd's mobile, battery-operated dose verification system. The system consists of PC-based user-interface software and one mobileMOSFET reader module. The mobileMOSFET reader was set up in the treatment room, connected to the dosimeters and the measurement circuitry was arranged. The measurement procedure was controlled by a PC using the mobileMOSFET software through an RS-232C cable or the provided wireless transceiver. The software provides a console on screen for the operator to perform all required actions in the dose measurements, such as reading, displaying, saving and printing results. MOSFET dosimeters were placed in a water phantom. The dose measurements were carried out by clicking the "start" and "read" buttons on the dose measurement screen^[31].

The MOSFET dosimeter was set at the high bias in order to achieve the highest sensitivity at lower doses. The first step of the study consisted of the calibration procedure, measuring the radiation sensitivity of the dosimeter under known conditions. Each dosimeter was placed on the central axis of the 6 MV and 18 MV photon beam at 10 cm depth inside a water phantom, with the irradiated field size set at 10 cm × 10 cm. The dosimeter received a nominal dose of 200 cGy and the output voltage of the reader was compared to the set level. The ratio of the measured voltage difference value (ΔV) to the radiation dose delivered determines the calibration factor (CF), also known as sensitivity. To improve the accuracy of the calibration procedure, the measurement was repeated four times and the average value of the CF was calculated.

The radiation dose absorbed by the MOSFET was calculated by the threshold voltage shift (ΔV) attributed to the irradiation, according to the formula: dose = CR × ΔV /CF.

Where CR is the manufacturer's Correction Factor which is equal to 1.

The threshold voltage shift is proportional to the dose deposited in the active volume of the MOSFET and increases linearly up to an inherent functional limit of 20 V, beyond which the voltage change is no longer proportional to the dose.

PD measurements

PD measurements were made in a water phantom with dimensions 54 cm × 52 cm × 30 cm. The field sizes at the surface of the phantom were set at 5 cm × 5 cm, 10 cm × 10 cm and 15 cm × 15 cm and the source to surface distance was set at 100 cm. A representative experimental arrangement is shown in Figure 1.

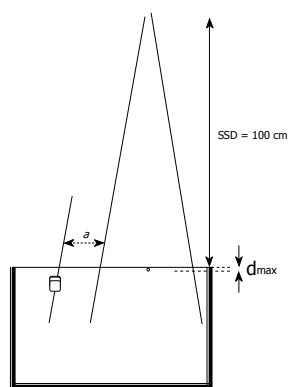


Figure 1 Geometry set-up of the peripheral dose measurements in a water phantom where a is the distance from the edge of the field (from 1 to 18 cm) where the MOSFET dosimeter was placed, and d_{\max} is 1.5 and 3.3 cm for 6 and 18 MV, respectively. This shape represents the MOSFET dosimeter.

Dose measurements were realized on the central axis and then in peripheral regions at several distances (1 to 18 cm) from the edge of the primary geometric field, and for various depths. All the results are expressed as the percentage PD (% PD) with respect to the d_{\max} of each field. Note that since the dimensions of the irradiated field increase with depth, due to the cone beam geometry, the axis of the PD measurements points (where the MOSFET dosimeter was placed) was not parallel to the central axis, but parallel to the edge of the field in order to keep the distance a from the edge of the primary field constant for all depths (Figure 1).

The % PD from the edge of the field was studied with respect to the field size and depth for 6 and 18 MV beams, and the results were evaluated for their accuracy against corresponding values obtained with a PTW 0.3 cm³ Unidos ionization chamber.

Each MOSFET was read immediately after exposure to minimize the potential effects of charge recombination and annealing and in order to achieve electronic stabilization^[27,28].

MOSFET reproducibility

The reproducibility of the dose measurements, which is a critical indicator for any dose verification system, was estimated. For different dose levels (4 for the early stage, and 6 for the late stage) the same measurement was repeated 6 times, and the shift voltage was measured. The standard deviation (s) which represents the reproducibility of each measurement, as well as the coefficient of variation (CV), were deduced according to the following formulae:

$$s = \sqrt{\frac{\sum_{i=1}^N (x_i - \bar{x})^2}{N-1}}$$

$$CV = \frac{s}{\bar{x}} \cdot 100\%$$

Where N is the number of measurements, x_i the dose measurement and \bar{x} the mean value of the measurements.

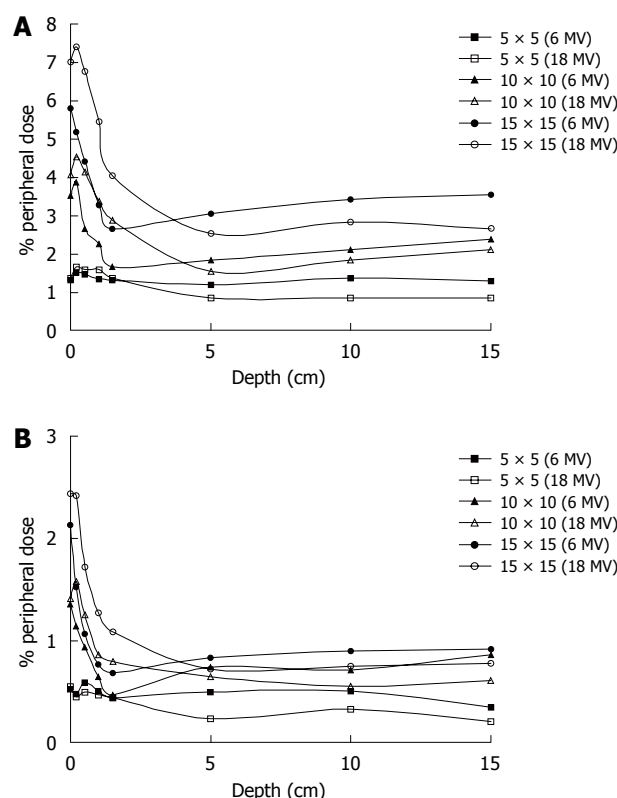


Figure 2 Effect of depth on percentage peripheral dose for 6 and 18 MV beams for various field sizes at (A) 5 cm off axis distance and (B) 15 cm off axis distance.

RESULTS

PD measurements

% PDs at distances of 5 and 15 cm from the field edge are presented as functions of the depth for both photon energies and for various field sizes (5 cm × 5 cm, 10 cm × 10 cm and 15 cm × 15 cm) in Figure 2A and B. From the curves it is obvious that the dose is higher near the surface and drops to a minimum at the depth of d_{\max} , and then the % PD tends to become constant with depth.

The variations of the % PD with distance from the field edge from 1 to 18 cm as a function of the field size and depth (0, 1.5 and 10.0 cm) for both energies are shown in Table 1.

The % PD decreases almost exponentially with the increase of distance. Figure 3 shows this behavior for the three field sizes and both energies (6 and 18 MV) while the same behavior of the % PD as a function of the depth (0, 0.2, 0.5, 1.0, 1.5, 5.0, 10.0 and 15.0 cm) can be noted in Figure 4.

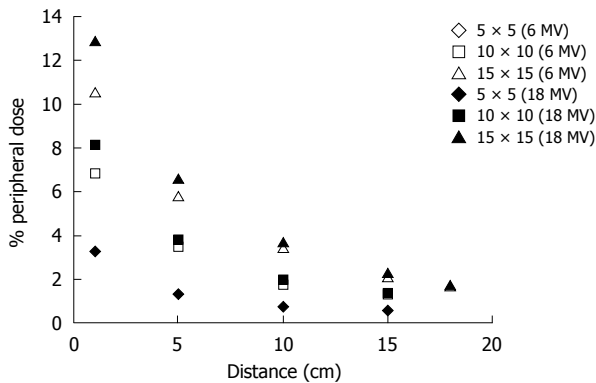
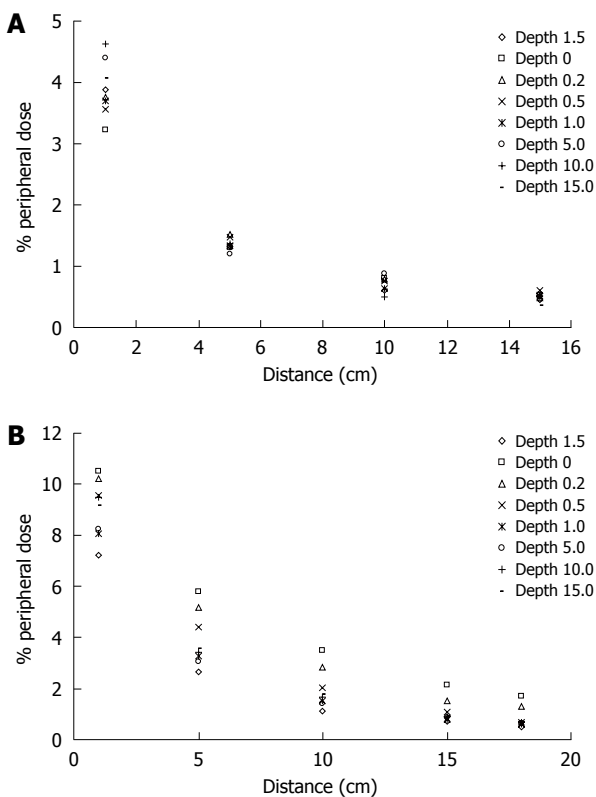
Finally, the accuracy of the mobileMOSFET dose verification system was evaluated by comparing PD measurements with corresponding measurements obtained with a PTW 0.3 cm³ ionization chamber and the results are represented in Figure 5A and B.

MOSFET reproducibility

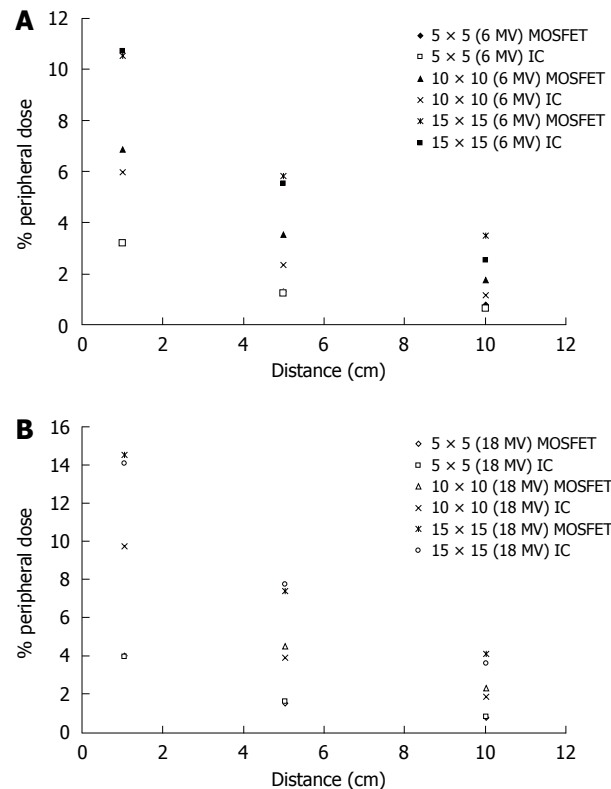
The MOSFET system, in high sensitivity mode, and in the early stage of its life (0-4000 mV) has a dose measurement

Table 1 Percentage peripheral dose measurements under various geometrical conditions

	Depth (cm)								
	0			1.5			10		
Distance (cm)	1	5	10	1	5	10	1	5	10
5 × 5 (6 MV)	3.22	1.30	0.79	3.88	1.32	0.59	4.64	1.36	0.49
5 × 5 (18 MV)	3.32	1.29	0.67	5.87	1.57	0.74	7.59	0.79	0.38
10 × 10 (6 MV)	6.84	3.53	1.75	6.03	1.65	0.89	7.59	2.11	1.28
10 × 10 (18 MV)	8.18	3.82	2.00	11.81	3.19	1.36	7.32	1.74	0.73
15 × 15 (6 MV)	10.52	5.80	3.48	7.23	2.64	1.10	9.52	3.41	1.66
15 × 15 (18 MV)	12.90	6.60	3.72	12.94	4.28	3.41	8.17	2.66	1.11

**Figure 3** Percentage peripheral dose at surface vs distance from the field edge for various field sizes and both energies.**Figure 4** Effect of distance on percentage peripheral dose, using the 6 MV beam, for various depths for (A) 5 cm × 5 cm and (B) 15 cm × 15 cm.

reproducibility of within 1.8%, 2.7%, 8.9% and 13.6% for 22.8, 11.3, 3.5 and 1.3 cGy dose assessments, respectively.

**Figure 5** Percentage peripheral dose obtained with metal oxide semiconductor field effect transistor and the ionization chamber for various field sizes as a function of distance from the surface using the (A) 6 MV and (B) 18 MV beam. MOSFET: Metal oxide semiconductor field effect transistor.

In the late stage of MOSFET life (> 18000 mV) the corresponding values change to 1.5%, 4.8%, 11.1% and 29.9% for 21.8, 2.9, 1.6 and 1.0 cGy, respectively (Figure 6).

Calibration Factor (CF) in the early stage of MOSFET life (0-4000 mV) has the value of 3.09 mV/cGy, in the middle stage of its life has the value of 2.90 mV/cGy and finally at the end of its lifetime the value is 2.80 mV/cGy.

DISCUSSION

From the curves of Figure 2A and B it is obvious that the PD is higher near the surface and drops to a minimum at the depth of d_{max} , and then the % PD tends to become constant with depth. Internal scatter radiation is the predominant source of PD and the depth dependence is determined by the attenuation of the primary photons^[14]. This is more evident away from the field edge. This might

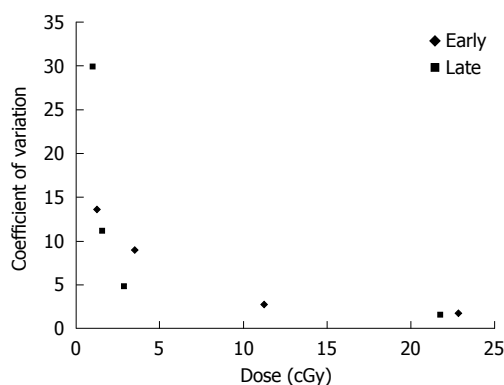


Figure 6 Coefficient of variation vs dose.

seem to be in disagreement with Fraass *et al.*^[20], who report that after d_{max} the PD increases with depth. However, in our measurements, as the field size increases with depth, the distance from the field edge is also displaced from the central axis, in order to stay constant with depth.

Closer to the field edge, where internal scatter from the phantom dominates, the PD increases with depth, because the ratio of the scatter to primary increases with depth. The fact that at d_{max} the % PD is minimized can also be observed from the measurements presented in Table 1, for the 6MV photon energy.

A few centimeters away from the field, where collimator scatter and leakage dominate, the PD decreases with depth, due to the attenuation by the water. This is in agreement with Francois *et al.*^[9].

The % PD decreases almost exponentially with the increase of distance. Figure 3 shows this behavior for the three field sizes and for both energies. The decrease of the % PD is more than 60% and can reach up to 90% as the measurement point departs from the edge of the field. For a given distance, the % PD is significantly higher for larger field sizes, due to the increase of the scattering volume.

The same behavior of the % PD as a function of the depth can be noted in Figure 4, where also the influence of the increase of the field size on the % PD can be observed. Figure 5A shows that the measured PD obtained with MOSFET is higher than that obtained with the ionization chamber in the case of the 6 MV beam at the surface, at three different distances (1.0, 5.0 and 10.0 cm) from the edge of the field, with percentage differences between corresponding values of the two dosimetric systems being from 0.6% to 34.0%. However, comparing with the central d_{max} this difference is less than 1%, which is in agreement with the findings of Butson *et al.*^[25]. Similar results arise for measurements obtained with the 18 MV beam, as shown in Figure 5B.

MOSFET reproducibility results as shown in Figure 6 are comparable to that obtained by Cheung *et al.*^[23]. Finally, from the measurements of Calibration Factor (CF) we conclude that after a large accumulated dose the detector requires larger doses for the same potential change.

The most important advantages of the mobileMOS-

FET dosimeter are its small size, as it can be easily placed on the patient's skin, and the almost direct estimation of the dose during exposure. Additionally, comparative results acquired with the MOSFET and with an ionization chamber show fair agreement, supporting the suitability of this measurement technique for clinical *in vivo* dosimetry, allowing radiation oncologists to evaluate and further optimize radiation treatment. Moreover, its sensitivity and reproducibility make it suitable for measurements of low PDs.

Regarding PD, these measurements show that a significant amount of the treatment dose reaching up to 14% of the central axis d_{max} , can be delivered to critical organs outside the treatment field at points near the primary field edge. Further studies are necessary to evaluate the clinical effects of this amount of dose and to develop appropriate solutions.

COMMENTS

Background

With radiotherapy treatment modalities there is an increase in tumor cure rates and additionally, there are a significant number of patients who are irradiated for benign diseases. During radiotherapy treatment with high energy photon beams, a small fraction of the delivered dose is absorbed a few centimeters away from the irradiated field. This dose is known as peripheral dose (PD) and compared to higher doses, the associated cancer risk is likely to be much lower but not insignificant.

Research frontiers

Many investigations have been carried out in order to measure PD in radiotherapy treatment modalities. *In vivo* dosimetry for radiotherapy patients often requires dose measurements not only in the treatment area, but also in the peripheral regions, so that doses to critical organs can be recorded and if possible minimized. For such measurements, there is a need for dosimeters with ability to measure low doses accurately and with tolerance to the variations of the spectral quality of the beam. Metal oxide semiconductor field effect transistor (MOSFET) features the ability to integrate dose measurements and to provide immediate dose readout. This, in combination with a very small sensing volume, makes the MOSFET dosimetry system advantageous over the other systems used in radiotherapy.

Innovations and breakthroughs

This study aims to assess the PD in high energy photon beam radiotherapy as a function of the distance from edge of the field, the depth, the field size and the energy of the photon beam using the mobileMOSFET dose verification system. The results are compared to corresponding ones obtained with an ionization chamber. Additionally, the reproducibility of the mobileMOSFET dose verification system is investigated, with respect to the low PDs. The small size, the radio-transparency, the high sensitivity and the immediate read make MOSFET dosimeters an excellent choice for dosimetry in radiotherapy, and when physical constraints, concerns over shadowing, or issues of scattered doses are important, then MOSFET dosimeters have clear advantages over both diodes and thermoluminescence dosimeters.

Applications

Since there is no dose that is considered as safe, assessment of PDs to radiosensitive tissue/organs, such as the breast, the gonads and the thyroid, is essential to determine the possible risk of late effects, such as secondary cancers that could appear in long-term surviving patients after the radiotherapy treatment. It is of extreme importance to calculate the PD down to a level of 0.1% of the central axis maximum dose and its determination has been the subject of extensive investigation.

Terminology

PD is the small fraction of the delivered radiotherapy dose that is absorbed a few centimeters away from the irradiated field MOSFET dosimeter is a MOSFET made of Si/SiO₂. It is used as a clinical dosimeter for radiotherapy beams. The MOSFET dosimeter is direct reading with a very thin (less than 2 mm) ac-

tive area. Calibration factor is the ratio of the recorded voltage difference value over the corresponding radiation dose delivered to the dosimeter.

Peer review

The paper can be published if some questions mentioned can be revised.

REFERENCES

- 1 Dörr W, Herrmann T. Cancer induction by radiotherapy: dose dependence and spatial relationship to irradiated volume. *J Radiol Prot* 2002; **22**: A117-A121
- 2 van der Giessen PH. Peridose, a software program to calculate the dose outside the primary beam in radiation therapy. *Radiother Oncol* 2001; **58**: 209-213
- 3 Brenner DJ, Doll R, Goodhead DT, Hall EJ, Land CE, Little JB, Lubin JH, Preston DL, Preston RJ, Puskin JS, Ron E, Sachs RK, Samet JM, Setlow RB, Zaider M. Cancer risks attributable to low doses of ionizing radiation: assessing what we really know. *Proc Natl Acad Sci USA* 2003; **100**: 13761-13766
- 4 Tubiana M, Aurengo A, Auerbeck D, Masse R. Recent reports on the effect of low doses of ionizing radiation and its dose-effect relationship. *Radiat Environ Biophys* 2006; **44**: 245-251
- 5 Brenner DJ, Curtis RE, Hall EJ, Ron E. Second malignancies in prostate carcinoma patients after radiotherapy compared with surgery. *Cancer* 2000; **88**: 398-406
- 6 Pierce DA, Preston DL. Radiation-related cancer risks at low doses among atomic bomb survivors. *Radiat Res* 2000; **154**: 178-186
- 7 Brenner DJ, Sachs RK. Estimating radiation-induced cancer risks at very low doses: rationale for using a linear no-threshold approach. *Radiat Environ Biophys* 2006; **44**: 253-256
- 8 Reissland JA. BEIR III 'The effects on populations of exposure to low levels of ionising radiation'. *J Soc Radiol Prot* 1981; **1**: 17-22
- 9 Francois P, Beurtheret C, Dutreix A. Calculation of the dose delivered to organs outside the radiation beams. *Med Phys* 1988; **15**: 879-883
- 10 McParland BJ, Fair HI. A method of calculating peripheral dose distributions of photon beams below 10 MV. *Med Phys* 1992; **19**: 283-293
- 11 Sherazi S, Kase KR. Measurements of dose from secondary radiation outside a treatment field: effects of wedges and blocks. *Int J Radiat Oncol Biol Phys* 1985; **11**: 2171-2176
- 12 van der Giessen PH. Calculation and measurement of the dose at points outside the primary beam for photon energies of 6, 10, and 23 MV. *Int J Radiat Oncol Biol Phys* 1994; **30**: 1239-1246
- 13 Van der Giessen PH. A simple and generally applicable method to estimate the peripheral dose in radiation teletherapy with high energy x-rays or gamma radiation. *Int J Radiat Oncol Biol Phys* 1996; **35**: 1059-1068
- 14 van der Giessen PH. Collimator-related radiation dose for different cobalt machines and linear accelerators. *Int J Radiat Oncol Biol Phys* 1996; **35**: 399-405
- 15 Van der Giessen PH. Measurement of the peripheral dose for the tangential breast treatment technique with Co-60 gamma radiation and high energy X-rays. *Radiother Oncol* 1997; **42**: 257-264
- 16 Van der Giessen PH, Bierhuizen HW. Comparison of measured and calculated peripheral doses in patients undergoing radiation therapy. *Radiother Oncol* 1997; **42**: 265-270
- 17 Starkschall G, St George FJ, Zellmer DL. Surface dose for megavoltage photon beams outside the treatment field. *Med Phys* 1983; **10**: 906-910
- 18 van der Giessen PH, Hurkmans CW. Calculation and measurement of the dose to points outside the primary beam for CO-60 gamma radiation. *Int J Radiat Oncol Biol Phys* 1993; **27**: 717-724
- 19 Diallo I, Lamon A, Shamsaldin A, Grimaud E, de Vathaire F, Chavaudra J. Estimation of the radiation dose delivered to any point outside the target volume per patient treated with external beam radiotherapy. *Radiother Oncol* 1996; **38**: 269-271
- 20 Fraass BA, van de Geijn J. Peripheral dose from megavolt beams. *Med Phys* 1983; **10**: 809-818
- 21 Consorti R, Petrucci A, Fortunato F, Soriani A, Marzi S, Iaccarino G, Landoni V, Benassi M. In vivo dosimetry with MOSFETs: dosimetric characterization and first clinical results in intraoperative radiotherapy. *Int J Radiat Oncol Biol Phys* 2005; **63**: 952-960
- 22 Rosenfeld AB. MOSFET dosimetry on modern radiation oncology modalities. *Radiat Prot Dosimetry* 2002; **101**: 393-398
- 23 Cheung T, Yu PKN, Butson MJ. Low-dose measurement with a MOSFET in high-energy radiotherapy applications. *Radiat Meas* 2005; **39**: 91-94
- 24 Ramani R, Russell S, O'Brien P. Clinical dosimetry using MOSFETs. *Int J Radiat Oncol Biol Phys* 1997; **37**: 959-964
- 25 Butson MJ, Cheung T, Yu PK. Peripheral dose measurement with a MOSFET detector. *Appl Radiat Isot* 2005; **62**: 631-634
- 26 Cherpak A, Studinski RC, Cygler JE. MOSFET detectors in quality assurance of tomotherapy treatments. *Radiother Oncol* 2008; **86**: 242-250
- 27 Oldham TR, McLean FB. Total ionizing dose effects in MOS oxides and devices. *IEEE Trans Nucl Sci* 2003; **50**: 483-499
- 28 Gladstone DJ, Lu XQ, Humm JL, Bowman HF, Chin LM. A miniature MOSFET radiation dosimeter probe. *Med Phys* 1994; **21**: 1721-1728
- 29 Tanyi JA, Krafft SP, Hagio T, Fuss M, Salter BJ. MOSFET sensitivity dependence on integrated dose from high-energy photon beams. *Med Phys* 2008; **35**: 39-47
- 30 Cygler JE, Saoudi A, Perry G, Morash C, E C. Feasibility study of using MOSFET detectors for in vivo dosimetry during permanent low-dose-rate prostate implants. *Radiother Oncol* 2006; **80**: 296-301
- 31 Thomson N. Operator's manual for the mobile MOSFET dosimetry system. Ottawa: Best Medical Canada Ltd., 2007

S- Editor Cheng JX L- Editor Logan S E- Editor Zheng XM

Multislice CT virtual intravascular endoscopy of aortic dissection: A pictorial essay

Zhonghua Sun, Yan Cao

Zhonghua Sun, Discipline of Medical Imaging, Department of Imaging and Applied Physics, Curtin University of Technology, Perth, Western Australia 6845, Australia

Yan Cao, Department of Medical Imaging, Shandong Medical College, Jinan 5460, Shandong Province, China

Author contributions: All authors contributed equally to this paper.

Correspondence to: Dr. Zhonghua Sun, Discipline of Medical Imaging, Department of Imaging and Applied Physics, Curtin University of Technology, GPO Box, U1987, Perth, Western Australia 6845, Australia. z.sun@curtin.edu.au

Telephone: +61-8-92667509 Fax: +61-8-92662377

Received: May 27, 2010 Revised: July 30, 2010

Accepted: August 6, 2010

Published online: November 28, 2010

Abstract

AIM: To present our experience of using 3D virtual intravascular endoscopy (VIE) to characterize and evaluate the intraluminal appearances of aortic dissection.

METHODS: Ten patients with known aortic dissection underwent dual-source computed tomography angiography and were included in the study. In addition to 2D axial and multiplanar reformatted images as well as 3D reconstructions, VIE images were created in each patient to demonstrate intraluminal views of the aorta and its branches, origin of artery branches and artery branch involvement by aortic dissection.

RESULTS: Stanford A dissection was found in 8 patients and B dissection in the remaining 2 patients. VIE images were successfully generated in all of the patients with excellent visualization of the normal anatomical structures, intimal flap and intimal entrance tear, communication between true and false lumens, as well as assessment of the extent of aortic dissection.

CONCLUSION: Our preliminary experience suggests that

VIE could be used as a complementary tool to assist radiologists accurately evaluate aortic dissection so that better patient management can be achieved.

© 2010 Baishideng. All rights reserved.

Key words: Aortic dissection; Computed tomography; 3D visualization; Virtual intravascular endoscopy

Peer reviewers: Ender Uysal, MD, Sisli Etfal Training and Research Hospital, Clinic of Radiology, Sisli Etfal Eğitim ve Araştırma Hastanesi Radyoloji Kliniği, Etfal sok. Sisli, Istanbul 34377, Turkey; Peter Gaines, Professor, Sheffield Vascular Institute, Northern General Hospital, Sheffield, S5 7AU, United Kingdom

Sun Z, Cao Y. Multislice CT virtual intravascular endoscopy of aortic dissection: A pictorial essay. *World J Radiol* 2010; 2(11): 440-448 Available from: URL: <http://www.wjgnet.com/1949-8470/full/v2/i11/440.htm> DOI: <http://dx.doi.org/10.4329/wjr.v2.i11.440>

INTRODUCTION

Aortic dissection is a common vascular disease and it is the most frequent cause of aortic emergency. Aortic dissection can be a life-threatening event which is characterized by splitting of the aortic wall by high blood pressure entering the media through an intimomedial entrance tear. Multislice computed tomography (CT) angiography is the preferred method for diagnosis of aortic dissection with a sensitivity and specificity of nearly 100%^[1,2]. CT has been shown to be more sensitive than invasive angiography and is comparable to MR imaging and transesophageal echocardiography for diagnosis of aortic dissection^[3,4].

Aortic dissection leads to formation of true and false lumens which are separated from each other by a flap of intimal lining and inner layers of media. Outer layers of the aortic media and adventitia form the outer wall of the

false lumen which is most commonly larger than the true lumen due to lack of outlet of blood flow. Differentiation between true and false lumens is important in the planning of percutaneous treatment with endovascular stent grafts or surgical repair of aortic dissections^[5,6]. It is crucial to identify the lumen of origin in major branch vessels such as coronary, carotid, renal and mesenteric arteries before treatment because viscera supplied by the false lumen are at risk when the false lumen is spontaneously or surgically occluded^[7]. The criteria to distinguish true from false lumens by CT have been previously described^[5,8]. In most of the cases, axial CT imaging supplemented by 2D or 3D reconstructions is able to identify the intimal flap which separates the true lumen from the false lumen and determine the type and extent of dissection; however, this may not be possible in all cases due to variable appearances resulting from different types of aortic dissection^[9,10].

3D virtual intravascular endoscopy (VIE) provides unique intraluminal views of the blood vessel and it has been previously reported to be valuable for assessment of aortic aneurysms and endovascular stent grafts^[11-13]. VIE has been shown to offer better understanding of the abnormalities of the aortic arch after endovascular repair^[14]; however, investigation of variable imaging appearances of aortic dissection by VIE visualization has not been studied before, to the best of our knowledge. The purpose of this paper is to demonstrate VIE findings in a group of patients diagnosed with aortic dissection. We present our experience of using VIE visualization in the assessment of aortic dissection with the aim of exploring the potential value of VIE for identification of the common and uncommon findings related to the aortic dissection with special focus on the identification of entry site or intimal tears of aortic dissection.

MATERIALS AND METHODS

Ten patients (7 men and 3 women, age range: 39-77 years, mean age: 55 years) with known aortic dissection were retrospectively included in this study. All patients underwent spiral CT angiography (CTA) which was performed with a dual-source CT scanner (Siemens, Definition, Forchheim, Germany). The scanning protocol was as follows: beam collimation 64 mm × 0.6 mm with slice thickness between 0.5-1.0 mm, pitch 1.0 with reconstruction interval of 50% overlap. Non-ionic contrast medium (Visipaque) with a total volume of 100 mL was injected intravenously *via* the antecubital vein at a flow rate of 4-6 mL/s, followed by 40-60 mL normal saline chasing. A bolus triggering technique was used with the region of interest placed at the proximal descending thoracic aorta and the triggering threshold was set at 120 HU to initiate the scan.

Aortic dissection was characterized based on 2D images as Stanford type A in 8 patients and type B dissection in the remaining 2 patients. In addition to 2D axial views, multiplanar reformation and 3D volume rendering including VIE images were generated in each patient.

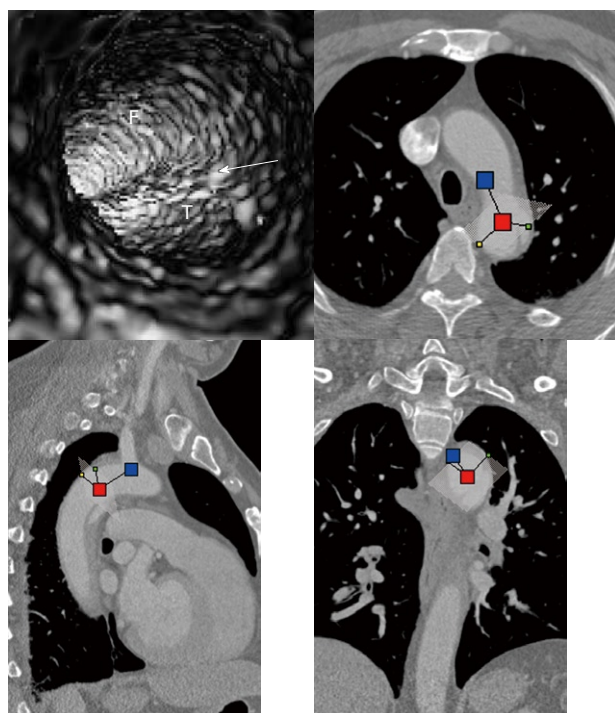


Figure 1 Virtual intravascular endoscopy visualization of the true lumen, false lumen and intimal flap (arrow) in a Stanford type B aortic dissection. Corresponding orthogonal views (axial, coronal and sagittal) confirm the location of virtual intravascular endoscopy position inside the false lumen (F) looking toward the true lumen (T) and intimal flap.

Since patients' details were removed from the DICOM data, and all of the images were anonymous during post-processing, there was no ethical issue involved so no IRB approval was required for the study.

Generation of VIE views

Multislice CT volume data were converted from original DICOM (Digital Imaging and Communication in Medicine) images using Analyze 7.0 (www.Analyzedirect.com). VIE images were generated based on a CT number thresholding technique to provide intraluminal views of the aorta and its branches as well as abnormal changes^[11,12]. VIE demonstration of both normal anatomical structures and pathological changes were determined by selecting an appropriate threshold value through measuring the CT attenuation at the aorta (either ascending or descending aorta or abdominal aorta). An upper threshold of 200-300 HU was applied to remove the contrast-enhanced blood from the aorta while keeping the artery wall intact without luminal disruption. Orthogonal views were referenced to assist VIE identification of the true and false lumens as well as intimal flap and entry site of aortic dissection (Figure 1).

Initially, it took about 30 min to produce VIE images for each patient. This includes a series of steps such as the conversion of DICOM images into volume data, image segmentation and generation of various VIE views of the aortic dissection. With experience gathered, the time was shortened to about 10-15 min for each case.

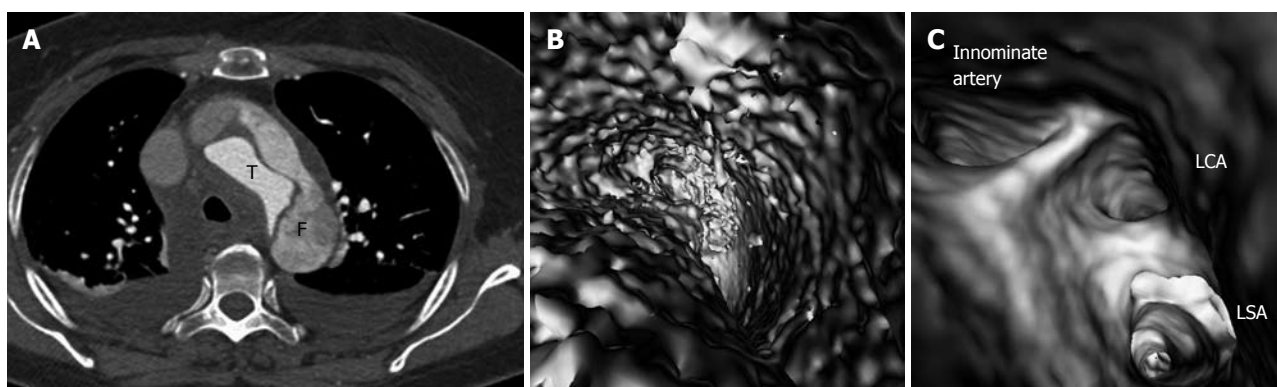


Figure 2 Stanford type A dissection with the true lumen smaller than the false lumen. The false lumen (F) has lower computed tomography (CT) attenuation than that in the true lumen (T) due to thrombus formation (A), thus a lower CT threshold (90 HU) was applied to view the false lumen intraluminally (B), while a higher CT attenuation (300 HU) was applied to demonstrate the true lumen. Corresponding virtual intravascular endoscopy (C) shows the involvement of three aortic branches by the dissection, namely left subclavian artery (LSA), left common carotid artery (LCA) and innominate artery when the view is positioned inside the false lumen. Bilateral pleural effusion is present on the 2D axial image.

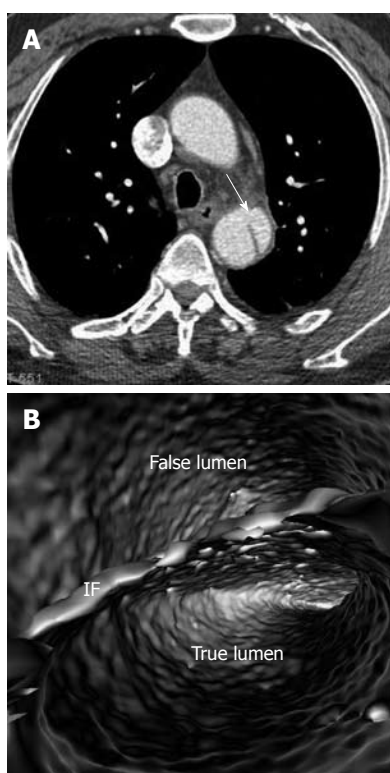


Figure 3 Stanford type B dissection with similar computed tomography attenuation in both true and false lumens (A). Virtual intravascular endoscopy clearly demonstrates the true and false lumens separated by the intimal flap (IF) in a single image (B). Arrow in A indicates the intimal flap.

RESULTS

Identification of true lumen and false lumen

In most cases, the false lumen is larger than the true lumen as once the blood enters the false lumen *via* an intimal tear it accumulates inside the lumen without any outlet. The false lumen then gradually becomes larger and compresses the true lumen which is in contact with the non-dissected portion of the aorta (Figure 2). A thrombus is frequently formed in the false lumen (Figure 2A), and this results in low CT attenuation when compared to the true lumen.

Therefore, for VIE visualization of true and false lumens, different CT thresholds need to be selected for demonstration of individual lumens clearly (Figure 2B).

Identification of intimal flap

The intimal flap is a soft tissue structure that separates the true lumen from the false lumen. The intimal flap can be seen in about 70% of cases in classic dissections^[1]. If the CT attenuation measured in the true lumen is similar to that measured in the false lumen, VIE is able to demonstrate both lumens separated by the intimal flap in a single image (Figure 3). However, in the majority of cases, contrast enhancement in the true lumen is higher than that in the false lumen, thus VIE visualization of these two lumens is normally presented in separate images as different thresholds are required to demonstrate individual lumens. This indicates that the intimal flap is not usually displayed on a single VIE image since different intraluminal views are generated by showing the individual lumens separately (either true lumen or false lumen) (Figure 2B and C).

If the false lumen is thrombosed, the intimal flap may be difficult to recognise on CT images; thus it is difficult to distinguish and differentiate acute dissection from mural thrombus or intramural hematoma (Figure 4A). The limitation of conventional visualizations can be overcome with intraluminal endoscopic views, even if in the presence of significantly stenosed lumens (Figure 4B and C).

Identification of intimal tear (entry site)

Identification of the accurate location of an intimomedial entrance tear is clinically important for diagnostic and therapeutic purposes. VIE is advantageous in this aspect as it enables generation of intraluminal views and clearly shows the communication between true and false lumens (Figure 5). In some complicated cases, VIE is able to confirm the entry site by navigating through the aorta and its branches including coronary branches (Figures 5 and 6). Moreover, VIE is able to determine the extent of the intimal tear which is believed useful for pre-operative evaluation of aortic dissection (Figures 5D and 6C).

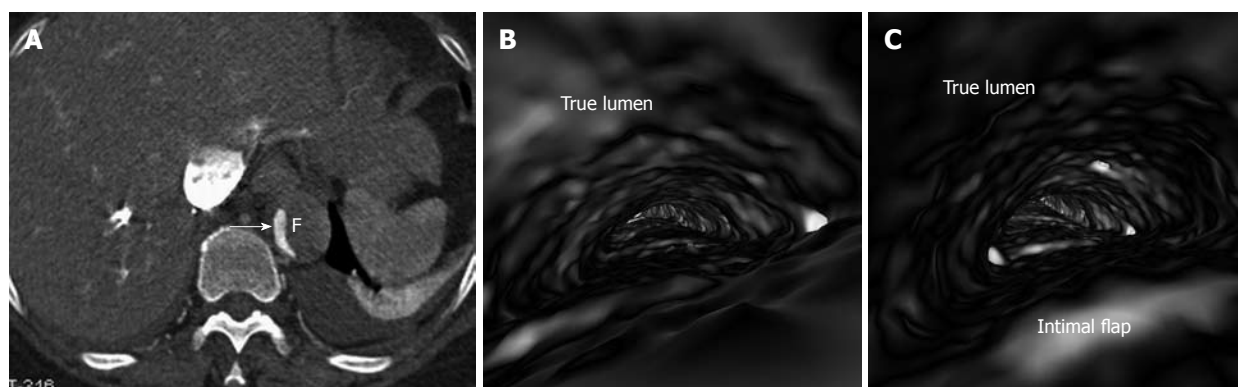


Figure 4 Stanford A dissection with abdominal artery branches involved. The false lumen (F) is thrombosed (A) with the true lumen being compressed to a much narrowed space. Virtual endoscopy views inside the true lumen clearly demonstrate the narrowed true lumen (B) and the intimal flap (C). Arrow in A indicates the true lumen.

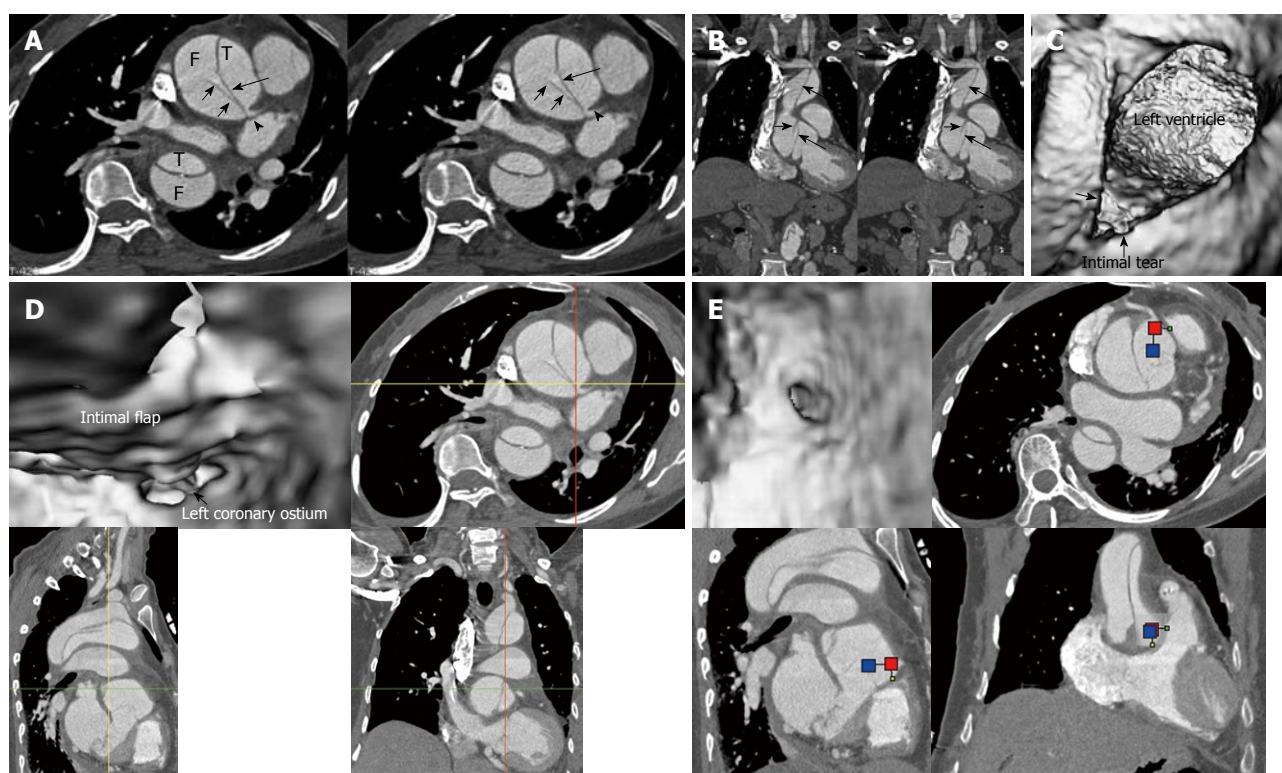


Figure 5 Stanford type A dissection with the dissection originating at the aortic root. The intimal flap is clearly displayed on 2D axial and coronal reformatted images (long arrows in A and B) with the left coronary artery arising from the true lumen (T) (arrowhead). Virtual intravascular endoscopy shows the intimal tear which is located at the aortic root (arrow in C) proximal to the left ventricle. Both of the coronary ostia arise from the true lumen with the intimal flap extending to the left coronary ostium (D, E). Short arrows in A and B indicate the cobweb sign in the false lumen (F).

Identification of vessel involvement by aortic dissection

Identification of vessel involvement by aortic dissection can be confirmed by 2D axial images in most situations (Figure 7A). VIE could be used as a complementary tool to 2D images in indeterminate cases, as virtual fly-through allows the viewers to follow the direction of dissection and identify whether the individual aortic branches are involved in the dissection (Figures 2B, 5D, 7B and 8). VIE assessment of vessel involvement is still possible even if in the presence of a severely narrowed true lumen due to compression by the false lumen (Figure 9).

Other findings of aortic dissection

In addition to the above-mentioned imaging findings related to the aortic dissection, there are other typical and atypical features which are also observed in aortic dissection. The slender linear areas of low attenuation that occasionally appear in the false lumen on CT images, known as the cobweb sign, are specific to the false lumen and may aid in its recognition (Figures 5 and 10). Another usual indication of the false lumen is the beak sign, which is an imaging manifestation of the wedge of hematoma that cleaves a space for the propagation of the false lumen

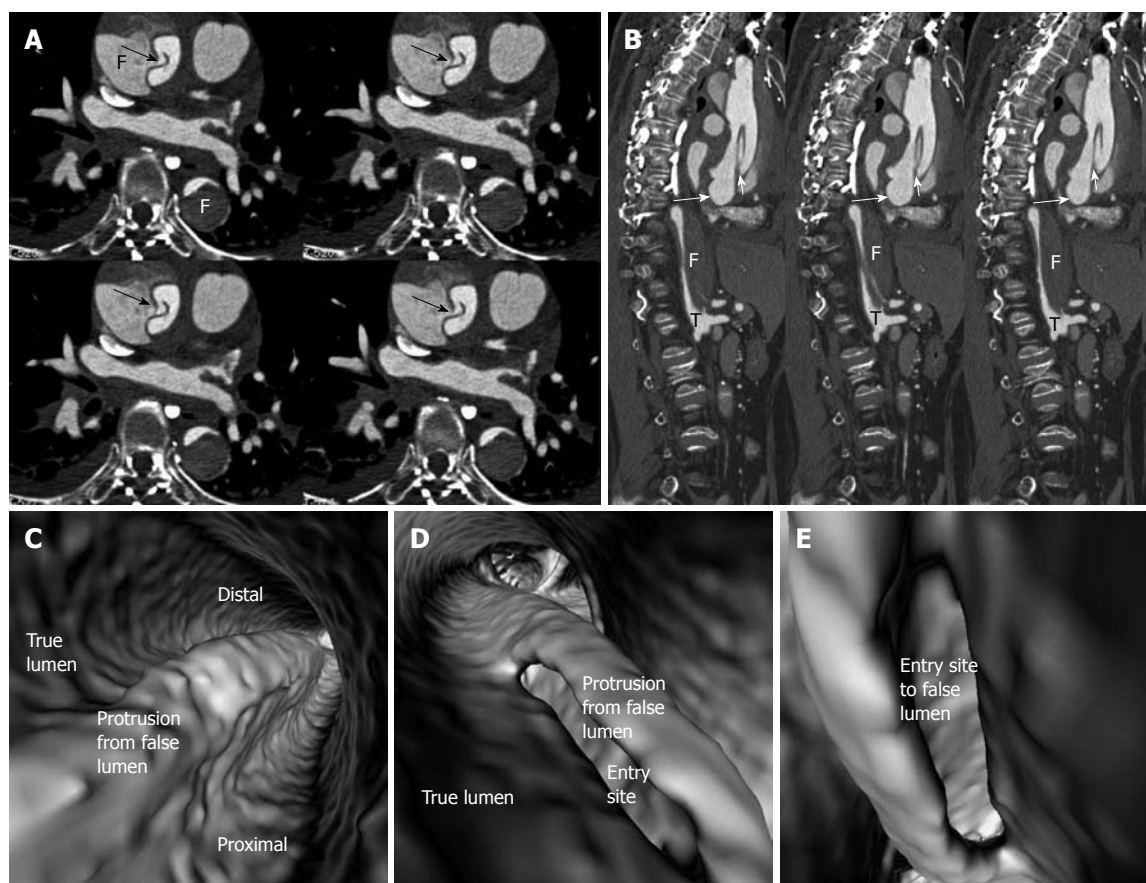


Figure 6 Stanford type A dissection with direct communication between the true lumen and false lumens (arrows in A). The true lumen (T) was obviously narrowed due to compression by the false lumen (F) with thrombus formed in the false lumen as shown on the sagittal reformatted image (B). The intimal flap (short arrows in B) arises from the level of the left ventricle (long arrows in B); C: A protrusion sign was observed on virtual intravascular endoscopy (VIE) images; D, E: The long intimal tear was identified at the ascending aorta posterior to the protrusion from the false lumen on different VIE visualizations. Pleural effusion is present at both sides on 2D axial images.



Figure 7 Stanford type A dissection with involvement of the three main artery branches on 2D axial image (A). Virtual intravascular endoscopy confirms that these three branches arise from the narrowed true lumen (B). Arrows in A indicate the intimal flap. LSA: Left subclavian artery; LCA: Left common carotid artery; IA: Innominate artery.

(Figure 11). The beak sign is a characteristic feature of the false lumen. These two findings can be easily identified and confirmed on 2D axial images, while VIE visualization does not present with characteristic features.

Intimointimal intussusception is an unusual manifestation of aortic dissection caused by circumferential dissection of the intimal layer^[1]. In intimointimal intussusception, CT scans may show one lumen wrapped around the other lumen in the aortic arch or descending aorta, with the in-

ner lumen always being the true lumen (Figure 12A). VIE clearly shows the central true lumen surrounded by the peripheral false lumen *via* two intimal flaps (Figure 12B), and the intraluminal visualization is enhanced by virtual fly-through viewing.

DISCUSSION

The principal complications of aortic dissection are car-

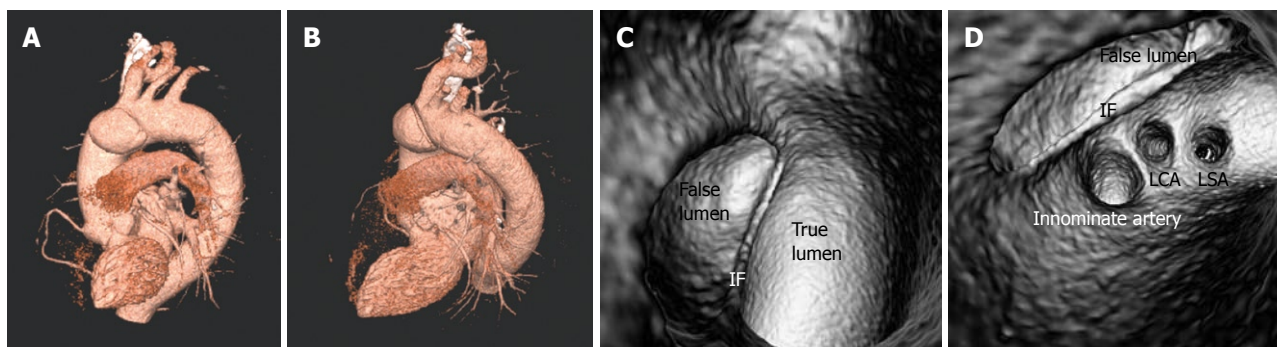


Figure 8 Stanford type A dissection is restricted to the ascending aorta on 3D volume rendering images (A, B). Both true and false lumens are clearly demonstrated on virtual intravascular endoscopy (VIE) visualization and these two lumens are separated by an intimal flap (IF) (C). The three main artery branches are perfused by the true lumen as shown on VIE view (D). LSA: Left subclavian artery; LCA: Left common carotid artery.

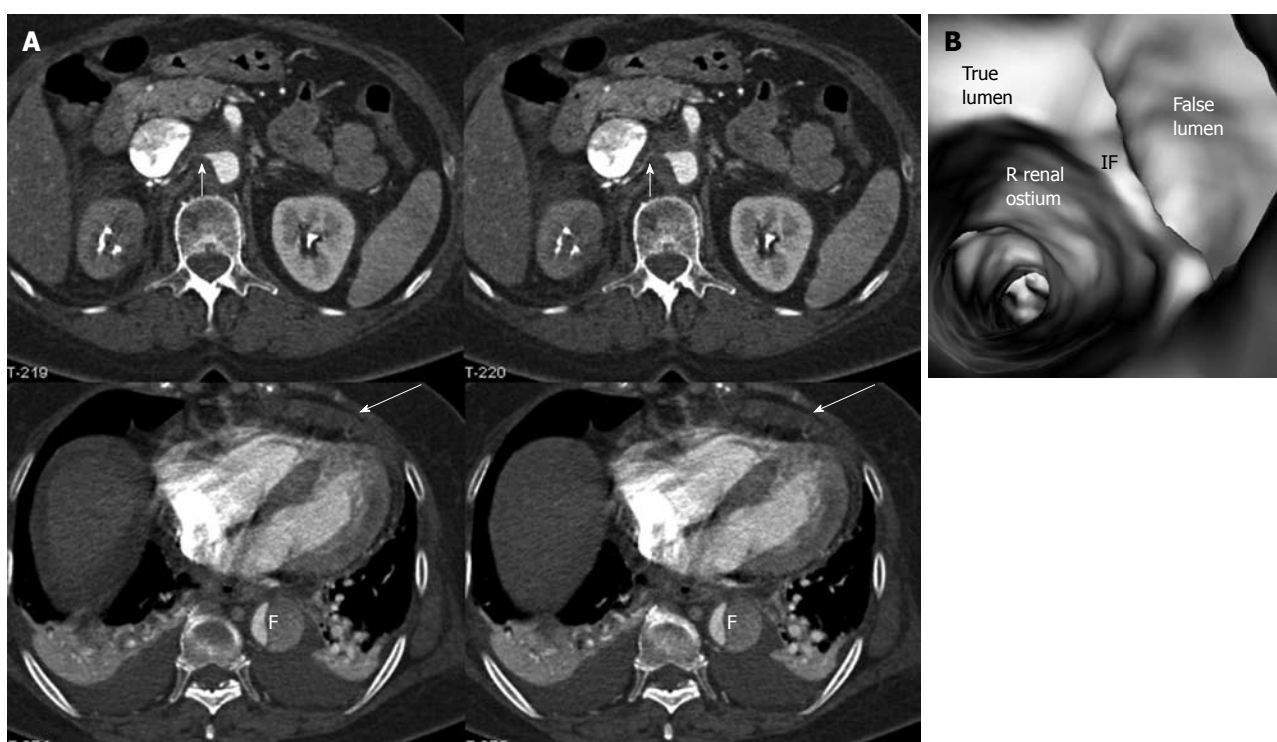


Figure 9 Stanford type B dissection with the true lumen much smaller than the false lumen. The right renal artery arises from the compressed true lumen resulting in right renal infarction (A). Virtual intravascular endoscopy confirms the origin of the right renal ostium coming from the true lumen which is separated from the false lumen (F) by an intimal flap (IF) (B). Short arrows in A indicate the right renal artery, while long arrows in A refer to pericardial effusion. Pleural effusion is also present at both sides.

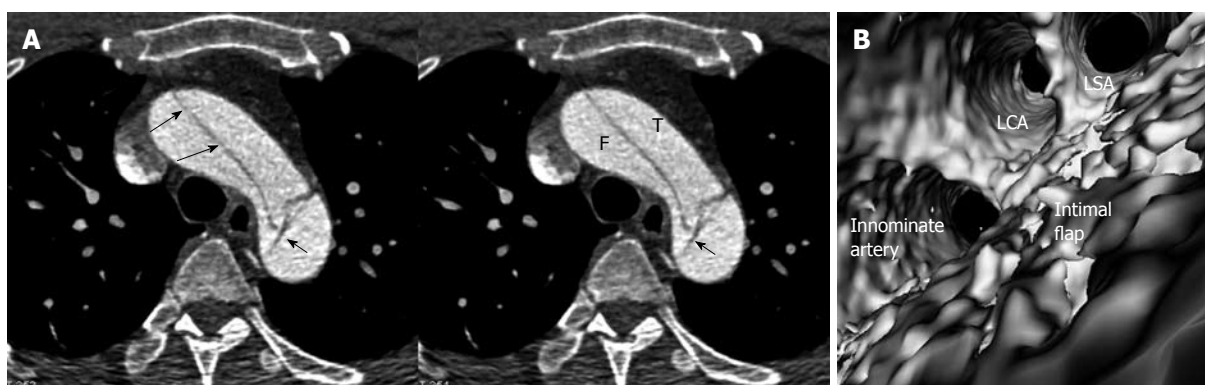


Figure 10 Stanford type A dissection with three aortic branches arising from the true lumen. An irregular intimal flap is displayed on virtual intravascular endoscopy visualization (B). A cob-web sign (short arrows) is noticed in the false lumen (F) on 2D axial image (A). Long arrows indicate the intimal flap. T: True lumen; LSA: Left subclavian artery; LCA: Left common carotid artery.

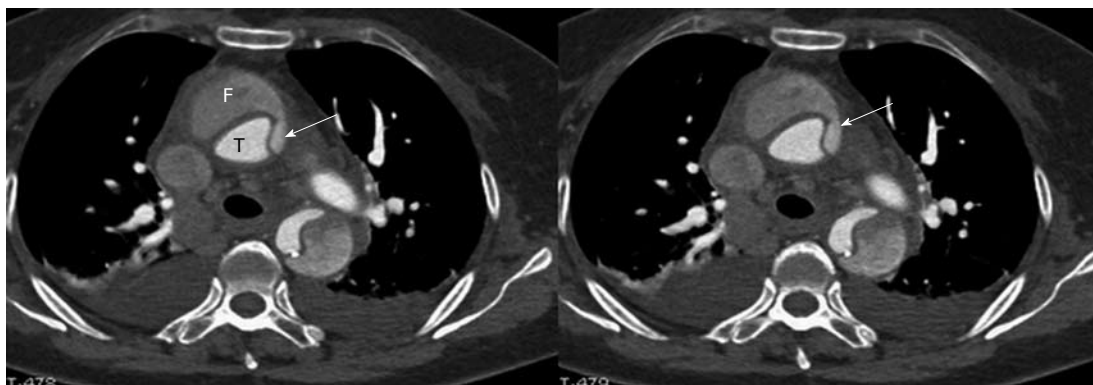


Figure 11 Stanford type A dissection with appearance of a beak sign (arrows) extending from the false lumen to surround the true lumen. The true lumen (T) is smaller than the false lumen (F). Bilateral pleural effusion is also noticed on 2D images.

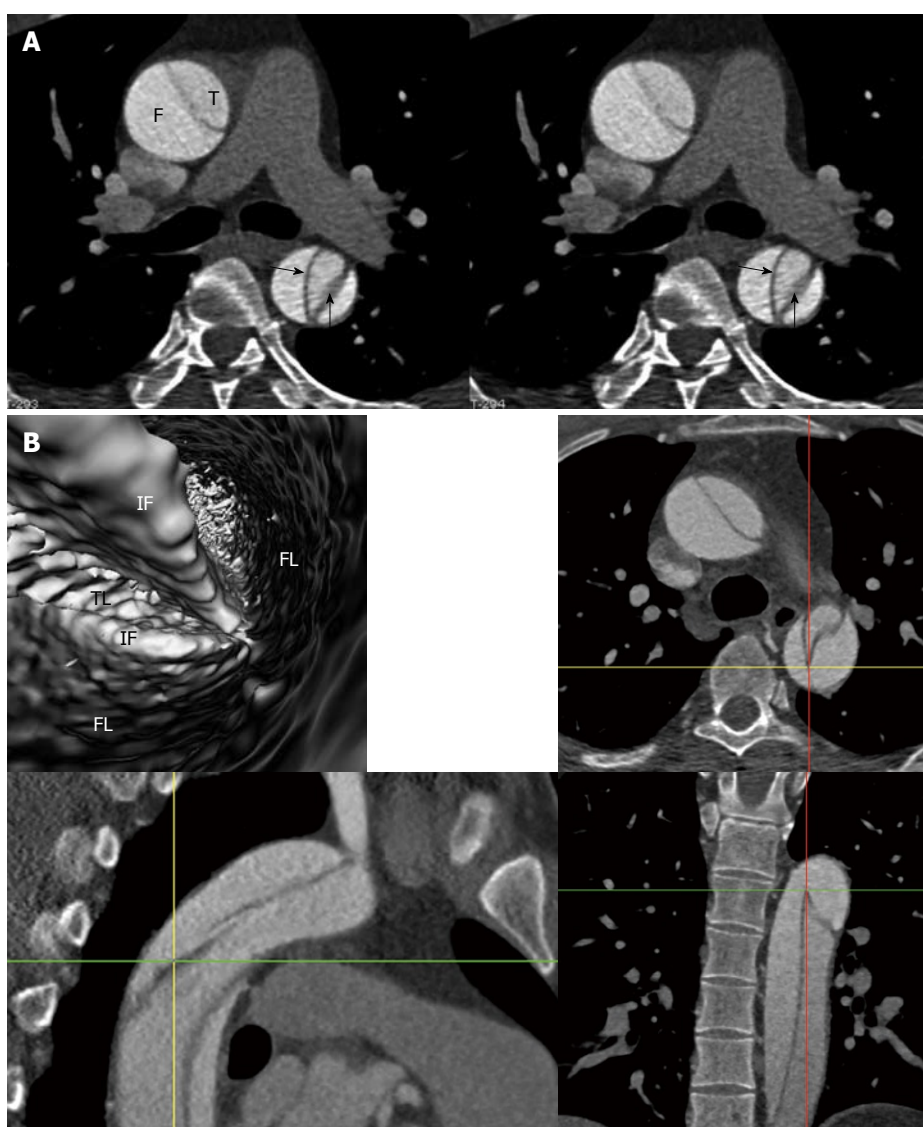


Figure 12 Stanford type A dissection with appearance of intimointimal intussusception (arrows in A). Corresponding virtual intravascular endoscopy shows the centrally narrowed true lumen (TL) was surrounded by the false lumen (FL) and separated by two intimal flaps (IF). The exact position of the VIE view is confirmed by the orthogonal views which are shown in B.

diac rupture, cardiac failure and end-organ ischemia. The aorta gives rise to many important branches that include

coronary arteries, carotid and vertebral arteries, subclavian arteries, lumbar arteries, celiac and mesenteric arteries, re-

nal arteries and iliac arteries. These branch arteries can become poorly perfused due to obstructions at their origin, as would happen if the artery branch was thrombosed during dissection^[15]. It is imperative to determine whether these major branch arteries originate from true or false lumens before interventional procedures such as placement of endovascular stent grafts or stents^[5,6,8], because any branch vessels supplied by the false lumen may be occluded with an intervention unless surgically bypassed. Medical imaging techniques play an important role in this aspect.

High resolution CT imaging is the method of choice for diagnosis of aortic dissection and identification of true and false lumens, as well as determination of the aortic branches in relation to the dissection^[2,10]. The most reliable direct imaging sign observed by CT for differentiating the true from false lumens is the ability to demonstrate direct continuity between the true lumen and the lumen of the uninvolved aortic lumen distal or proximal to the dissected aortic segment. This may not always be possible because the dissection may extend proximally into the aortic root, or the origin of the intimomedial entrance tear is at the convexity of the aortic arch where the true and false lumens may be difficult to follow^[7,9]. The limitation of 2D CT imaging is complemented by multiplanar reformation and 3D reconstructions. Our experience of using VIE for assessment of aortic dissection, especially in the identification of intimal tears shows the feasibility of VIE visualization in complex cases of dissection.

In addition to the identification of the entry site, determination of the extent of the entry site can be further explored by VIE and assessment of vessel involvement can be confirmed even if for visualization of the tiny artery branches such as coronary arteries, as shown in Figures 5 and 6. We believe VIE could be used as a complementary tool to conventional CT visualizations for accurate assessment of the aortic dissection.

VIE image quality is determined by an appropriate threshold selection. Demonstration of true and false lumens is dependent on CT attenuation measured in each compartment. The intimal flap has a soft tissue density and presents as a linear structure; thus, it is commonly shown as an irregular linear structure which separates the true lumen from the false lumen (Figure 10B). Detecting full-directional information about the dissection should be assisted with cross-sectional and multiplanar reformatted CT images. Correlation with orthogonal views is necessary to confirm the exact position of anatomic details on VIE visualization, especially to assess the aortic branches with regard to their relationship to the dissection.

With the current multislice CT scanners such as the 64-slice or dual source CT, acquisition of isotropic volume data is possible so that high resolution original data is generated to ensure the image quality of VIE images^[16,17]. In our small group of patients whose CT scans were performed with a dual source CT scanner, VIE was successfully generated in all of the patients with clear demonstration of anatomical details including the linear

structure of intimal flap. Rapidly technical developments have significantly enhanced the diagnostic value of CT in the detection and evaluation of aortic dissection.

In conclusion, in this pictorial essay, we demonstrated the applications of VIE for visualization of aortic dissection and identification of true and false lumens, intimal flap and intimal entry site. Our preliminary study shows that VIE is a feasible 3D visualization tool which could be used to assist radiologists to accurately evaluate aortic dissection so that better patient management could be achieved.

COMMENTS

Background

Aortic dissection is a common vascular disease which carries high mortality if not diagnosed and treated appropriately. Despite high diagnostic value of computed tomography (CT) angiography in the diagnosis of aortic dissection, its accuracy to identify the location of an intimal tear or entry site is limited in some complicated cases. This study presents the advantages of 3D virtual intravascular endoscopy (VIE) for identification of intimal tear and assessment of vessel involvement in aortic dissection.

Research frontiers

Extended application of 3D VIE to the patients with aortic dissection, thus, improving understanding of the dissection extent and vessel involvement for surgical planning.

Innovations and breakthroughs

Aortic dissection is routinely diagnosed and evaluated with CT angiography through a combination of 2D and 3D visualizations. This study presents advanced applications of VIE in aortic dissection by demonstrating findings which cannot be achieved with traditional image visualizations.

Applications

Our preliminary study shows the potential value of VIE in aortic dissection. Further studies based on a large cohort are needed to compare the diagnostic value of VIE with traditional 2D/3D visualizations.

Terminology

VIE is a method of image data visualization using computer processing of 3D image datasets (such as CT or MR scans). It can provide visualizations of vascular structures similar or equivalent to those produced by standard endoscopic procedures.

Peer review

It's a well written pictorial essay about 3D VIE in aortic dissection. There are many figures showing aortic dissection and their 3D VIE views.

REFERENCES

- 1 Castañer E, Andreu M, Gallardo X, Mata JM, Cabezu MA, Pallardó Y. CT in nontraumatic acute thoracic aortic disease: typical and atypical features and complications. *Radiographics* 2003; **23** Spec No: S93-S110
- 2 Sebastià C, Pallisa E, Quiroga S, Alvarez-Castells A, Dominguez R, Evangelista A. Aortic dissection: diagnosis and follow-up with helical CT. *Radiographics* 1999; **19**: 45-60; quiz 149-150
- 3 Cigarroa JE, Isselbacher EM, DeSanctis RW, Eagle KA. Diagnostic imaging in the evaluation of suspected aortic dissection. Old standards and new directions. *N Engl J Med* 1993; **328**: 35-43
- 4 Small JH, Dixon AK, Coulden RA, Flower CD, Housden BA. Fast CT for aortic dissection. *Br J Radiol* 1996; **69**: 900-905
- 5 LePage MA, Quint LE, Sonnad SS, Deeb GM, Williams DM. Aortic dissection: CT features that distinguish true lumen from false lumen. *AJR Am J Roentgenol* 2001; **177**: 207-211
- 6 Williams DM, Lee DY, Hamilton BH, Marx MV, Narasimham DL, Kazanjian SN, Prince MR, Andrews JC, Cho KJ, Deeb GM. The dissected aorta: percutaneous treatment of

- ischemic complications--principles and results. *J Vasc Interv Radiol* 1997; **8**: 605-625
- 7 **Kapoor V**, Ferris JV, Fuhrman CR. Intimomedial rupture: a new CT finding to distinguish true from false lumen in aortic dissection. *AJR Am J Roentgenol* 2004; **183**: 109-112
- 8 **Williams DM**, Joshi A, Dake MD, Deeb GM, Miller DC, Abrams GD. Aortic cobwebs: an anatomic marker identifying the false lumen in aortic dissection--imaging and pathologic correlation. *Radiology* 1994; **190**: 167-174
- 9 **Scaglione M**, Salvolini L, Casciani E, Giovagnoni A, Mazzei MA, Volterrani L. The many faces of aortic dissections: Beware of unusual presentations. *Eur J Radiol* 2008; **65**: 359-364
- 10 **Berger FH**, van Lienden KP, Smithuis R, Nicolaou S, van Delden OM. Acute aortic syndrome and blunt traumatic aortic injury: pictorial review of MDCT imaging. *Eur J Radiol* 2010; **74**: 24-39
- 11 **Sun Z**, Winder RJ, Kelly BE, Ellis PK, Hirst DG. CT virtual intravascular endoscopy of abdominal aortic aneurysms treated with suparenal endovascular stent grafting. *Abdom Imaging* 2003; **28**: 580-587
- 12 **Sun Z**, Winder RJ, Kelly BE, Ellis PK, Kennedy PT, Hirst DG. Diagnostic value of CT virtual intravascular endoscopy in aortic stent-grafting. *J Endovasc Ther* 2004; **11**: 13-25
- 13 **Sun Z**, Allen YB, Nadkarni S, Knight R, Hartley DE, Lawrence-Brown MM. CT virtual intravascular endoscopy in the visualization of fenestrated stent-grafts. *J Endovasc Ther* 2008; **15**: 42-51
- 14 **Louis N**, Desgranges P, Kobeiter H, Kirsch M, Becquemin JP. Virtual angiography and 3-dimensional navigation findings of the aortic arch after vascular surgery. *Circulation* 2009; **119**: 1052-1055
- 15 **Golledge J**, Eagle KA. Acute aortic dissection. *Lancet* 2008; **372**: 55-66
- 16 **Brodoefel H**, Burgstahler C, Tsiflikas I, Reimann A, Schroeder S, Claussen CD, Heuschmid M, Kopp AF. Dual-source CT: effect of heart rate, heart rate variability, and calcification on image quality and diagnostic accuracy. *Radiology* 2008; **247**: 346-355
- 17 **Leschka S**, Alkadhi H, Plass A, Desbiolles L, Grünenfelder J, Marincek B, Wildermuth S. Accuracy of MSCT coronary angiography with 64-slice technology: first experience. *Eur Heart J* 2005; **26**: 1482-1487

S- Editor Cheng JX L- Editor O'Neill M E- Editor Zheng XM

Perfusion characterization of liver metastases from endocrine tumors: Computed tomography perfusion

Aur lie Guyennon, Marius Mihaila, John Palma, Catherine Lombard-Bohas, Jean-Alain Chayvialle, Frank Pilleul

Aur lie Guyennon, Marius Mihaila, John Palma, Frank Pilleul, Department of Gastrointestinal Radiology, University Hospital Edouard Herriot, 5 Place d'Arsonval 69437 Lyon, France
 Catherine Lombard-Bohas, Department of Oncology, University Hospital Edouard Herriot, 5 Place d'Arsonval 69437 Lyon, France

Jean-Alain Chayvialle, Department of Hepato-Gastroenterology, University Hospital Edouard Herriot, 5 Place d'Arsonval 69437 Lyon, France

Author contributions: All authors had a nearly equivalent contribution to this paper.

Correspondence to: Frank Pilleul, Professor, Department of Gastrointestinal Radiology, University Hospital Edouard Herriot, 5 Place d'Arsonval 69437 Lyon, France. frank.pilleul@chu-lyon.fr

Telephone: +33-472-115473 Fax: +33-472-117541

Received: April 15, 2010 Revised: October 15, 2010

Accepted: October 22, 2010

Published online: November 28, 2010

a radiologist and regions of interest were plotted on the metastases, normal liver, aorta and portal vein.

RESULTS: At the arterial phase of the morphological CT scan, the aspects of liver metastases were hyperdense ($n = 21$), hypodense ($n = 7$), and necrotic ($n = 2$). In cases of necrotic metastases, none of the CT p parameters were changed. Compared to normal liver, a significant difference in all CT p parameters was found in cases of hyperdense metastases, and only for HAPI and MTT in cases of hypodense metastases. No significant difference was found for MTT and HAPI between hypo- and hyperdense metastases. A significant decrease of PS, BV and BF was demonstrated in cases of patients with hypodense lesions PS (23 ± 11.6 mL/100 g per minute) compared to patients with hyperdense lesions; PS (13.5 ± 10.4 mL/100 g per minute), BF (93.7 ± 75.4 vs 196.0 ± 115.6 mL/100 g per minute) and BV (9.7 ± 5.9 vs 24.5 ± 10.9 mL/100 g).

CONCLUSION: CT p provides additional information compared to the morphological appearance of liver metastases.

© 2010 Baishideng. All rights reserved.

Key words: Computed tomography perfusion scanning; Tumor angiogenesis; Hepatic metastases; Endocrine tumors

Peer reviewers: Xiao-Ming Zhang, MD, Professor, Department of Radiology, Affiliated Hospital of North Sichuan Medical College, Wenhua Road 63, Nanchong 637000, Sichuan Province, China; Kenneth Coenegrachts, MD, PhD, Department of Radiology, AZ St-Jan AV, Ruddershove 10, B-8000 Bruges, Belgium

Guyennon A, Mihaila M, Palma J, Lombard-Bohas C, Chayvialle JA, Pilleul F. Perfusion characterization of liver metastases from endocrine tumors: Computed tomography perfusion. *World J Radiol* 2010; 2(11): 449-454 Available from: URL: <http://www.wjgnet.com/1949-8470/full/v2/i11/449.htm> DOI: <http://dx.doi.org/10.4329/wjr.v2.i11.449>

Abstract

AIM: To assess prospectively parameters of computed tomography perfusion (CT p) for evaluation of vascularity of liver metastases from neuroendocrine tumors.

METHODS: This study was approved by the hospital's institutional review board. All 18 patients provided informed consent. There were 30 liver metastases from neuroendocrine tumors. Patients were divided into three groups depending on the appearance of the liver metastases at the arterial phase of morphological CT (hyperdense, hypodense and necrotic). Sequential acquisition of the liver was performed before and for 2 min after intravenous injection of 0.5 mg/kg contrast medium, at 4 mL/s. Data were analyzed using deconvolution analysis to calculate blood flow (BF), blood volume (BV), mean transit time (MTT), hepatic arterial perfusion index (HAPI) and a bi-compartmental analysis was performed to obtain vascular permeability-surface area product (PS). Post-treatment analysis was performed by

INTRODUCTION

Neuroendocrine tumors are rare^[1], and are usually described as having a slow rate of progression. The presence of hepatic metastases from neuroendocrine tumors is frequent (25%-90%) and has obvious implications for quality of life (in the presence of debilitating functional syndromes), which affects the overall prognosis^[2]. The 5-year survival rate depends on the presence of hepatic metastases and represents an independent prognostic factor, such as tumor cell differentiation and complete resection of the primary tumor^[3]. Accordingly, the presence of hepatic metastases influences the strategies available for treatment.

Neuroendocrine tumors are characterized by a dense and specialized capillary network^[4]. This specificity has been commonly used for diagnosis on conventional and multiphase helical computed tomography (CT) scanning with contrast enhancement. Currently, various patterns of enhancement have been described on contrast-enhanced CT scanning, which suggest that the angiogenesis process is variable among liver metastases of neuroendocrine tumors^[3]. CT perfusion (CT p) is a technology that allows quantitative assessment of various parameters, such as tumor blood flow (BF), blood volume (BV), mean transit time (MTT), and permeability-surface area product (PS). CT p is currently used for brain, lung, and head and neck tumors.

The purpose of our study was to describe, prospectively, parameters of CT p in evaluating the vascularity of tumors in different aspects of liver metastases from neuroendocrine tumors.

MATERIALS AND METHODS

Selection

This prospective single center study included patients with pathologically proven liver metastases from neuroendocrine tumors, during the period between February 2007 and January 2008 at the Department of Gastrointestinal Imaging of the University Hospital Edouard Herriot, and for whom liver CT scanning was performed. Patients without adequate renal function (creatinine clearance < 50 mL/min), allergy, liver metastases not detected by non-contrast enhancement CT, non-cooperative patients, and patients with dyspnea were excluded from the study.

Patient population/study cohort

The study cohort included 10 men and eight women (age range: 38-81 years; mean age: 55 years).

The site of the main tumor was either gastrointestinal ($n = 8$), pancreas ($n = 6$), kidney ($n = 2$), lung ($n = 1$) or indeterminate ($n = 1$). All patients had a well-differentiated neuroendocrine tumor; digestive tumors were all classified as group 2 according to WHO 2000 criteria (well-differentiated endocrine carcinoma)^[5], lung tumor as atypical carcinoid tumor, and other tumors as differentiated neuroendocrine tumors by a referent pathologist. Seventeen out of 18 patients benefited initially from surgical excision

of the primary tumor and were in the course of additional treatment. Our institutional review board approved the study, and all patients gave their informed consent.

The cohort was divided into three different groups depending on the aspect of liver metastases at the arterial phase of the CT scan in comparison with background liver parenchyma; two of the groups being patients with hypodense liver metastases ($n = 4$) and hyperdense liver metastases ($n = 12$). If the lesion has a cystic element, the third group classified patients as having necrotic liver metastases ($n = 2$).

CT p technique

CT p of the liver was obtained to estimate the following parameters in metastases of neuroendocrine tumors and the background liver: BF, BV, MTT, hepatic arterial perfusion index (HAPI), and capillary PS^[6,7]. CT p of the liver was performed with a 32-section multi-row CT scanner (Light Speed; GE Medical Systems, Milwaukee, WI, USA). A non-contrast CT scan of the liver was obtained to localize the tumor for further investigation by dynamic scanning. A 4-cm region of interest (ROI) was selected and dynamic scanning of this area was performed at a static table position 5 s after initiation of intravenous injection. The scanning was made at breath-holding after deep inspiration. A total of 0.5 mg/kg non-ionic iodinated contrast medium (Xenetix; 350 mg/mL iodine; Guerbet, France) was injected at a rate of 4 mL/s through an 18-gauge intravenous cannula. The following CT parameters were used to acquire dynamic data: 1-s gantry rotation time, 80 kVp, 100 mAs, acquisition with 8 sections per gantry rotation and 5-mm reconstructed section thickness. Scanning was initiated after a 5-s delay from the start of the injection, and images were acquired for a total duration of 120 s: 40 acquisitions with 1 rotation/s during 40 s, 10 acquisitions with 1 rotation/2 s during 20 s, and 12 acquisitions with 1 rotation/4 s during 60 s, to limit the radiation dose.

Data analysis

Data were processed at a workstation (Advantage Windows 4.0; GE Medical Systems) with CT p software (GE Perfusion 3.0) by an experienced radiologist in the field of abdominal imaging. This software is based on the mathematical models of Johnson and Wilson. Functional maps were obtained by displaying images at an appropriate window and filter, placing an ROI in the aorta and portal vein manually to provide reference arterial and portal vein curves. Functional maps of BF, BV, MTT, PS and HAPI were generated and were displayed in a range of colors. ROIs for tumors (range: 28-1333.3 mm²) and background liver parenchyma (range: 41-1118.5 mm²) were hand drawn.

Statistical analysis

The value of BF, BV, HAPI, PS and MTT for each ROI of liver metastases and background parenchyma were recorded. Data were compiled in an Excel 2003 database

to calculate the mean, SD and variance of each parameter. One-way ANOVA was used to compare the difference in CT p parameters between hepatic metastases from neuroendocrine tumors and the background liver. In addition, ANOVA was used to compare CT p parameters between the three subgroups. Statistical analysis using Student's *t* test was performed to calculate the *P* value for each comparison. $P \leq 0.05$ was considered to indicate a statistically significant difference.

RESULTS

CT p parameters of liver metastases of neuroendocrine tumors vs normal liver parenchyma

In the cohort of 18 patients, the CT scan aspect of liver metastases of neuroendocrine tumors in the arterial phase (scanning after 30 s from the injection of the contrast material) was hyperdense ($n = 21$), hypodense ($n = 7$), and necrotic ($n = 2$). The average size of liver metastases was 35 ± 23.5 mm (range: 11–89 mm). A CT p scan could not be performed on two patients due to technical problems (a delay starting the acquisition). These two patients were subsequently excluded from the study. Comparison of CT p parameters between hepatic metastases from neuroendocrine tumors and the background liver was performed.

Overall, liver metastases from neuroendocrine tumors demonstrated higher CT p parameters (BF, BV, PS) than the background liver (Table 1). There was a significant difference in perfusion parameters between liver metastases and the background liver ($P < 0.05$). In cases of necrotic metastases, none of the CT p parameters were changed.

MTT was equal to 11.4 s (SD: 3.6) for the metastases group and 15.2 s (SD: 3.3) for the parenchyma group ($P < 0.001$). There is an increased arterial perfusion in hepatic metastases of neuroendocrine tumors with HAPI equal to 0.66 ± 0.21 for metastases and 0.21 ± 0.17 for the background liver ($P < 0.001$).

Comparison of CT p parameters between patients with hyperdense and hypodense liver metastases in the arterial phase of the CT scan

Mean HAPI was similar in both hyperdense (0.67 ± 0.14) and hypodense (0.64 ± 0.35) liver metastases. The mean BF and BV parameters were lower in patients with hypodense liver metastases compared to those with hyperdense liver metastases (BF: 93.7 ± 75.4 mL/100 g per minute *vs* 196.0 ± 115.6 mL/100 g per minute; BV: 9.7 ± 5.9 mL/100 g *vs* 24.5 ± 10.9 mL/100 g). MTT was not significantly different when comparing hypodense and hyperdense liver metastases (11.7 ± 4.7 s *vs* 10.7 ± 2.9 s). Permeability was 13.5 ± 10.4 mL/100 g per minute (hypodense liver lesions) *vs* 23 ± 11.6 mL/100 g per minute (hyperdense liver metastases).

Necrotic liver metastases from neuroendocrine tumors

Two patients of our cohort presented with necrotic liver

Table 1 Computed tomography perfusion parameters of metastases from neuroendocrine tumors and background liver

CT p parameters	Liver metastases from neuroendocrine tumors	Background liver	<i>P</i> value
BF (mL/100 g per minute)	170.5 ± 114.9	80.6 ± 38.3	< 0.001
BV (mL/100 g)	20.8 ± 11.8	13.9 ± 6.7	< 0.01
PS (mL/100 g per minute)	20.9 ± 11.8	15.9 ± 6.6	< 0.05
MTT (s)	11.4 ± 3.6	15.2 ± 3.3	< 0.001
HAPI	0.66 ± 0.21	0.21 ± 0.17	< 0.001

CT p: Computed tomography perfusion; BF: Blood flow; BV: Blood volume; MTT: Mean transit time; HAPI: Hepatic arterial perfusion index; PS: Permeability-surface area product.

metastases from neuroendocrine tumors. Their curves of contrast enhancement had a null slope. On the parametric maps, HAPI was equal to 0.36 ± 0.03 , BF was 20.2 ± 0.2 mL/100 g per minute, BV was 2.2 ± 0.4 mL/100 g, MTT was 14.2 ± 1.4 s, and PS was 1.7 ± 1.1 mL/100 g per minute.

DISCUSSION

The results of our study were significant. Comparison between metastases and normal liver parenchyma demonstrated a significant increase in BV, BF and PS, and a lower MTT within the lesions ($P < 0.05$) compared to the normal liver.

Quantification of various parameters of vascularization of liver metastasis showed a significant increase in tumor perfusion compared to that of normal liver parenchyma. These results seem similar to those found previously^[8,9]. Sahani *et al*^[8] have analyzed the parameters of perfusion in cases of hepatocellular carcinoma (HCC) and have found significant differences between measures performed within the lesion compared with the non-tumoral liver parenchyma. Although HCC and liver metastatic lesions from neuroendocrine tumors are considered to be hypervascular on dynamic imaging, a difference in their CT p parameters seems apparent, which could help in the differential diagnosis of the hepatic lesions. Fabiano *et al*^[10] and Wang *et al*^[11] also have found differences between the values of the CT p parameters of benign and malignant liver lesions. Fournier *et al*^[12] have previously identified differences in CT p values between regenerative and dysplastic carcinomatous nodules, which allowed early detection of HCC. Tsushima *et al*^[13] have performed a comparative study to evaluate CT p of HCC and liver metastases of colorectal origin. All the lesions were hypervascular compared to normal liver parenchyma, but HCC presented with arterial perfusion that was superior to that of colorectal metastases (0.94 ± 0.26 mL/min per milliliter *vs* 0.67 ± 0.33 mL/min per milliliter, $P = 0.03$).

BV and BF of normal liver parenchyma in our study were different to those found in the study of Sahani *et al*^[8] (BF: 57 ± 38.3 mL/100 g per minute *vs* $14.9 \pm$

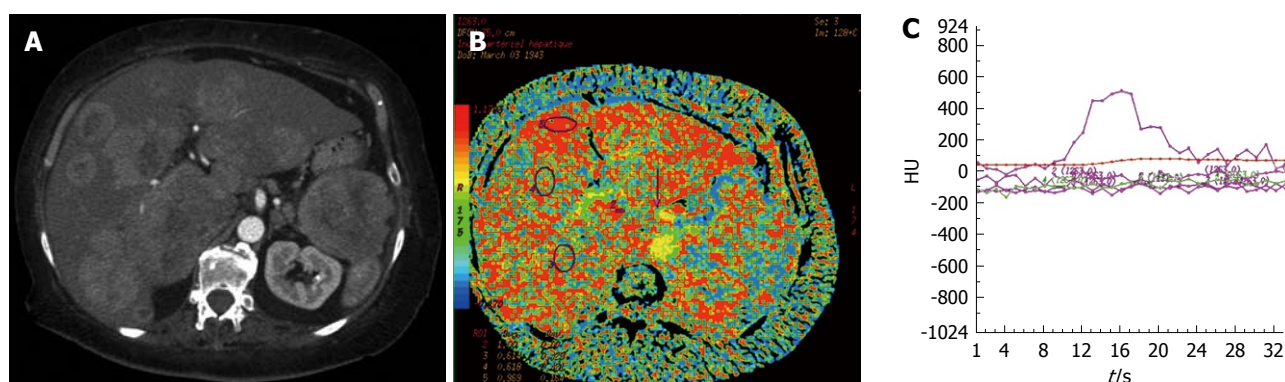


Figure 1 Functional maps of hepatic arterial perfusion index for a hyperdense metastasis from a neuroendocrine tumor (A-C).

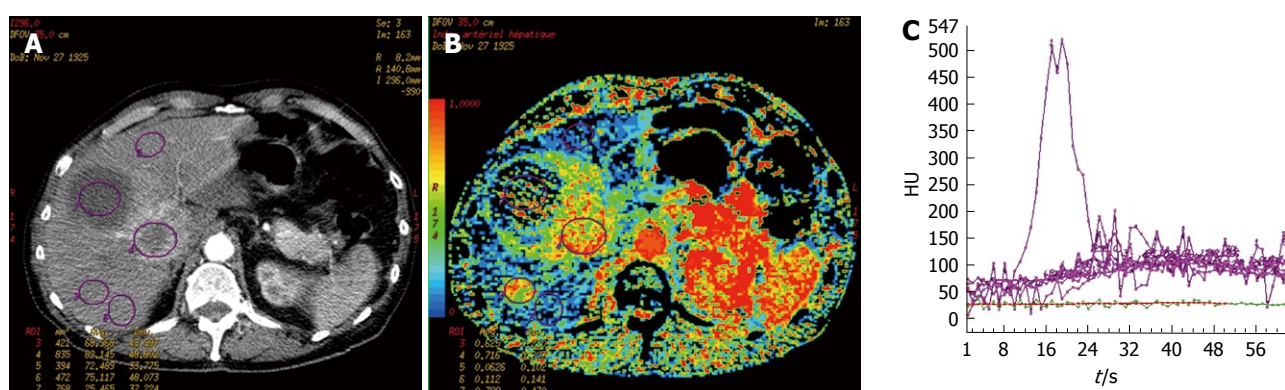


Figure 2 Example of results for a necrotic liver metastasis from an neuroendocrine tumor (A-C).

2.8 mL/100 g per minute; BV: 13.9 ± 6.8 mL/100 g *vs* 2.6 ± 0.9 mL/100 g). These differences were explained by the existence of underlying cirrhosis in patient with HCC. Fibrosis of the liver parenchyma involved an increased resistance vascular network, thus revealing a fall in BF and BV. Guan *et al*^[14] have identified in an animal study, modification of the CT p parameters in the liver between different stages of hepatitis, fibrosis and cirrhosis. Van Beers *et al*^[15] also have shown in a human study, decreased BF, and increased HAPI and MTT ($P < 0.05$) in cases of cirrhosis compared to a normal population with a strong correlation between these modifications and the severity of cirrhosis (Child-Pugh class A, B and C). The increased HAPI should be explained by the development of secondary hyper-arteriolization and the presence of portal hypertension. In our patients with liver metastases from neuroendocrine tumors, five presented with hypodense lesions (31.25%) and 11 with hyperdense lesions (68.75%), which was similar to other findings in the literature^[3]. Comparison of metastatic disease according to its hypodense or hyperdense aspect demonstrated decreased tumor perfusion for the hypodense lesion (BF: $P < 0.05$; BV: $P < 0.01$). A correlation between the hypo- or hyperdense aspect of neuroendocrine liver metastases, their microvascular index of density, and their degree of tumor differentiation has already been demonstrated^[3]. Therefore, the CT p parameters of tumor vascularization could represent a prognostic factor and should be con-

firmed by the realization of a prospective study that correlates CT p and histological data with a survival curve. Values of HAPI, which have not been systematically calculated in published studies, could be altered by the presence of portal hypertension or portal vein thrombosis. In our study, the HAPI of the normal parenchyma measured 0.21 on average, which corresponds to the arterial part of hepatic vascularization^[16]. Neuroendocrine liver metastases mainly develop with an arterial network (HAPI: 0.66)^[17-19]. Thus, our study showed that all neuroendocrine liver metastases were hypervascular and arterial (Figure 1). Furthermore, HAPI seemed to be similar for hypodense and hyperdense liver lesions (0.67 and 0.64). Therefore, hypodense liver metastases from neuroendocrine tumors also have preferential arterial vascularization identical to that of hyperdense metastases.

Even if neuroendocrine liver metastases are hypodense by double-phase CT scanning, these lesions have the same type of arterial network but have lower CT p parameters; probably because of architectural differences from the network of neo-microvascularization due to different neoangiogenesis.

In cases of neuroendocrine metastases with necrosis, perfusion parameters could not be measured, due to the lack of vascularization in the necrotic area (Figure 2). Nevertheless, CT p has some limitations. The volume of exploration is limited by the width of the detectors, which is generally 4 cm. The selection of the metastatic

area and the portal vein section for comparison are operator dependent, thus, this technical constraint could limit lesion detection.

Standardization of CT p values allowed minimization of variations due to cardiac output and circulating BV. This standardization is not available at present for commercial software. It was recently proposed by Miles *et al*^[20] and the principle is similar to that used for positron emission tomography, with the standardized perfusion value (SPV), such that $SPV = \text{tissue perfusion} / \text{total body perfusion}$. This requires knowledge of the dose of contrast agent injected and the body weight of the patient. Recently, Goh *et al*^[21] have compared the CT p parameters of colorectal tumors in 44 examinations performed with two different commercial software packages, and have identified a lack of reproducibility for the different values. Commercially available softwares do not use the same mathematical models for calculation, and are not thus interchangeable. However, it does seem possible to apply a factor of correction according to the software used.

Therefore, CT p seems to be promising for exploring diffuse hepatic disease such as fibrosis and cirrhosis^[14,15]. Furthermore, CT p seems to be attractive for the diagnosis and follow-up of focal liver lesions. CT p has demonstrated increased arterial flow within macro-metastases in numerous studies^[22].

In 2001, a small animal study demonstrated that the presence of micro-metastases of the liver decreased the portal flow by up to 34%, and increased MTT up to 25%, which was explained by increased resistance in the sinusoids^[23].

In 2005, Kan *et al*^[7] performed a small animal study that demonstrated significant modification of BV, BF and PS of intrahepatic lesions at days 1 and 14 of daily antiangiogenic treatment, but without correlation with the microvascular index of density. One of the hypotheses could be modification of the number of circulating microvessels with the appearance of non-functional vessels and not the total number of microvessels. In 2006, Meijerink *et al*^[24] measured the BF of primary lesions (melanoma, fibrosarcoma, mesothelioma, osteosarcoma, colorectal carcinoma) and of hepatic, pleural, mediastinal and pelvic secondary tumors before and after treatment, by association of a vascular endothelial growth factor receptor inhibitor and an epidermal growth factor receptor inhibitor in a phase I clinical trial. The arterial BF was decreased in 12 out of 13 patients. CT p should be one of the tools that are indispensable for evaluation of antiangiogenic treatment, as well early detection of patients who respond well to such treatment.

However, the approach of using CT p imaging of liver metastases from neuroendocrine tumors highlighted some disadvantages. First of all, we did not estimate the reproducibility of the technique, which has already been demonstrated in the literature^[6-8]. Second, we did not study the reproducibility of the intra- and inter-operator values because a single radiologist did the post-treatment analysis of the CT p. Strong agreement of the intra- and

inter-observer values has already been demonstrated for the quantification of CT p in colorectal tumors^[9]. Finally, only a relatively small number of patients were included in our study because of limited time of inclusion and the low incidence of this pathology.

Furthermore, our study demonstrated the arterial predominance of the neo-microcirculation of the neuroendocrine liver metastases, and the advantage of chemoembolization could be extended to all the hyper- and hypodense lesions. Recent studies have demonstrated the advantages of CT p for detection of rectal tumors in patients who respond well to chemotherapy and radiotherapy, by comparing BF and MTT ($P < 0.05$). CT p could be used in the evaluation of antiangiogenic treatment of liver metastases^[25,26].

Neuroendocrine tumors constitute a homogeneous group of tumors that are disseminated within the body, which are characterized by their histological and biological properties. Liver metastases of neuroendocrine tumors are frequent, which is one of the main factors for poor prognosis. CT p is useful for characterization of liver metastases of neuroendocrine tumors, especially those that are hypervascular.

As in any neoplastic lesions, neoangiogenesis plays an essential role in tumor growth and the response to various therapeutic options. Quantification of tumor angiogenesis without an invasive procedure is essential in oncology for the characterization and staging of the lesions^[27].

CT p is a feasible technique for quantification of tumor vascularity and angiogenesis in liver metastases of neuroendocrine tumors. CT p could help in the future to identify subgroups of patients who could benefit from antiangiogenic therapy and help clinicians to choose the most appropriate treatment. Another challenge is to establish the accuracy of CT p to evaluate prospectively therapeutic efficacy.

COMMENTS

Background

Neuroendocrine tumors are characterized by their histological and biological properties. Liver metastases of neuroendocrine tumors are frequent, and are one of the main factors for poor prognosis. Computed tomography perfusion (CT p) is useful for characterization of liver metastases of neuroendocrine tumors, especially those that are hypervascular, which constitute a homogeneous group of tumors that are disseminated throughout the body.

Innovations and breakthroughs

CT p could help in the future to identify subgroups of patients who could benefit from antiangiogenic therapies and help clinicians to choose the most appropriate treatment to administer. Another challenge is to evaluate the accuracy of CT p to evaluate prospectively treatment efficiency.

Applications

As with any neoplastic lesions, neoangiogenesis plays an essential role in tumor growth and in the response to various therapeutic options. Quantification of tumoral angiogenesis without an invasive procedure is essential in oncology for the characterization and staging of the lesions. CT p is a feasible technique for quantification of tumor vascularity and angiogenesis in liver metastases of neuroendocrine tumors.

Terminology

Neuroendocrine tumors are rare and slow growing. They are characterized by a dense and specialized capillary network. The presence of hepatic metastases

from neuroendocrine tumors is frequent (25%-90%). CT p is a technique that allows quantitative assessment of various parameters, such as tumor blood flow, blood volume, mean transit time, and permeability-surface area product.

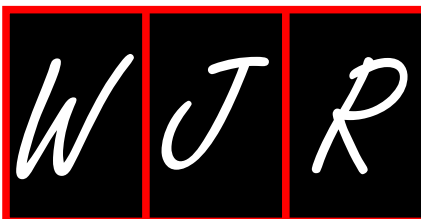
Peer review

This manuscript may be helpful to recognize the tumour vascularity of liver metastases from endocrine tumor and would be a reference for radiological practice.

REFERENCES

- Ruszniewski P, O'Toole D. Ablative therapies for liver metastases of gastroenteropancreatic endocrine tumors. *Neuroendocrinology* 2004; **80** Suppl 1: 74-78
- Dromain C, de Baere T, Baudin E, Galline J, Ducreux M, Boige V, Duvillard P, Laplanche A, Caillet H, Lasser P, Schlumberger M, Sigal R. MR imaging of hepatic metastases caused by neuroendocrine tumors: comparing four techniques. *AJR Am J Roentgenol* 2003; **180**: 121-128
- Rodallec M, Vilgrain V, Couvelard A, Rufat P, O'Toole D, Barrau V, Sauvanet A, Ruszniewski P, Menu Y. Endocrine pancreatic tumours and helical CT: contrast enhancement is correlated with microvascular density, histoprosthetic factors and survival. *Pancreatology* 2006; **6**: 77-85
- Scarsbrook AF, Ganeshan A, Statham J, Thakker RV, Weaver A, Talbot D, Boardman P, Bradley KM, Gleeson FV, Phillips RR. Anatomic and functional imaging of metastatic carcinoid tumors. *Radiographics* 2007; **27**: 455-477
- Solcia E, Klöppel G, Sobin L. In: WHO international histological classification of tumours: histological typing of endocrine tumours. 2nd ed. Berlin: Springer, 2000
- Miles KA, Griffiths MR. Perfusion CT: a worthwhile enhancement? *Br J Radiol* 2003; **76**: 220-231
- Kan Z, Phongkitkarun S, Kobayashi S, Tang Y, Ellis LM, Lee TY, Charnsangavej C. Functional CT for quantifying tumor perfusion in antiangiogenic therapy in a rat model. *Radiology* 2005; **237**: 151-158
- Sahani DV, Holalkere NS, Mueller PR, Zhu AX. Advanced hepatocellular carcinoma: CT perfusion of liver and tumor tissue—initial experience. *Radiology* 2007; **243**: 736-743
- Goh V, Halligan S, Hugill JA, Bassett P, Bartram CI. Quantitative assessment of colorectal cancer perfusion using MDCT: inter- and intraobserver agreement. *AJR Am J Roentgenol* 2005; **185**: 225-231
- Fabiano S, Squillaci E, Cariani M, Fusco N, Stefanini M, Simonetti G. CT Perfusion Studies of Liver Lesions with a 64-detector Row Scanner: Initial Clinical Results. *RSNA* 2005; **SSQ08-07**: 508
- Wang S, Zhou C, Zhao X. Perfusion studies of hepatic tumors: use of multi-detector row helical CT and liver perfusion software. In: Radiological Society of North America scientific assembly and annual meeting program 2004. Oak Brook: Radiological Society of North America, 2004: 238
- Fournier LS, Cuenod CA, de Bazelaire C, Siauve N, Rosty C, Tran PL, Fria G, Clement O. Early modifications of hepatic perfusion measured by functional CT in a rat model of hepatocellular carcinoma using a blood pool contrast agent. *Eur Radiol* 2004; **14**: 2125-2133
- Tsushima Y, Funabasama S, Aoki J, Sanada S, Endo K. Quantitative perfusion map of malignant liver tumors, created from dynamic computed tomography data. *Acad Radiol* 2004; **11**: 215-223
- Guan S, Zhao WD, Zhou KR, Peng WJ, Mao J, Tang F. CT perfusion at early stage of hepatic diffuse disease. *World J Gastroenterol* 2005; **11**: 3465-3467
- Van Beers BE, Leconte I, Materne R, Smith AM, Jamart J, Horsmans Y. Hepatic perfusion parameters in chronic liver disease: dynamic CT measurements correlated with disease severity. *AJR Am J Roentgenol* 2001; **176**: 667-673
- Bézy-Wendling J, Kretowski M, Rolland Y. Hepatic tumor enhancement in computed tomography: combined models of liver perfusion and dynamic imaging. *Comput Biol Med* 2003; **33**: 77-89
- Miles KA, Leggett DA, Kelley BB, Hayball MP, Sinnatamby R, Bunce I. In vivo assessment of neovascularization of liver metastases using perfusion CT. *Br J Radiol* 1998; **71**: 276-281
- Miles KA. Tumour angiogenesis and its relation to contrast enhancement on computed tomography: a review. *Eur J Radiol* 1999; **30**: 198-205
- Dugdale PE, Miles KA. Hepatic metastases: the value of quantitative assessment of contrast enhancement on computed tomography. *Eur J Radiol* 1999; **30**: 206-213
- Miles KA, Griffiths MR, Fuentes MA. Standardized perfusion value: universal CT contrast enhancement scale that correlates with FDG PET in lung nodules. *Radiology* 2001; **220**: 548-553
- Goh V, Halligan S, Bartram CI. Quantitative tumor perfusion assessment with multidetector CT: are measurements from two commercial software packages interchangeable? *Radiology* 2007; **242**: 777-782
- Pandharipande PV, Krinsky GA, Rusinek H, Lee VS. Perfusion imaging of the liver: current challenges and future goals. *Radiology* 2005; **234**: 661-673
- Cuenod C, Leconte I, Siauve N, Resten A, Dromain C, Poulet B, Frouin F, Clément O, Fria G. Early changes in liver perfusion caused by occult metastases in rats: detection with quantitative CT. *Radiology* 2001; **218**: 556-561
- Meijerink MR, van Crujisen H, Hoekman K, Kater M, van Schaik C, van Waesberghe JH, Giaccone G, Manoliu RA. The use of perfusion CT for the evaluation of therapy combining AZD2171 with gefitinib in cancer patients. *Eur Radiol* 2007; **17**: 1700-1713
- Sahani DV, Kalva SP, Hamberg LM, Hahn PF, Willett CG, Saini S, Mueller PR, Lee TY. Assessing tumor perfusion and treatment response in rectal cancer with multisection CT: initial observations. *Radiology* 2005; **234**: 785-792
- Bellomi M, Petralia G, Sonzogni A, Zampino MG, Rocca A. CT perfusion for the monitoring of neoadjuvant chemotherapy and radiation therapy in rectal carcinoma: initial experience. *Radiology* 2007; **244**: 486-493
- Pauls S, Gabelmann A, Heinz W, Fröhlich E, Juchems MS, Brambs HJ, Schmidt SA. Liver perfusion with dynamic multidetector-row computed tomography as an objective method to evaluate the efficacy of chemotherapy in patients with colorectal cancer. *Clin Imaging* 2009; **33**: 289-294

S- Editor Cheng JX L- Editor Kerr C E- Editor Zheng XM



ACKNOWLEDGMENTS

Acknowledgments to reviewers of World Journal of Radiology

Many reviewers have contributed their expertise and time to the peer review, a critical process to ensure the quality of *World Journal of Radiology*. The editors and authors of the articles submitted to the journal are grateful to the following reviewers for evaluating the articles (including those published in this issue and those rejected for this issue) during the last editing time period.

Filippo Cademartiri, MD, PhD, Department of Radiology - c/o Piastra Tecnica - Piano 0, Azienda Ospedaliero-Universitaria di Parma, Via Gramsci, 14 - 43100 Parma, Italy

Kenneth Coenegrachts, MD, PhD, Department of Radiology, AZ St.-Jan AV, Ruddershove 10, B-8000 Bruges, Belgium

Thomas Deserno, PhD, Professor, Department of Medical Informatics, RWTH Aachen University, Pauwelsstr, 30, 52057 Aachen, Germany

Mohamed Abou El-Ghar, MD, Department of Radiology, Urology and Nephrology center-Mansoura University, 72 El-gomhoria st, Mansoura, 35516, Egypt

Peter Gaines, Professor, Sheffield Vascular Institute, Northern General Hospital, Sheffield, S5 7AU, United Kingdom

Igor Meglinski, PhD, Head of Bio-Photonics and Bio-Medical Imaging, Cranfield Health, Cranfield University, Cranfield, Bedfordshire, MK43 0AL, United Kingdom

Yicheng Ni, MD, PhD, Professor, Biomedical Imaging, Interventional Therapy and Contrast Media Research, Department of Radiology, University Hospitals, K.U. Leuven, Herestraat 49, B-3000, Leuven, Belgium

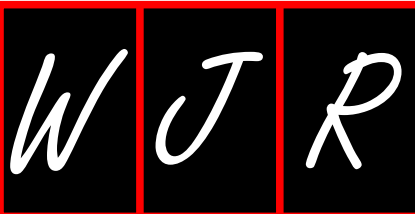
Sergio Sartori, MD, Department of Internal Medicine, Section of Interventional Ultrasound, St. Anna Hospital, I-44100 Ferrara, Italy

Ahmed A Shokeir, MD, PhD, FEBU, Professor, Urology Department, Urology and Nephrology Center, Mansoura University, Mansoura 35516, Egypt

Ender Uysal, MD, Sisli Etfal Training and Research Hospital, Clinic of Radiology, Sisli Etfal Eğitim ve Araştırma Hastanesi Radyoloji Kliniği, Etfal sok. Sisli, Istanbul 34377, Turkey

Martin A Walter, MD, Institute of Nuclear Medicine, University Hospital, Petersgraben 41, CH-4031 Basel, Switzerland

Xiao-Ming Zhang, MD, Professor, Department of Radiology, Affiliated Hospital of North Sichuan Medical College, Wenhua Road 63, Nanchong 637000, Sichuan Province, China



Meetings

Events Calendar 2010

January 4-8
Beaver Creek, Colorado, United States
18th Annual Winter Diagnostic Imaging Update

January 7-9
Leuven, Belgium
4th Leuven Course on Ear Imaging

January 16-17
Hollywood, Florida, United States
The Symposium on Clinical Interventional Oncology

January 17-21
Hollywood, Florida, United States
The International Symposium on Endovascular Therapy

January 21-22
Cairo, Egypt
BGICC Breast Gyne International Cancer Conference

January 21-24
Phoenix, AZ, United States
13th Society for Cardiovascular Magnetic Resonance (SCMR) Annual Scientific Sessions

January 23-23
Atlanta, GA, United States
Emory Winship Cancer Institute: Breast Cancer 2010: Advances in Science, Emerging Data, and Novel Therapeutics

January 25-29
Maui, HI, United States
Musculoskeletal & Neuroradiology MR Imaging Update in Maui

January 27-February 2
Albuquerque, NM, United States
2010 SNM Conjoint Mid-Winter Meetings

January 29-30
Barcelona, Spain
7th European Congress: Perspectives in Gynecologic Oncology

February 7-12
Vail, CO, United States
15th Annual Vail 2010: Multislice CT in Clinical Practice

February 11-13
Las Vegas, NV, United States
5th Annual Symposium on PET/CT and Molecular Imaging

February 16-19
Park City, UT, United States
6th Interventional/Neurointerventional Conference

February 18-19
London, United Kingdom
Diagnostic and Interventional Radiology

February 18-21
Las Vegas, NV, United States
American Society of Spine Radiology Annual Symposium

February 20-20
Jacksonville, Florida, United States
Mayo Clinic Molecular Markers and Management of Breast Cancer

February 20-21
Bethesda, Maryland, United States
25th Anniversary Washington Neuroradiology Review

February 21-26
Orlando, FL, United States
The Abdominal Radiology Course

February 21-27
Snowmass, CO, United States
16th Annual Snowmass 2010: Clinical Ultrasound

February 22-26
Bethesda, MD, United States
48th Annual Dr. Kenneth M. Earle Memorial Neuropathology Review

February 24-27
Lake Buena Vista, FL, United States
ACRO 2010 American College of Radiation Oncology Symposium: Clinical Radiation Oncology Challenges

February 25-27
Chandler, AZ, United States
Multidisciplinary Head and Neck Cancer Symposium

February 26-27
Brussels, Belgium
10èmes Mises au Point en Imagerie Ostéo-Articulaire

February 27-March 1
Cairo, Egypt
7th Gastroenterology Hepatology & Endoscopy Symposium

February 28-March 4
Scottsdale, AZ, United States
International Congress XXIII on Endovascular Interventions

February 28-March 5
Breckenridge, CO, United States
5th Annual Breckenridge 2010: Musculoskeletal MRI

March 3-6
Las Vegas, Nevada, United States
11th Annual Advances in Breast Imaging and Interventions

March 4-8
Vienna, Austria
European Congress of Radiology (ECR 2010) Annual Meeting

March 5-7
Mt Tremblant, QC, Canada
Neuroimaging and Head & Neck Radiology Update in Mt Tremblant

March 7-11
San Diego, CA, United States
SCBT-MR Masters in Body Imaging: "What's New, What's Hot, What You May Not Have Known"

March 10-13
San Antonio, Texas, United States
Clinical Osteoporosis 2010: An ISCD-NOF Symposium

March 11-13
Barcelona, Spain
EORTC Group Meeting: EORTC Radiation Oncology Group

March 11-13
Hannover, Germany
40. Kongress der Deutschen Gesellschaft für Endoskopie und Bildgebende Verfahren e.V.

March 13-18
Tampa, FL, United States
Society of interventional radiology 35th Annual Scientific Meeting

March 14-17
Park City, UT, United States
14th Annual Park City 2010: MRI in Clinical Practice

March 22-26
Beaver Creek, CO, United States
NYU Radiology Spring Skiing Symposium in Beaver Creek

March 22-26
Maui, HI, United States
18th Annual Spring Diagnostic Imaging Update

March 24-27
San Diego, California, United States
2010 American institute of ultrasound in Medicine Annual Convention Preliminary Program

March 24-27
Barcelona, Spain
7th European Breast Cancer Conference

April 8-12
Shanghai, China
The 26th International Congress of Radiology

September 8-12
Guangzhou, China
Chinese Society of Interventional Radiology, 2010 CSIR

November 28-December 03
Chicago, United States
Radiological Society of North America: 2010 Annual Meeting

Instructions to authors

GENERAL INFORMATION

World Journal of Radiology (*World J Radiol*, *WJR*, online ISSN 1949-8470, DOI: 10.4329), is a monthly, open-access (OA), peer-reviewed journal supported by an editorial board of 319 experts in Radiology from 40 countries.

The biggest advantage of the OA model is that it provides free, full-text articles in PDF and other formats for experts and the public without registration, which eliminates the obstacle that traditional journals possess and usually delays the speed of the propagation and communication of scientific research results. The open access model has been proven to be a true approach that may achieve the ultimate goal of the journals, i.e. the maximization of the value to the readers, authors and society.

Maximization of personal benefits

The role of academic journals is to exhibit the scientific levels of a country, a university, a center, a department, and even a scientist, and build an important bridge for communication between scientists and the public. As we all know, the significance of the publication of scientific articles lies not only in disseminating and communicating innovative scientific achievements and academic views, as well as promoting the application of scientific achievements, but also in formally recognizing the "priority" and "copyright" of innovative achievements published, as well as evaluating research performance and academic levels. So, to realize these desired attributes of *WJR* and create a well-recognized journal, the following four types of personal benefits should be maximized. The maximization of personal benefits refers to the pursuit of the maximum personal benefits in a well-considered optimal manner without violation of the laws, ethical rules and the benefits of others. (1) Maximization of the benefits of editorial board members: The primary task of editorial board members is to give a peer review of an unpublished scientific article via online office system to evaluate its innovativeness, scientific and practical values and determine whether it should be published or not. During peer review, editorial board members can also obtain cutting-edge information in that field at first hand. As leaders in their field, they have priority to be invited to write articles and publish commentary articles. We will put peer reviewers' names and affiliations along with the article they reviewed in the journal to acknowledge their contribution; (2) Maximization of the benefits of authors: Since *WJR* is an open-access journal, readers around the world can immediately download and read, free of charge, high-quality, peer-reviewed articles from *WJR* official website, thereby realizing the goals and significance of the communication between authors and peers as well as public reading; (3) Maximization of the benefits of readers: Readers can read or use, free of charge, high-quality peer-reviewed articles without any limits, and cite the arguments, viewpoints, concepts, theories, methods, results, conclusion or facts and data of pertinent literature so as to validate the innovativeness, scientific and practical values of their own research achievements, thus ensuring that their articles have novel arguments or viewpoints, solid evidence and correct conclusion; and (4) Maximization of the benefits of employees: It is an iron law that a first-class journal is unable to exist without first-class editors, and only first-class editors can create a first-class academic journal. We insist on strengthening our team cultivation and construction so that every employee, in an open, fair and transparent environment, could contribute their wisdom to edit and publish high-quality articles, thereby realizing the maximization of the personal benefits

of editorial board members, authors and readers, and yielding the greatest social and economic benefits.

Aims and scope

The major task of *WJR* is to rapidly report the most recent improvement in the research of medical imaging and radiation therapy by the radiologists. *WJR* accepts papers on the following aspects related to radiology: Abdominal radiology, women health radiology, cardiovascular radiology, chest radiology, genitourinary radiology, neuroradiology, head and neck radiology, interventional radiology, musculoskeletal radiology, molecular imaging, pediatric radiology, experimental radiology, radiological technology, nuclear medicine, PACS and radiology informatics, and ultrasound. We also encourage papers that cover all other areas of radiology as well as basic research.

Columns

The columns in the issues of *WJR* will include: (1) Editorial: To introduce and comment on major advances and developments in the field; (2) Frontier: To review representative achievements, comment on the state of current research, and propose directions for future research; (3) Topic Highlight: This column consists of three formats, including (A) 10 invited review articles on a hot topic, (B) a commentary on common issues of this hot topic, and (C) a commentary on the 10 individual articles; (4) Observation: To update the development of old and new questions, highlight unsolved problems, and provide strategies on how to solve the questions; (5) Guidelines for Basic Research: To provide guidelines for basic research; (6) Guidelines for Clinical Practice: To provide guidelines for clinical diagnosis and treatment; (7) Review: To review systemically progress and unresolved problems in the field, comment on the state of current research, and make suggestions for future work; (8) Original Articles: To report innovative and original findings in radiology; (9) Brief Articles: To briefly report the novel and innovative findings in radiology; (10) Case Report: To report a rare or typical case; (11) Letters to the Editor: To discuss and make reply to the contributions published in *WJR*, or to introduce and comment on a controversial issue of general interest; (12) Book Reviews: To introduce and comment on quality monographs of radiology; and (13) Guidelines: To introduce consensus and guidelines reached by international and national academic authorities worldwide on the research in radiology.

Name of journal

World Journal of Radiology

CSSN

ISSN 1949-8470 (online)

Indexed and Abstracted in

PubMed Central

Published by

Baishideng Publishing Group Co., Limited

SPECIAL STATEMENT

All articles published in this journal represent the viewpoints of the authors except where indicated otherwise.

Biostatistical editing

Statistical review is performed after peer review. We invite an expert in Biomedical Statistics from to evaluate the statistical method used in the paper, including *t*-test (group or paired comparisons), chi-

Instructions to authors

squared test, Ridit, probit, logit, regression (linear, curvilinear, or stepwise), correlation, analysis of variance, analysis of covariance, *etc.* The reviewing points include: (1) Statistical methods should be described when they are used to verify the results; (2) Whether the statistical techniques are suitable or correct; (3) Only homogeneous data can be averaged. Standard deviations are preferred to standard errors. Give the number of observations and subjects (*n*). Losses in observations, such as drop-outs from the study should be reported; (4) Values such as ED50, LD50, IC50 should have their 95% confidence limits calculated and compared by weighted probit analysis (Bliss and Finney); and (5) The word 'significantly' should be replaced by its synonyms (if it indicates extent) or the *P* value (if it indicates statistical significance).

Conflict-of-interest statement

In the interests of transparency and to help reviewers assess any potential bias, *WJR* requires authors of all papers to declare any competing commercial, personal, political, intellectual, or religious interests in relation to the submitted work. Referees are also asked to indicate any potential conflict they might have reviewing a particular paper. Before submitting, authors are suggested to read "Uniform Requirements for Manuscripts Submitted to Biomedical Journals: Ethical Considerations in the Conduct and Reporting of Research: Conflicts of Interest" from International Committee of Medical Journal Editors (ICMJE), which is available at: http://www.icmje.org/ethical_4conflicts.html.

Sample wording: [Name of individual] has received fees for serving as a speaker, a consultant and an advisory board member for [names of organizations], and has received research funding from [names of organization]. [Name of individual] is an employee of [name of organization]. [Name of individual] owns stocks and shares in [name of organization]. [Name of individual] owns patent [patent identification and brief description].

Statement of informed consent

Manuscripts should contain a statement to the effect that all human studies have been reviewed by the appropriate ethics committee or it should be stated clearly in the text that all persons gave their informed consent prior to their inclusion in the study. Details that might disclose the identity of the subjects under study should be omitted. Authors should also draw attention to the Code of Ethics of the World Medical Association (Declaration of Helsinki, 1964, as revised in 2004).

Statement of human and animal rights

When reporting the results from experiments, authors should follow the highest standards and the trial should conform to Good Clinical Practice (for example, US Food and Drug Administration Good Clinical Practice in FDA-Regulated Clinical Trials; UK Medicines Research Council Guidelines for Good Clinical Practice in Clinical Trials) and/or the World Medical Association Declaration of Helsinki. Generally, we suggest authors follow the lead investigator's national standard. If doubt exists whether the research was conducted in accordance with the above standards, the authors must explain the rationale for their approach and demonstrate that the institutional review body explicitly approved the doubtful aspects of the study.

Before submitting, authors should make their study approved by the relevant research ethics committee or institutional review board. If human participants were involved, manuscripts must be accompanied by a statement that the experiments were undertaken with the understanding and appropriate informed consent of each. Any personal item or information will not be published without explicit consents from the involved patients. If experimental animals were used, the materials and methods (experimental procedures) section must clearly indicate that appropriate measures were taken to minimize pain or discomfort, and details of animal care should be provided.

SUBMISSION OF MANUSCRIPTS

Manuscripts should be typed in 1.5 line spacing and 12 pt. Book

Antiqua with ample margins. Number all pages consecutively, and start each of the following sections on a new page: Title Page, Abstract, Introduction, Materials and Methods, Results, Discussion, Acknowledgements, References, Tables, Figures, and Figure Legends. Neither the editors nor the publisher are responsible for the opinions expressed by contributors. Manuscripts formally accepted for publication become the permanent property of Baishideng Publishing Group Co., Limited, and may not be reproduced by any means, in whole or in part, without the written permission of both the authors and the publisher. We reserve the right to copy-edit and put onto our website accepted manuscripts. Authors should follow the relevant guidelines for the care and use of laboratory animals of their institution or national animal welfare committee. For the sake of transparency in regard to the performance and reporting of clinical trials, we endorse the policy of the ICMJE to refuse to publish papers on clinical trial results if the trial was not recorded in a publicly-accessible registry at its outset. The only register now available, to our knowledge, is <http://www.clinicaltrials.gov> sponsored by the United States National Library of Medicine and we encourage all potential contributors to register with it. However, in the case that other registers become available you will be duly notified. A letter of recommendation from each author's organization should be provided with the contributed article to ensure the privacy and secrecy of research is protected.

Authors should retain one copy of the text, tables, photographs and illustrations because rejected manuscripts will not be returned to the author(s) and the editors will not be responsible for loss or damage to photographs and illustrations sustained during mailing.

Online submissions

Manuscripts should be submitted through the Online Submission System at: <http://www.wjgnet.com/1949-8470/office>. Authors are highly recommended to consult the ONLINE INSTRUCTIONS TO AUTHORS (http://www.wjgnet.com/1949-8470/g_info_20100316162358.htm) before attempting to submit online. For assistance, authors encountering problems with the Online Submission System may send an email describing the problem to wjr@wjgnet.com, or by telephone: +86-10-85381892. If you submit your manuscript online, do not make a postal contribution. Repeated online submission for the same manuscript is strictly prohibited.

MANUSCRIPT PREPARATION

All contributions should be written in English. All articles must be submitted using word-processing software. All submissions must be typed in 1.5 line spacing and 12 pt. Book Antiqua with ample margins. Style should conform to our house format. Required information for each of the manuscript sections is as follows:

Title page

Title: Title should be less than 12 words.

Running title: A short running title of less than 6 words should be provided.

Authorship: Authorship credit should be in accordance with the standard proposed by International Committee of Medical Journal Editors, based on (1) substantial contributions to conception and design, acquisition of data, or analysis and interpretation of data; (2) drafting the article or revising it critically for important intellectual content; and (3) final approval of the version to be published. Authors should meet conditions 1, 2, and 3.

Institution: Author names should be given first, then the complete name of institution, city, province and postcode. For example, Xu-Chen Zhang, Li-Xin Mei, Department of Pathology, Chengde Medical College, Chengde 067000, Hebei Province, China. One author may be represented from two institutions, for example, George Sgourakis, Department of General, Visceral, and Transplantation Surgery, Essen 45122, Germany; George Sgourakis, 2nd Surgical

Department, Korgialenio-Benakio Red Cross Hospital, Athens 15451, Greece

Author contributions: The format of this section should be: Author contributions: Wang CL and Liang L contributed equally to this work; Wang CL, Liang L, Fu JF, Zou CC, Hong F and Wu XM designed the research; Wang CL, Zou CC, Hong F and Wu XM performed the research; Xue JZ and Lu JR contributed new reagents/analytic tools; Wang CL, Liang L and Fu JF analyzed the data; and Wang CL, Liang L and Fu JF wrote the paper.

Supportive foundations: The complete name and number of supportive foundations should be provided, e.g., Supported by National Natural Science Foundation of China, No. 30224801

Correspondence to: Only one corresponding address should be provided. Author names should be given first, then author title, affiliation, the complete name of institution, city, postcode, province, country, and email. All the letters in the email should be in lower case. A space interval should be inserted between country name and email address. For example, Montgomery Bissell, MD, Professor of Medicine, Chief, Liver Center, Gastroenterology Division, University of California, Box 0538, San Francisco, CA 94143, United States. montgomery.bissell@ucsf.edu

Telephone and fax: Telephone and fax should consist of +, country number, district number and telephone or fax number, e.g., Telephone: +86-10-85381892 Fax: +86-10-85381893

Peer reviewers: All articles received are subject to peer review. Normally, three experts are invited for each article. Decision for acceptance is made only when at least two experts recommend an article for publication. Reviewers for accepted manuscripts are acknowledged in each manuscript, and reviewers of articles which were not accepted will be acknowledged at the end of each issue. To ensure the quality of the articles published in *WJR*, reviewers of accepted manuscripts will be announced by publishing the name, title/position and institution of the reviewer in the footnote accompanying the printed article. For example, reviewers: Professor Jing-Yuan Fang, Shanghai Institute of Digestive Disease, Shanghai, Affiliated Renji Hospital, Medical Faculty, Shanghai Jiaotong University, Shanghai, China; Professor Xin-Wei Han, Department of Radiology, The First Affiliated Hospital, Zhengzhou University, Zhengzhou, Henan Province, China; and Professor Anren Kuang, Department of Nuclear Medicine, Huaxi Hospital, Sichuan University, Chengdu, Sichuan Province, China.

Abstract

There are unstructured abstracts (no more than 256 words) and structured abstracts (no more than 480). The specific requirements for structured abstracts are as follows:

An informative, structured abstracts of no more than 480 words should accompany each manuscript. Abstracts for original contributions should be structured into the following sections. AIM (no more than 20 words): Only the purpose should be included. Please write the aim as the form of "To investigate/study/...; MATERIALS AND METHODS (no more than 140 words); RESULTS (no more than 294 words): You should present *P* values where appropriate and must provide relevant data to illustrate how they were obtained, e.g. 6.92 ± 3.86 vs 3.61 ± 1.67 , $P < 0.001$; CONCLUSION (no more than 26 words).

Key words

Please list 5-10 key words, selected mainly from *Index Medicus*, which reflect the content of the study.

Text

For articles of these sections, original articles and brief articles, the main text should be structured into the following sections: INTRO-

DUCTION, MATERIALS AND METHODS, RESULTS and DISCUSSION, and should include appropriate Figures and Tables. Data should be presented in the main text or in Figures and Tables, but not in both. The main text format of these sections, editorial, topic highlight, case report, letters to the editors, can be found at: http://www.wjgnet.com/1949-8470/g_info_20100313183720.htm.

Illustrations

Figures should be numbered as 1, 2, 3, *etc.*, and mentioned clearly in the main text. Provide a brief title for each figure on a separate page. Detailed legends should not be provided under the figures. This part should be added into the text where the figures are applicable. Figures should be either Photoshop or Illustrator files (in tiff, eps, jpeg formats) at high-resolution. Examples can be found at: <http://www.wjgnet.com/1007-9327/13/4520.pdf>; <http://www.wjgnet.com/1007-9327/13/4554.pdf>; <http://www.wjgnet.com/1007-9327/13/4891.pdf>; <http://www.wjgnet.com/1007-9327/13/4986.pdf>; <http://www.wjgnet.com/1007-9327/13/4498.pdf>. Keeping all elements compiled is necessary in line-art image. Scale bars should be used rather than magnification factors, with the length of the bar defined in the legend rather than on the bar itself. File names should identify the figure and panel. Avoid layering type directly over shaded or textured areas. Please use uniform legends for the same subjects. For example: Figure 1 Pathological changes in atrophic gastritis after treatment. A: ...; B: ...; C: ...; D: ...; E: ...; F: ...; G: ...*etc.* It is our principle to publish high resolution-figures for the printed and E-versions.

Tables

Three-line tables should be numbered 1, 2, 3, *etc.*, and mentioned clearly in the main text. Provide a brief title for each table. Detailed legends should not be included under tables, but rather added into the text where applicable. The information should complement, but not duplicate the text. Use one horizontal line under the title, a second under column heads, and a third below the Table, above any footnotes. Vertical and italic lines should be omitted.

Notes in tables and illustrations

Data that are not statistically significant should not be noted. ^a*P* < 0.05, ^b*P* < 0.01 should be noted (*P* > 0.05 should not be noted). If there are other series of *P* values, ^c*P* < 0.05 and ^d*P* < 0.01 are used. A third series of *P* values can be expressed as ^e*P* < 0.05 and ^f*P* < 0.01. Other notes in tables or under illustrations should be expressed as ¹F, ²F, ³F; or sometimes as other symbols with a superscript (Arabic numerals) in the upper left corner. In a multi-curve illustration, each curve should be labeled with ●, ○, ■, □, ▲, △, *etc.*, in a certain sequence.

Acknowledgments

Brief acknowledgments of persons who have made genuine contributions to the manuscript and who endorse the data and conclusions should be included. Authors are responsible for obtaining written permission to use any copyrighted text and/or illustrations.

REFERENCES

Coding system

The author should number the references in Arabic numerals according to the citation order in the text. Put reference numbers in square brackets in superscript at the end of citation content or after the cited author's name. For citation content which is part of the narration, the coding number and square brackets should be typeset normally. For example, "Crohn's disease (CD) is associated with increased intestinal permeability^[12]". If references are cited directly in the text, they should be put together within the text, for example, "From references^[19,22-24], we know that..."

When the authors write the references, please ensure that the order in text is the same as in the references section, and also ensure the spelling accuracy of the first author's name. Do not list the same citation twice.

Instructions to authors

PMID and DOI

Pleased provide PubMed citation numbers to the reference list, e.g. PMID and DOI, which can be found at <http://www.ncbi.nlm.nih.gov/sites/entrez?db=pubmed> and <http://www.crossref.org/SimpleTextQuery/>, respectively. The numbers will be used in E-version of this journal.

Style for journal references

Authors: the name of the first author should be typed in bold-faced letters. The family name of all authors should be typed with the initial letter capitalized, followed by their abbreviated first and middle initials. (For example, Lian-Sheng Ma is abbreviated as Ma LS, Bo-Rong Pan as Pan BR). The title of the cited article and italicized journal title (journal title should be in its abbreviated form as shown in PubMed), publication date, volume number (in black), start page, and end page [PMID: 11819634 DOI: 10.3748/wjg.13.5396].

Style for book references

Authors: the name of the first author should be typed in bold-faced letters. The surname of all authors should be typed with the initial letter capitalized, followed by their abbreviated middle and first initials. (For example, Lian-Sheng Ma is abbreviated as Ma LS, Bo-Rong Pan as Pan BR) Book title. Publication number. Publication place: Publication press, Year: start page and end page.

Format

Journals

English journal article (list all authors and include the PMID where applicable)

- 1 **Jung EM**, Clevert DA, Schreyer AG, Schmitt S, Rennert J, Kubale R, Feuerbach S, Jung F. Evaluation of quantitative contrast harmonic imaging to assess malignancy of liver tumors: A prospective controlled two-center study. *World J Gastroenterol* 2007; **13**: 6356-6364 [PMID: 18081224 DOI: 10.3748/wjg.13.6356]

Chinese journal article (list all authors and include the PMID where applicable)

- 2 **Lin GZ**, Wang XZ, Wang P, Lin J, Yang FD. Immunologic effect of Jianpi Yishen decoction in treatment of Pixu-diarhoea. *Shijie Huaren Xiaohua Zazhi* 1999; **7**: 285-287

In press

- 3 **Tian D**, Araki H, Stahl E, Bergelson J, Kreitman M. Signature of balancing selection in Arabidopsis. *Proc Natl Acad Sci USA* 2006; In press

Organization as author

- 4 **Diabetes Prevention Program Research Group**. Hypertension, insulin, and proinsulin in participants with impaired glucose tolerance. *Hypertension* 2002; **40**: 679-686 [PMID: 12411462 PMID:2516377 DOI:10.1161/01.HYP.0000035706.28494.09]

Both personal authors and an organization as author

- 5 **Vallancien G**, Emberton M, Harving N, van Moorselaar RJ; Alf-One Study Group. Sexual dysfunction in 1, 274 European men suffering from lower urinary tract symptoms. *J Urol* 2003; **169**: 2257-2261 [PMID: 12771764 DOI:10.1097/01.ju.0000067940.76090.73]

No author given

- 6 21st century heart solution may have a sting in the tail. *BMJ* 2002; **325**: 184 [PMID: 12142303 DOI:10.1136/bmj.325.7357.184]

Volume with supplement

- 7 **Geraud G**, Spierings EL, Keywood C. Tolerability and safety of frovatriptan with short- and long-term use for treatment of migraine and in comparison with sumatriptan. *Headache* 2002; **42** Suppl 2: S93-99 [PMID: 12028325 DOI:10.1046/j.1526-4610.42.s2.7.x]

Issue with no volume

- 8 **Banit DM**, Kaufer H, Hartford JM. Intraoperative frozen section analysis in revision total joint arthroplasty. *Clin Orthop Relat Res* 2002; **(401)**: 230-238 [PMID: 12151900 DOI:10.1097/00003086-200208000-00026]

No volume or issue

- 9 Outreach: Bringing HIV-positive individuals into care. *HRS-A Careaction* 2002; 1-6 [PMID: 12154804]

Books

Personal author(s)

- 10 **Sherlock S**, Dooley J. Diseases of the liver and biliary system. 9th ed. Oxford: Blackwell Sci Pub, 1993: 258-296

Chapter in a book (list all authors)

- 11 **Lam SK**. Academic investigator's perspectives of medical treatment for peptic ulcer. In: Swabb EA, Azabo S. Ulcer disease: investigation and basis for therapy. New York: Marcel Dekker, 1991: 431-450

Author(s) and editor(s)

- 12 **Breedlove GK**, Schorffheide AM. Adolescent pregnancy. 2nd ed. Wicczorek RR, editor. White Plains (NY): March of Dimes Education Services, 2001: 20-34

Conference proceedings

- 13 **Harnden P**, Joffe JK, Jones WG, editors. Germ cell tumours V. Proceedings of the 5th Germ cell tumours Conference; 2001 Sep 13-15; Leeds, UK. New York: Springer, 2002: 30-56

Conference paper

- 14 **Christensen S**, Oppacher F. An analysis of Koza's computational effort statistic for genetic programming. In: Foster JA, Lutton E, Miller J, Ryan C, Tettamanzi AG, editors. Genetic programming. EuroGP 2002: Proceedings of the 5th European Conference on Genetic Programming; 2002 Apr 3-5; Kinsdale, Ireland. Berlin: Springer, 2002: 182-191

Electronic journal (list all authors)

- 15 Morse SS. Factors in the emergence of infectious diseases. *Emerg Infect Dis* serial online, 1995-01-03, cited 1996-06-05; 1(1): 24 screens. Available from: URL: <http://www.cdc.gov/ncidod/eid/index.htm>

Patent (list all authors)

- 16 **Pagedas AC**, inventor; Ancel Surgical R&D Inc., assignee. Flexible endoscopic grasping and cutting device and positioning tool assembly. United States patent US 20020103498. 2002 Aug 1

Statistical data

Write as mean \pm SD or mean \pm SE.

Statistical expression

Express *t* test as *t* (in italics), *F* test as *F* (in italics), chi square test as χ^2 (in Greek), related coefficient as *r* (in italics), degree of freedom as *v* (in Greek), sample number as *n* (in italics), and probability as *P* (in italics).

Units

Use SI units. For example: body mass, *m* (B) = 78 kg; blood pressure, *p* (B) = 16.2/12.3 kPa; incubation time, *t* (incubation) = 96 h; blood glucose concentration, *c* (glucose) 6.4 \pm 2.1 mmol/L; blood CEA mass concentration, *p* (CEA) = 8.6 24.5 μ g/L; CO₂ volume fraction, 50 mL/L CO₂, not 5% CO₂; likewise for 40 g/L formaldehyde, not 10% formalin; and mass fraction, 8 ng/g, etc. Arabic numerals such as 23, 243, 641 should be read 23 243 641.

The format for how to accurately write common units and quantums can be found at: http://www.wjgnet.com/1949-8470/g_info_20100313185816.htm.

Abbreviations

Standard abbreviations should be defined in the abstract and on first mention in the text. In general, terms should not be abbreviated unless they are used repeatedly and the abbreviation is helpful to the reader. Permissible abbreviations are listed in Units, Symbols and Abbreviations: A Guide for Biological and Medical Editors and Authors (Ed. Baron DN, 1988) published by The Royal Society of Medicine, London. Certain commonly used abbreviations, such as DNA, RNA, HIV, LD50, PCR, HBV, ECG, WBC, RBC, CT, ESR, CSF, IgG, ELISA, PBS, ATP, EDTA, mAb, can be used directly without further explanation.

Italics

Quantities: *t* time or temperature, *c* concentration, *A* area, *l* length, *m* mass, *V* volume.

Genotypes: *gyrA*, *arg 1*, *c myc*, *c fos*, etc.

Restriction enzymes: *EcoRI*, *HindI*, *BamHI*, *Kho I*, *Kpn I*, etc.

Biology: *H. pylori*, *E. coli*, etc.

Examples for paper writing

Editorial: http://www.wjgnet.com/1949-8470/g_info_20100313182341.htm

Frontier: http://www.wjgnet.com/1949-8470/g_info_20100313182448.htm

Topic highlight: http://www.wjgnet.com/1949-8470/g_info_20100313182639.htm

Observation: http://www.wjgnet.com/1949-8470/g_info_20100313182834.htm

Guidelines for basic research: http://www.wjgnet.com/1949-8470/g_info_20100313183057.htm

Guidelines for clinical practice: http://www.wjgnet.com/1949-8470/g_info_20100313183238.htm

Review: http://www.wjgnet.com/1949-8470/g_info_20100313183433.htm

Original articles: http://www.wjgnet.com/1949-8470/g_info_20100313183720.htm

Brief articles: http://www.wjgnet.com/1949-8470/g_info_20100313184005.htm

Case report: http://www.wjgnet.com/1949-8470/g_info_20100313184149.htm

Letters to the editor: http://www.wjgnet.com/1949-8470/g_info_20100313184410.htm

Book reviews: http://www.wjgnet.com/1949-8470/g_info_20100313184803.htm

Guidelines: http://www.wjgnet.com/1949-8470/g_info_20100313185047.htm

SUBMISSION OF THE REVISED MANUSCRIPTS AFTER ACCEPTED

Please revise your article according to the revision policies of *WJR*. The revised version including manuscript and high-resolution image figures (if any) should be re-submitted or uploaded online. The author should send copyright transfer letter, and responses to the reviewers and science news to us *via* email.

Editorial Office

World Journal of Radiology

Editorial Department: Room 903, Building D,
Ocean International Center,
No. 62 Dongsihuan Zhonglu,
Chaoyang District, Beijing 100025, China
E-mail: wjr@wjgnet.com
<http://www.wjgnet.com>
Telephone: +86-10-85381892
Fax: +86-10-85381893

Language evaluation

The language of a manuscript will be graded before it is sent for revision. (1) Grade A: priority publishing; (2) Grade B: minor language polishing; (3) Grade C: a great deal of language polishing needed; and (4) Grade D: rejected. Revised articles should reach Grade A or B.

Copyright assignment form

Please download a Copyright assignment form from http://www.wjgnet.com/1949-8470/g_info_20100313185522.htm.

Responses to reviewers

Please revise your article according to the comments/suggestions provided by the reviewers. The format for responses to the reviewers' comments can be found at: http://www.wjgnet.com/1949-8470/g_info_20100313185358.htm.

Proof of financial support

For paper supported by a foundation, authors should provide a copy of the document and serial number of the foundation.

Links to documents related to the manuscript

WJR will be initiating a platform to promote dynamic interactions between the editors, peer reviewers, readers and authors. After a manuscript is published online, links to the PDF version of the submitted manuscript, the peer-reviewers' report and the revised manuscript will be put on-line. Readers can make comments on the peer reviewer's report, authors' responses to peer reviewers, and the revised manuscript. We hope that authors will benefit from this feedback and be able to revise the manuscript accordingly in a timely manner.

Science news releases

Authors of accepted manuscripts are suggested to write a science news item to promote their articles. The news will be released rapidly at EurekAlert/AAAS (<http://www.eurekalert.org>). The title for news items should be less than 90 characters; the summary should be less than 75 words; and main body less than 500 words. Science news items should be lawful, ethical, and strictly based on your original content with an attractive title and interesting pictures.

Publication fee

Authors of accepted articles must pay a publication fee. EDITORIAL, TOPIC HIGHLIGHTS, BOOK REVIEWS and LETTERS TO THE EDITOR are published free of charge.